

Doctoral thesis

Doctoral theses at NTNU, 2021:232

Gagan Paudel

# Exploring glow discharge mass spectrometry applications in materials characterization

**NTNU**  
Norwegian University of Science and Technology  
Thesis for the Degree of  
Philosophiae Doctor  
Faculty of Natural Sciences  
Department of Materials Science and Engineering



Norwegian University of  
Science and Technology



Gagan Paudel

# **Exploring glow discharge mass spectrometry applications in materials characterization**

Thesis for the Degree of Philosophiae Doctor

Trondheim, June 2021

Norwegian University of Science and Technology  
Faculty of Natural Sciences  
Department of Materials Science and Engineering

**NTNU**

Norwegian University of Science and Technology

Thesis for the Degree of Philosophiae Doctor

Faculty of Natural Sciences

Department of Materials Science and Engineering

© Gagan Paudel

ISBN 978-82-326-6760-4 (printed ver.)

ISBN 978-82-326-6524-2 (electronic ver.)

ISSN 1503-8181 (printed ver.)

ISSN 2703-8084 (online ver.)

Doctoral theses at NTNU, 2021:232

Printed by NTNU Grafisk senter



Dedicated to

'that' which grows and evolves  
'that' ever changing, yet ever present

.....



## Preface

The thesis is submitted to Norwegian University of Science and Technology (NTNU) as a partial fulfilment for the requirements of the degree, Degree of Philosophiae Doctor. The main part of the work was performed during period August 2017 to February 2021 at Department of Materials Science and Engineering, NTNU. During August 2018-July 2019, the candidate also supported researchers at the department by preparing samples for inductively coupled plasma mass spectrometry (ICP-MS) characterization. The PhD project was funded by Department of Materials science and Engineering, where Professor Marisa Di Sabatino and Professor Hans Jørgen Roven were the candidate's main supervisor and co-supervisor, respectively.

The PhD education involved training of the candidate during period 24 – 26 October 2018 at Evans Analytical Group (EAG) Laboratories, Syracuse, USA. The sample preparation and characterization of non-conductive and powder samples were covered during the training.

The thesis consists of two sections and is presented in the form of papers collection. The first part of the thesis consists of the theory, literature review, applications of the direct-current glow discharge mass spectrometry, introduction to Astrum GDMS, and summary of papers. The second part of the thesis consists of published articles and the manuscript under a peer-review process.

In addition, during the PhD work, the candidate was involved in two projects where manuscripts are in preparation and therefore not presented in this dissertation. The work involved determination of relative sensitivity factor for aluminum certified reference materials and utilization of silicon masks for analysis of non-conductive samples such as alumina and sapphire.

Trondheim, April 2021

Gagan Paudel



## Scientific contributions related to the PhD work

### Scientific papers:

#### Paper I:

**Paudel, G.**, Kasik, M., and Di Sabatino, M. (2019) Investigation of the intensity dependence of glow discharge mass spectrometry quantification on the discharge parameters, *Journal of Analytical Atomic Spectrometry* 34, 1829-1837.

#### Paper II:

**Paudel, G.**, and Di Sabatino, M. (2020) Quantification of discharge gas to optimize discharge parameters for relative sensitivity factors (RSFs) determination by slow-flow glow discharge mass spectrometry (GDMS), *Journal of Analytical Atomic Spectrometry* 35, 2748-2757.

#### Paper III:

**Paudel, G.**, Khromov, S., Kasik, M., Roven, H. J., and Di Sabatino, M. (2020) Influence of polycrystalline material on crater shape optimization and roughness using low-power/low-pressure direct-current glow discharge mass spectrometry, *Journal of Analytical Atomic Spectrometry* 35, 1450-1457.

#### Paper IV:

**Paudel, G.**, Langelandsvik, G., Khromov, S., Arbo S.M., Westermann, I., Roven, H.J., and Di Sabatino, M. Depth profiling at a steel-aluminum interface using slow-flow direct current glow discharge mass spectrometry, *in a peer review process of Journal of Analytical and Bioanalytical Chemistry*.

### Contribution not included in the thesis:

1. **Paudel, G.**, and Di Sabatino, M. Relative sensitivity factors determination for aluminum analysis using slow-flow direct current glow discharge mass spectrometry, *manuscript in preparation*.
2. Busam, J., **Paudel, G.**, and Di Sabatino, M. Silicon and Indium as secondary cathode for the analysis of solid alumina and sapphire by slow-flow direct-current glow discharge mass spectrometry, *manuscript in preparation*.

## Conferences:

The conferences attended during the PhD project are given below with presenter underlined.

1. Impact of discharge parameters on elemental quantification of a slow-flow glow discharge Mass Spectrometer  
Gagan Paudel, Marisa Di Sabatino  
4<sup>th</sup> International Glow discharge Spectroscopy Symposium, Berlin, Germany  
16 –18 April 2018
2. Impact of Discharge Parameter on Elemental Quantification (Invited Talk)  
Gagan Paudel, Marisa Di Sabatino  
SCIX 2018, Atlanta, USA, 21–26 October 2018
3. Application of glow discharge mass spectrometry for characterization of solar cell  
Gagan Paudel, Marisa Di Sabatino  
Norwegian Solar Cell Conference 2019, Son, Norway, 20–21 May 2019
4. Exploring material characterization possibilities using Astrum glow discharge mass spectrometer  
Gagan Paudel, Hans Jørgen Roven, Marisa Di Sabatino  
National Conference for Material Technology 2020, Trondheim, Norway, 2–3 December 2020

## Other contributions:

During the PhD work, the candidate was involved in planning the experimental work for characterization of solar cell silicon ingots for master student, Ada Louise Heyerdahl Jervell. As a result, the project was completed which is titled as “Resistivity studies of High Performance multicrystalline compensated silicon ingots for solar cells”, NTNU 2018.

## Acknowledgements

I am grateful to the Department of Materials Science and Engineering at NTNU and especially to the admission committee involved in selection of PhD candidate for the project. At the hindsight, I am equally surprised as much as I am thankful for being selected as I had no experience of inorganic materials research until involved in the project. Coming from a different field meant that background knowledge was required at the initial stage of the PhD studies. Furthermore, to establish analytical workflow for a new instrument, with only few published articles available, was challenging. To overcome this, it has been an enjoyable and fulfilling journey where roads were crossed with a lot of people who impacted the project in one way or another. Some of the important ones are mentioned here.

My supervisors Professor Marisa Di Sabatino and Professor Hans Jørgen Roven deserve a great thanks for all assistance during my PhD. Their doors were always open for fruitful discussions and guidance. Professor Di Sabatino is also thanked for proofreading the thesis and for providing valuable feedbacks to all the manuscripts and whenever needed during the PhD. Not to mention the freedom and independency allowed during the PhD work. Special thanks to Professor Hans Jørgen Roven for discussions of third and fourth manuscript, his positivity and motivation.

I am grateful to have met and collaborated with Dr. Martin Kasik from MK2 Technologies Inc., USA, who is co-author of some of the papers. Dr. Kasik not only enriched me scientifically but deeply influenced me as a person.

Associate Professor Ida Westermann at NTNU and Dr. Siri Marthe Arbo from SINTEF Manufacturing AS are thanked for providing sample specimen for the fourth paper and discussions leading to work completion.

I am grateful to senior engineers at NTNU, Dr. Sergey Khromov and Syverin Lierhagen for all great support throughout PhD project and especially with SEM and ICP-MS analysis, respectively. Nu Instruments and scientists James Wright, Dr. Benoit Disch and Dr. Christopher Page are greatly acknowledged for sending in valuable samples and instrument parts, valuable discussions and, more importantly, for being available when I ran into problems with the instrument.

Dr. Karol Putyera and engineers from Evans Analytical Group (EAG) Laboratories are thanked for the training and characterization of samples.

Dear friend and colleague PhD fellow, Geir Langelandsvik is thanked for social and scientific discussions and for providing valuable insights to the life in Norway. Ada Louise Heyerdahl Jervell is thanked for excellent work on her thesis.

I thank my earlier office mates Mahmood Khan (exchange PhD fellow at NTNU) and Jochen Busam and later Dr. Maria Tsoutsouva for their guidance. The colleagues at the department, Dr. Omar Awayssa, Dr. Fabian Imanasa Azof, Simen N. H. Eliassen, Dr. Aina Opsal Bakke, JiaWei Yang, Dr. Mengyi Zhu, Arman Hoseinpour Kermani and Rania Hendawi are thanked for social discussions.

The delegates of the conferences are thanked, especially the European glow discharge conference held in Berlin in 2018 for their interest in my work, discussions and for sending in valuable samples. Anonymous reviewers of the manuscripts are thanked for challenging questions that helped to increase the quality of the work.

The PhD would certainly have been incomplete without the motivation and support of my beloved spouse Mrs. Bharati Mainali. Thank you for standing beside me during my highs and lows. समानान्तर रूपमा, म मेरा प्यारा बाबुआमाको त्याग, जीवन मूल्य र शिक्षाको लागि आभारी छु। My siblings and Mainali family are thanked for love, friendship, and support.

I am also thankful to all friends and families in Nepal and abroad including Norway. Same is reiterated for *NEST pariwar* in Trondheim who paved paths for building in valuable relationships which will stay for a long term. You all played your part in making me feel home in Norway. Thank you all!



## Abstract

Glow discharge mass spectrometry (GDMS) relying on continuous direct current discharge source coupled to sector field mass analyzer (SF-GDMS) is popular for its ability to detect impurities in sub-ppb level. Astrum GDMS is one of the recent instruments introduced of this category. Despite of its introduction in 2010, there are only a few articles available presenting Astrum's application and theory. Moreover, no systematic approach for determining the mode of Astrum operation, figures of merit, relative sensitivity factors (RSFs), or depth profiling are available. Therefore, the PhD thesis is focused on these limitations. Hence, broadly two applications are investigated, i.e., bulk analysis and depth profiling. To achieve this, different materials were studied, such as tantalum, silicon powder, and steel-aluminum bi-layered material.

Understanding the effect of glow discharge parameters is important as they affect quantification and, in turn, accuracy and reproducibility. Further, measurement of relative sensitivity factors (RSFs) is important to determine accurate results. Hence, firstly influence of glow discharge parameters on variation of elemental concentration was studied using a homogenous tantalum pin (>99.5% Ta) sample using a range of current and voltage settings (0.5 – 5 mA at 1 kV and 0.6 – 1.5 kV at 3 mA). The variation in concentration change was related to unequal change of absolute intensity of elemental impurities as compared to that of tantalum. Hence, RSFs vary with glow discharge parameters. Interestingly, this work hinted that measurement of discharge gas and other gaseous elements can contribute to optimization of discharge parameters before determining RSFs.

This followed analysis of silicon powder after pressing against high purity indium sheets. Various impurity elements were analysed using glow discharge current and voltage settings of 1 – 3.5 mA and 1 – 1.4 kV, respectively. Further, argon was quantified using current and voltage settings of 1– 5 mA and 1.2 – 1.6 kV, respectively. Remarkably the concentration of most of the impurity elements and quantification of

argon is found to vary less in range of 2 – 3 mA and 1.2 – 1.4 kV. This observation is consistent with argon and oxygen quantification using flat silicon and nitrogen quantification using aluminum flat samples. Further, gaseous elements such as carbon, oxygen, nitrogen and argon present in tantalum pin and nitrogen present in aluminum pin followed the same pattern. Hence, measurement of gaseous elements and discharge gas can contribute to RSFs determination in other matrices also. Finally, relative sensitivity factors of 16 impurity elements valuable for solar cell silicon application are determined using certified silicon standard.

For depth profiling application, the glow discharge settings leading to optimum crater shapes are determined using tantalum flat samples. The results of the study indicate that current to voltage ratio in range of 0.2 – 0.35 kV/mA results into flat craters in tantalum. Hence, five different combinations of current and voltage are found given as, (i) 2 mA, 0.6 kV; (ii) 2.3 mA, 0.7 kV; (iii) 3 mA, 0.8 kV; (iv) 4 mA, 0.9 kV and (v) 5 mA, 1 kV. Further, sputtering rate increases with increasing current and voltage setting. Sputtering of tantalum of small and large grains indicated that differential sputtering of grains of different crystal orientation generated crater bottom roughness.

This followed analysis of steel-aluminum bi-layered material where firstly crater shape optimization using base aluminum material was carried out using similar approach as with tantalum flat sample. The depth profiling of chromium and nickel is carried out in non-heated and heat treated (at 400 °C for 30 min) steel-aluminum bi-layered joints. The analysis was performed using glow discharge current and voltage of 5 mA and 0.75 kV, respectively. Using Astrum GDMS, the diffusion behavior of trace alloying elements such as chromium and nickel at the aluminum-steel interface was investigated. The results of the work indicate enrichment of both impurity elements for both set of samples at the steel-aluminum interface. The heat-treated sample demonstrated higher content of chromium and nickel at the interface as well as formation of thin intermetallic layer. Further, chromium precipitates along with iron were found in the aluminum layer correlating with high chromium content in the aluminum layer.

## List of symbols and abbreviations

°C: degree Celsius	LA-ICP-OES: laser ablation inductively coupled plasma optical emission spectroscopy
µg: microgram	m/z: mass to charge ratio
µm: micrometre	M: atomic mass
A: ampere	m: mass
Å: Angstrom	M <sup>0</sup> : ground atom other than argon
AES: auger electron spectroscopy	M <sup>+</sup> : ground atom ion other than argon
A <sub>Mi</sub> , I <sub>Mi</sub> : abundance and intensity of matrix	M <sub>1</sub> and M <sub>2</sub> : mass of impinging ion and cathode material
Ar <sup>*</sup> : excited state argon	mA: milliampere
Ar <sup>+</sup> /Ar <sup>*</sup> : argon ion to metastable argon ratio	min: minute
Ar <sup>+</sup> : argon ion	ml/min: millimetre per minute
Ar <sup>0</sup> : ground state of argon atom	N: Avogadro number
Ar <sup>+</sup> : argon fast ion	nm: nanometre
Ar <sup>0</sup> : argon fast atom	ppb: parts per billion
Ar <sub>m</sub> <sup>*</sup> : excited state of argon	ppm: parts per million
Ar <sub>s</sub> : slow argon atom	PP-TOF-GDMS: plasma profiling time of flight glow discharge mass spectrometry
Ar <sub>s</sub> <sup>+</sup> : slow argon ion	Q: sputtering rate
A <sub>xi</sub> , I <sub>xi</sub> : abundance and intensity of analyte	r: radius of electrostatic and magnetic sector
B: magnetic field strength	RF: radio frequency
CHC: combined hollow cathode	RM: reference material
cm: centimetre	RSFs: relative sensitivity factors
cps: counts per second	RSF <sub>x/M</sub> : RSF of element/isotope x in matrix M
C <sub>Q</sub> : material dependent sputtering constant	s: second
CRM: certified reference material	S: sputtering yield
C <sub>x/M</sub> : concentration of analyte element/isotope	SF-GDMS: sector field glow discharge mass spectrometry
dc: direct current	SIMS: secondary ion mass spectrometry
e <sup>-</sup> : electron	SNMS: sputtering neutral mass spectrometry
E: electrostatic field strength	stdRSF <sub>x</sub> : standard relative sensitivity factors
EBSD: electron backscattered diffraction	U <sub>0</sub> : heat of sublimation
EPMA: electron probe micro-analyzer	v: velocity
ESA: electrostatic analyzer	V: volt
eV: electron volt	V <sub>0</sub> : threshold voltage
FC: centrifugal force	V <sub>b</sub> : breakdown voltage
FM: centripetal force	V <sub>c</sub> : cathode fall
GDMS: glow discharge mass spectrometry	V <sub>g</sub> : discharge voltage
GDOES: glow discharge optical emission Spectroscopy	V <sub>n</sub> : operating voltage
h: hour	W: watt
IBR <sub>x/M</sub> : abundance corrected ion beam ratio	X <sup>-</sup> : arbitrary anion
ICE: ion count efficiency	X <sup>+</sup> : arbitrary cation
ICP-MS: Inductively coupled plasma mass spectrometry	X <sup>0</sup> : neutral arbitrary atom
i <sub>g</sub> : discharge current	XPS: X-ray photoelectron spectroscopy
KE: kinetic energy	Y: number of secondary electrons
keV: kiloelectron volt	Y: third body
kV: kilovolt	z: charge
LA-ICP-MS: laser ablation inductively coupled plasma mass spectrometry	σ: collisional cross section area

# Table of contents

Preface.....	i
Scientific contributions related to the PhD work.....	iii
Acknowledgements.....	v
Abstract.....	vii
List of symbols and abbreviations.....	ix
<b>1. Introduction</b>	
1.1 Motivation and scope.....	1
1.2 Outline.....	2
<b>2. Fundamentals of glow discharge plasma</b>	
2.1 Electrical discharges and the glow discharge.....	4
2.2 Regions in the glow discharge plasma.....	7
2.2.1 The cathode dark space.....	8
2.2.2 The negative glow.....	8
2.2.3 The anode zone.....	8
2.3 Processes occurring in the glow discharge plasma.....	8
2.3.1 Ionization and excitation of argon.....	9
A. Electron impact ionization and excitation.....	9
B. Photoionization and excitation.....	10
C. Ionization and excitation of argon atoms due to fast argon species.....	10
D. Symmetric charge transfer.....	11
2.3.2 Ionization and excitation of sputtered atoms.....	11
A. Electron impact ionization and excitation.....	11
B. Penning ionization.....	12
C. Asymmetric charge transfer.....	12
D. Charge transfer and ionization: formation of doubly charged ions.....	12
2.3.3 Recombination in glow discharge plasma.....	13
A. Three body collision.....	13
B. Two stage recombination.....	13
C. Dissociation.....	14
2.3.4 Relaxation.....	14
2.4 Sputtering.....	15
2.4.1 Sputtering yield.....	15
2.4.2 Factors affecting sputtering.....	15
A. Discharge gas and mass of impinging ions.....	15
B. Angle of incidence of impinging ions.....	16
C. Energy of impinging ions.....	16
D. Cathode material.....	16
E. Temperature of cathode.....	17

2.4.3	Sputtering rate.....	17
<b>3.</b>	<b>Glow discharge mass spectrometry</b>	
3.1	Glow discharge operation modes.....	22
3.2	Glow discharge geometries.....	24
3.3	Mass analyzers.....	26
3.3.1	Magnetic sector and double focusing mass analyzers.....	26
3.4	Quantification approaches in GDMS.....	29
3.4.1	Ion beam ratio.....	29
3.4.2	Calibrated materials and relative sensitivity factors.....	29
3.4.3	Standard relative sensitivity factors.....	30
3.5	Applications.....	32
3.5.1	Bulk analysis.....	32
A.	Metals.....	32
B.	Bulk analysis for solar cell silicon applications.....	33
C.	Powders.....	33
D.	Non-conductive samples.....	33
3.5.2	Depth profiling.....	34
3.6	Glow discharge mass spectrometry compared to other techniques.....	36
<b>4.</b>	<b>Astrum GDMS</b>	
4.1	Introduction.....	40
4.2	Operation of glow discharge.....	41
4.3	Tuning of Astrum GDMS.....	42
4.4	Glow discharge cell and sample holder.....	44
<b>5.</b>	<b>Summary of papers</b>	
5.1	Paper I: Tantalum pin analysis.....	47
5.2	Paper II: Silicon powder analysis.....	49
5.3	Paper III: Tantalum flat sputtering and roughness.....	51
5.4	Paper IV: Steel-Aluminum joint depth profiling.....	52
5.5	Other interesting data.....	53
<b>6.</b>	<b>Conclusions and Recommendations</b>	
6.1	Conclusions.....	56
6.2	Limitations of the PhD work.....	57
6.3	Recommendations and outlook.....	58
<b>7.</b>	<b>References.....</b>	<b>60</b>
<b>8.</b>	<b>Paper collection</b>	
Paper I:	Tantalum pin analysis.....	69
Paper II:	Silicon powder analysis.....	81
Paper III:	Tantalum flat sputtering and roughness.....	96
Paper IV:	Steel-Aluminum joint depth profiling.....	107
<b>9.</b>	<b>Appendix</b>	
Appendix 1:	Ionization energy of various elements.....	122
Appendix 2:	Sputtering rate of tantalum.....	123



**CHAPTER 1**  
**Introduction**





# 1. Introduction

## 1.1 Motivation and scope

Glow discharge mass spectrometry (GDMS) is one of the popular techniques for analysis of materials for elemental characterization and determination of isotopic ratios. It is known for direct analysis of solid specimens which require minimal sample preparation. No need for ultra-high vacuum conditions in the ionization chamber, short analysis time as well as flexibility of using non-matrix matched standards for quantification makes it popular for industrial applications where high sample throughput is required. Further, depending upon the GDMS type, it offers good precision, reproducibility, robustness and offers high dynamic range of concentration. Therefore, GDMS is a well-established analytical technique for quality control applications. Among various glow discharge mass spectrometry systems, direct current glow discharge ion source coupled with sector field mass analyzer is among the most popular GDMS instruments. The low detection limit makes this type of instrument ideal for bulk application of high purity materials. Astrum GDMS is one of such instruments introduced in 2010 by Nu Instruments in UK. Currently, there are about 60 Astrum instruments installed worldwide. Although it is more than a decade since its introduction, not much information is available in the open literature regarding its applications. In addition, the Department of Materials Science and Engineering at NTNU received such an instrument at the end of 2016. Therefore, the motivation of this PhD work has been to explore the application possibilities of this new and powerful instrument. Following objectives are set for the PhD project:

1. Understanding the influence of glow discharge parameters in absolute intensity of matrix and impurity elements and how it impacts variation in elemental concentration.
2. Estimating possibility of using glow discharge gas and other gaseous elements for optimizing discharge condition for RSFs determination.
3. Designing analytical workflow for determining relative sensitivity factors (RSFs) using silicon powders.
4. Determining glow discharge parameters for obtaining optimum crater profiles and influence on sputtering rate.

5. Understanding the influence of differential sputtering on crater bottom roughness.
6. Application of depth profiling for understanding heat induced diffusion in iron-aluminum joints.

## **1.2 Outline**

The dissertation is presented as a collection of peer-reviewed articles preceded by several introductory chapters. Firstly, fundamentals of glow discharge plasma and sputtering is presented. In the chapter 3, "Glow discharge mass spectrometry", a literature review about GDMS instruments and its applications in material characterization is discussed. Likewise, a short chapter dedicated to Astrum GDMS is also presented. Additionally, the main findings of the PhD work are presented. Here, results of the published articles, the article in a peer-review process, and some unpublished work are summarized. Furthermore, the main conclusions from the PhD work are presented. Moreover, the limitations of the work are pointed out. For further improvement of applications of Astrum GDMS, lastly, outlook and recommendations are presented.

**CHAPTER 2**  
**Fundamentals of glow discharge plasma**

## 2.1 Electrical discharges and the glow discharge

In general, gas is a poor electrical conductor. However, if gas at a low pressure is placed between two electrodes and voltage is applied between them, then the resistivity of the gas decreases. With further increase of voltage at a certain point, the gas starts to break down, forming electron-ion pairs and hence generation of an electric field. This leads to the current flow through the gaseous medium as positively and negatively charged species are accelerated towards the cathode and the anode, respectively. This phenomenon is referred to as 'electrical discharge'. The potential at which electrical discharge occurs is known as the breakdown voltage ( $V_b$ ) (Figure 2-1). The breakdown voltage can be influenced by several factors for instance, the type of discharge gas used<sup>1-3</sup>, distance between electrodes and gas pressure<sup>4</sup>, physiochemical properties of cathode such as electrical conductivity, heat of sublimation<sup>5</sup>, and secondary electron emission.<sup>6-8</sup> The gas conductivity can also be increased by other means, e.g., by heating at very high temperatures or subjecting gas with other sources such as ultraviolet rays. The electron-ion pairs generated by this means generate very low currents (approx.  $10^{-12}$  A) and are not self-sustaining. The first region among various types of electrical discharges as a function of current-voltage behavior is the Townsend discharge (as shown in Figure 2-1), which typically does not extinguish.

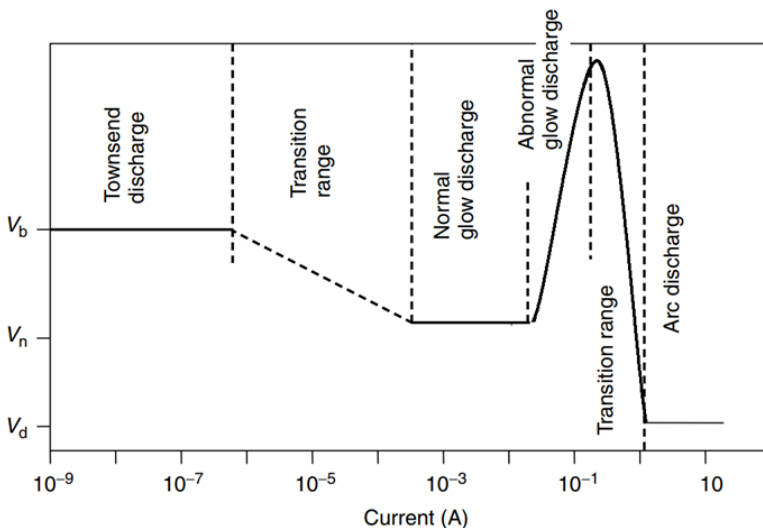


**Figure 2-1:** Current-voltage (i-V) characteristics of electrical discharges (*reprinted with permission from*<sup>9</sup>, Copyright © 2003 John Wiley & Sons, Ltd).

After the Townsend discharge, a transition range follows where the further increase of current does not require an increase in voltage. In fact, at the operating voltage,  $V_n$ , which is lower than that of breakdown voltage,  $V_b$ , it is still possible to sustain the electrical discharge. This is a characteristic of a self-sustained discharge which occurs due to continuous electron-ion production from initially produced electrons.

The transition range is followed by a normal glow discharge. The term glow discharge was coined after a luminous glow that forms between the electrodes, due to excitation/de-excitation process of atoms in the discharge. The color of luminous glow is observed to be dependent on the type of discharge gas used, for instance, argon discharge has a bluish violet color.<sup>10</sup> In normal glow discharge, the cathode surface is not entirely covered by the discharge. Increase in current is achieved as more of the cathode surface is proportionally covered by the glow discharge (as shown in Figure 2-2). Hence, the voltage remains constant. However, at some point when current is increased further, the cathode surface is fully covered and increase in current density leads to further increase in voltage. This electrical discharge is referred to as an abnormal glow discharge (Figure 2-1 and 2-2). The analytical glow discharge such as glow discharge mass spectrometry operates in this mode with reduced inert gas pressure of (0.1 – 10 Torr) at power less than 100 W.<sup>9, 11</sup> With careful selection of current and voltage in the flat sample setup, glow discharge can be regulated in such a way that the cathode surface is evenly covered to ensure uniform sputtering. This allows depth-profiling application using analytical glow discharge mass spectrometry.

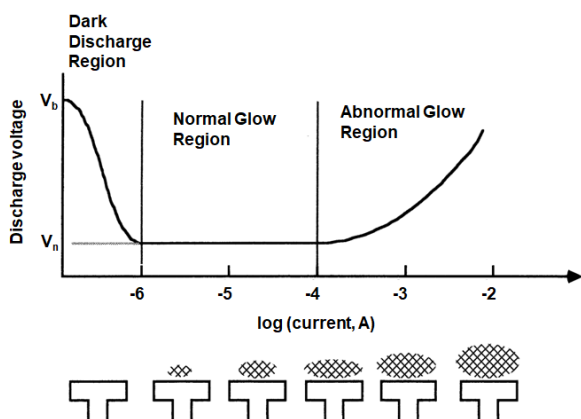


**Figure 2-2:** Transition between normal to abnormal glow discharge (reprinted from <sup>11</sup>, Copyright © 1993 Springer).

The further increase of current leads to maximum rise in potential followed by fall of potential to a low value. This mode is known as arc discharge where current density is very high leading to heating and vaporization of the cathode material. Thermionic electron emission becomes the prominent electron carrying mechanism at high current values in the range of 10 – 1000 A.<sup>9, 11</sup> At higher fields, especially for samples with a pointed tip, electrons tunnel out of the cathode surface.<sup>12-14</sup> This process, however, is of negligible significance to glow discharge spectrometry as ultrathin samples or substantially higher voltages are not used.

## 2.2 Regions in the glow discharge plasma

The glow discharge plasma is a weakly ionized gas which is electrically neutral and has a degree of ionization in the order of 0.01 %.<sup>15</sup> Hence, the plasma mostly consists of neutrals atoms. Other species that could be present in the plasma are molecular clusters, free radicals, photons, excited species, etc. Depending on the degree of excitation/de-excitation process, glow discharge plasma comprises of series of several dark or light (glowing) regions. The dark regions are dominated by processes other than excitation/de-excitation transitions, for example ionization collisions.<sup>15</sup>

As depicted in Figure 2-3, glow discharge plasma consists of as many as eight regions depending on the tube length and pressure. Modern mass spectrometers utilize the abnormal glow discharge, where inter-electrode distance is relatively small with only three prominent regions<sup>15, 16</sup>, i.e., the cathode dark space, the negative glow and the anode dark space.

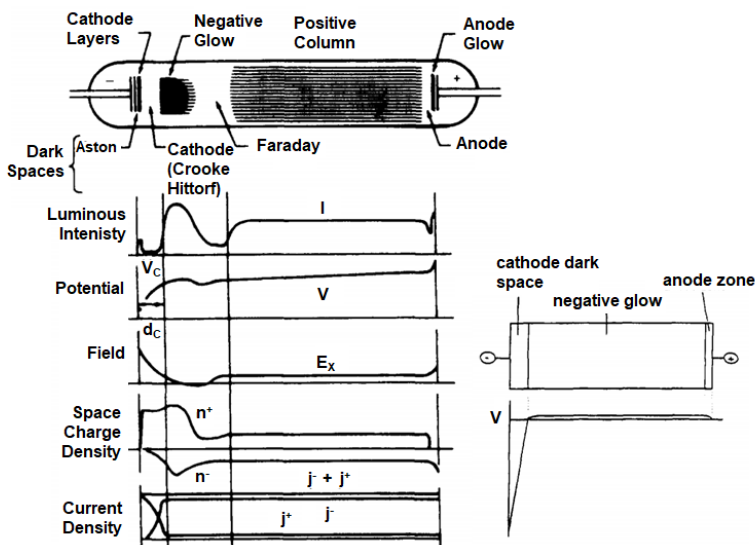


**Figure 2-3:** Different regions in glow discharge plasma and how distribution of luminous intensity, potential, electric field, space charge density, and current density varies (left), distribution of potential and prominent regions in analytical glow discharge plasma (right), *reprinted with permission from*<sup>15</sup> *Copyright © 1980, John Wiley and Sons (left) and (right)*<sup>16</sup> *Copyright © 1998 Published by Elsevier B.V respectively.*

### **2.2.1 The cathode dark space**

The cathode dark space is considered as the most important part of glow discharge as it is responsible for sustaining the glow discharge plasma. There is a characteristic voltage drop in this region referred to as the cathode fall ( $V_c$ ). The large potential difference over a small distance gives rise to a high electric field in front of the cathode. This field is responsible for acceleration of emitted electrons which eventually leads to ionization collisions in the plasma. The ions formed accelerate towards the cathode generating more secondary electrons leading to more ionization collisions. As an output, these processes contribute to the sustenance of the glow discharge plasma.

Due to the electric field, the number of positive ions will be higher closer to the cathode as compared to electrons. Moreover, the argon ions are the current carrier in the cathode dark space, while density of electrons increases further away from the cathode.

### **2.2.2 The negative glow**

The negative glow is a luminous region of the glow discharge plasma, which is more or less equipotential and field-free. The electrons lose their energy due to numerous collisions which contribute to excitation/de-excitation transitions emitting bright light. In this region, the positive and negative charge are nearly equal leading to charge neutrality.

### **2.2.3 The anode zone**

Due to the shorter interelectrode distance in analytical glow discharge, all remaining parts of the plasma are compressed to form the anode dark space. This region is similar to the cathode dark space where voltage falls only slightly as compared to the cathode dark space and therefore does not contribute as much to acceleration or deceleration of charged species.

## **2.3 Processes occurring in the glow discharge plasma**

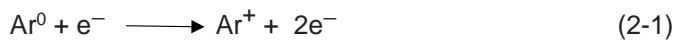
At this point, it is appropriate to introduce some of the relevant collisional processes occurring in the glow discharge plasma, which are important to understand some of



the findings of the PhD work. As argon has been used as discharge gas throughout the PhD work, the processes discussed here are specific to this. It is also common to use other inert gases such as helium,<sup>17</sup> neon,<sup>18</sup> or in combination with argon.<sup>19-21</sup> Furthermore, there are studies where non-inert gases such as hydrogen<sup>18, 22</sup>, oxygen<sup>23, 24</sup> or nitrogen<sup>25</sup> are added to inert gases. Such experiments have led to generation of new sets of emission lines from excited atoms<sup>19</sup>, enhancement in signal intensity of impurity ions<sup>20</sup>, change in sputtering rate of cathode<sup>24</sup> or change in ionization/excitation patterns.<sup>21, 26, 27</sup> Hence, these investigations open new possibilities of glow discharge applications.

### 2.3.1 Ionization and excitation of argon

#### A. Electron impact ionization and excitation



The fast electrons generated close to the cathode dark space of sufficient energy can knock off an electron from an argon atom ( $\text{Ar}^0$ ) generating the argon ion ( $\text{Ar}^+$ ). The minimum electron energy required for this reaction to occur is the first ionization potential of argon, i.e., 15.76 eV. This ionization process is referred to as direct electron impact ionization (equation 2-1). The process contributes to the sustenance of plasma as it leads to electron multiplication thereby generating more argon ions that lead to more sputtering.

The electron impact ionization can occur either in a single step, i.e., direct electron impact ionization or in two steps, i.e., two-step electron impact ionization.<sup>16</sup> The latter process at first involves the generation of metastable argon ( $\text{Ar}_m^*$ ) of 11.55 eV or 11.72 eV, i.e., excitation of argon atoms at higher energy level (as shown in equation 2-2). The two-step electron impact ionization requires additional electron energy of 4.21 eV for its ionization (equation 2-3).

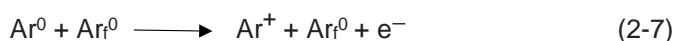
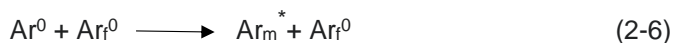
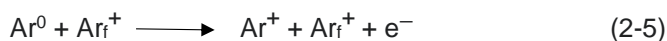
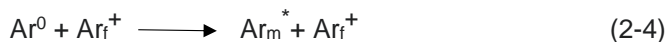
The collision of species in plasma depends on the mean free path, i.e., the average distance travelled by one species before colliding with other species. The mean free path decreases with higher pressure and depends on atom size and volume of the glow discharge cell.<sup>15</sup> A more versatile term collisional cross section is used to indicate the probability or uncertainty of collision, where collisional cross section area ( $\sigma$ ) is plotted against the function of electron velocity or energy. The higher energy means decrease in interaction time. The collision cross section area is dependent on the mass of colliding species, radius and polarizability.<sup>15</sup>

The cross sections for direct and two-step electron impact ionization have maximum values in the range of  $3 \times 10^{-16} \text{ cm}^2$  and  $8 \times 10^{-16} \text{ cm}^2$  at about 80 and 10 eV, respectively.<sup>16</sup> Beyond these values the residence time of electron around argon is reported to decrease, hence leading to decline in efficient ionization. Likewise, electron impact excitation reaches maximum of  $1.6 \times 10^{-16} \text{ cm}^2$  at about 20 eV for lower excitation level of 11.55 eV.<sup>16</sup>

## B. Photoionization and excitation

Similar to the electron impact ionization/excitation, other sufficient energy inputs like thermal or photon activation can also ionize or excite argon atoms. The glow discharge plasma is considered as a cold plasma, i.e., temperature of ions and neutrals is about 300 K. Therefore, the ionization and excitation due to heat transfer is negligible. The photoionization cross section for argon is reported to have a threshold value of about 15.8 eV, which corresponds to wavelength of about 800 Å.<sup>16</sup> The cross section is maximum at about  $3.7 \times 10^{-17} \text{ cm}^2$  and then decreases at higher energy.<sup>16</sup>

## C. Ionization and excitation of argon atoms due to fast argon species



As previously stated, the electric field near the cathode strongly repels electrons in front of cathode while strongly attracts fast argon ions towards the cathode. Such energetic argon ions ( $Ar_f^+$ ) are responsible for excitation (as shown in equation 2-4) and ionization of other argon atoms (as shown in equation 2-5). This is also true in case of neutral fast argon atoms,  $Ar_f^0$  (as shown in equation 2-6 and 2-7). For this process to come into existence, the voltage across the electrodes should be about 100 volts.<sup>16</sup> Furthermore, the importance of this process is believed to increase at voltage beyond 1000 volts where cross sectional values are maximum in the order of  $10^{-16} \text{ cm}^2$ .<sup>16</sup>

#### D. Symmetric charge transfer



The fast argon ions ( $Ar_f^+$ ) can also collide to slow argon atoms ( $Ar_s^0$ ) forming slow argon ions,  $Ar_s^+$  (as shown in equation 2-8). Such ions are responsible for the sputtering of the cathode. During this process the number of electrons or ions does not increase. The kinetic energy of colliding species does not change.

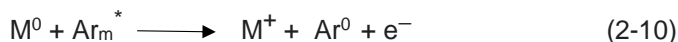
### 2.3.2 Ionization and excitation of sputtered atoms

#### A. Electron impact ionization and excitation



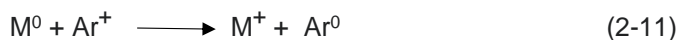
Similar to electron impact ionization of argon, sputtered atoms ( $M^0$ ) can also be ionized by the same process (as shown in equation 2-9). This requires bombardment of atoms with electrons with energy of at least first ionization potential of these atoms. The ionization cross section for all elements are reported to possess similar curves and hence considered to be a non-selective ionization process.<sup>16</sup>

## B. Penning ionization



Upon collision of sputtered atom with metastable argon, the energy transfer can lead to ionization of analyte atoms if the ionization potential of analyte atom is lower than the metastable energy of argon (equation 2-10). This process is considered to be dominant in low pressure discharge such as glow discharge mass spectrometry.<sup>16</sup> Except for a few elements in the periodic table most of the elements can be ionized by this process.<sup>16</sup>

## C. Asymmetric charge transfer



This is a very specific type of ionization process, which involves transfer of electron from the analyte atom to the argon ion (shown in equation 2-11). For this to happen, the energy difference between the argon ion ground state or metastable level and the energy level of resulting analyte ion should be sufficiently small, generally in the range of 0.02 – 1 eV above or below the argon levels respectively.<sup>28</sup> The efficiency of this process decreases at higher energy differences, although some work in the literature suggests this process to occur at higher energy differences close to 2 eV while is most effective in range of 0.1 – 0.4 eV.<sup>28</sup> Steers and coworkers have demonstrated occurrence of asymmetric charge transfer between Ar<sup>+</sup> and Cu<sup>29</sup>, Ar<sup>+</sup> and Fe<sup>30</sup>, and between Ar<sup>+</sup> and Ti.<sup>31</sup> Recent work by Mushtaq et al. has demonstrated that addition of gases, such as oxygen and hydrogen, is found to be involved in asymmetric charge transfer.<sup>23, 27</sup>

## D. Charge transfer and ionization: formation of doubly charged ions

Doubly charged ions occur in glow discharge plasma. However, population of double charge ions is more common for plasma gas with higher metastable energy, i.e., more common in neon plasma than in argon plasma.<sup>32</sup> Mushtaq et al. found that elements

with the double ionization energy lower than that of first ionization energy of discharge gas are more likely to occur in doubly charged states due to charge transfer and ionization.<sup>32</sup> Further, specifically for argon plasma, it is stated that it is only barium and radium doubly charged ions that can be produced by charge transfer and ionization.<sup>32</sup>

### 2.3.3 Recombination in glow discharge plasma

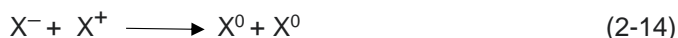
Ionization is the process by which ions are formed from neutral atoms, while recombination is the process by which positive ions reverses back to neutral atoms by coalescing with electrons. This process of recombination increases with increase in gas pressure.

#### A. Three body collision



Law of conservation of momentum and energy does not support the two-body collision.<sup>15, 16</sup> A third body is required to satisfy these laws where the wall of a glow discharge cell or any another particle in the plasma can be a third body. The third particle (Y) takes away the excess energy to satisfy the conservation laws. A general equation representing three-body collision is shown in equation 2-12a and 2-12b.<sup>33</sup> The rate constants of this process indicate that an electron is most efficient third body while a heavy particle such as gas atom slows down the process.<sup>16</sup>

#### B. Two stage recombination



Firstly, an electron is captured by a neutral atom forming a negative ion (as shown in equation 2-13). As a last step, positive and negative ion collide with each other such that the electron is transferred from the negative atom to positive atoms thereby

forming two neutrals (as shown in equation 2-14). However, the likelihood of this type of recombination is negligible. The limiting factor is lack of sufficiently high affinity of an atom to the electron (equation 2-13). As argon does not easily participate in such reaction, the probability of formation of negative ion is negligible.<sup>16</sup>

### **C. Dissociation**

A molecular ion can dissociate into products with certain kinetic and potential energy. This is a common process in glow discharge plasma as association of atoms lead to formation of molecular species. If such molecular species are close to the mass to charge ratio of analyte ion of interest, then it leads to challenges in identification of the analyte ion due to interference. Hence, dissociation in this case is helpful to reduce interference.

#### **2.3.4 Relaxation**

Relaxation is the inverse process to excitation. The excited states are unstable and return to ground state in one or several transitions where lifetime varies from nanoseconds to seconds. Each transition is associated with emission of a photon of certain energy which is generally in the visible range of 410 – 720 nm.<sup>16</sup>

## 2.4 Sputtering

Sputtering is an atomization process during which sample atoms are ejected out of the cathode surface by bombardment of discharge gas ions or atoms with energy greater than 30 eV.<sup>11</sup> The energy and momentum transfer by the impinging projectiles can spread in random directions among which some propagate back to the cathode surface and eventually lead to ejection of atoms. This may happen if the impact created by collision cascade is greater than the surface binding energy of an atom. It is understood that besides gas ions, gas atoms or matrix ions near the cathode dark space can also participate in the sputtering process. The atomization process is followed by subsequent excitation and/or ionization in plasma.

### 2.4.1 Sputtering yield

Sputtering yield denotes the sputtering efficiency and is defined as the number of atoms sputtered per incident projectile. For argon glow discharge, it is approximately 0.1, which means for each ten argon ions hitting the sample surface, one atom of cathode is ejected.<sup>11</sup> The sputtering yield is represented by equation 2-15.<sup>34</sup>

$$\frac{S}{1+\gamma} = \frac{0.0965*Q}{M} \quad (2-15)$$

Where  $S$  is sputtering yield,  $\gamma$  is number of secondary electrons released and  $Q$  is sputtering rate in  $\mu\text{gs}^{-1}$  and  $M$  is atomic mass of cathode. There are some factors that influence the sputtering yield, which are mentioned below.

### 2.4.2 Factors affecting sputtering

#### A. Discharge gas and mass of impinging ions

The fact that mostly noble gases are used as discharge gas leads to higher sputtering yields as they do not react with the cathode. Further, discharge gases are also available in high purity. The sputtering yield is higher for materials with atomic mass close to that of the impinging projectile.<sup>11</sup>

## **B. Angle of incidence of impinging ions**

The sputtering yield continuously increases with angle of incidence and has highest values at about 60°- 80° relative to the cathode surface beyond which it drops.<sup>11</sup> The rationale behind this is increase in probability of collision cascade to propagate towards cathode surface at angles below 90°. At higher angles, impinging ions are more likely to be reflected off the surface.

## **C. Energy of impinging ions**

There is no sputtering until a certain energy of impinging ions, which is referred to as the threshold energy. Beyond this, sputtering yield is linearly dependent to the energy of impinging ions. The threshold energy required for sputtering to take place varies from one material to another, as surface binding energy should be exceeded which is material specific. Some literature suggest that a good estimate of surface binding energy depends on heat of sublimation and secondary electron yield.<sup>5</sup> At very high energies such as several keV, the sputtering yield reaches a plateau which can be attributed to ion implantation.<sup>11</sup>

## **D. Cathode material**

Besides heat of sublimation, the electrical conductivity of a material is important for the sputtering to occur. For direct current glow discharge mass spectrometry, insulators are not sputtered without use of secondary cathode. For transition elements, the sputtering yield is found to be correlated with d-orbital filling, where elements with filled d-shell sputter higher as compared to less filled elements.<sup>11</sup> The d-shell filling is associated with decrease in atomic radii hence contributing to higher atomic density. The energy and momentum transfer to denser elements is expected to be slightly higher as compared to less dense atoms. Therefore, differential sputtering is likely for multi-elemental samples.<sup>11, 35</sup>



## E. Temperature of the cathode

The sample heating during glow discharge mass spectrometry operation can influence sputtering yield. The increase in sample temperature during the sputtering process can anneal the loosely bound atoms, thereby increasing the surface binding energy.<sup>11</sup> Likewise, volatile elements with lower heat of sublimation may evaporate out of the sample surface.<sup>36</sup> Such elements can have variable sputtering rates.<sup>37</sup> Furthermore, elements with low melting points, such as gallium, cannot be analysed without cryocooling due to heat generation during the sputtering process. Some GD instruments such as Astrum or VG9000 allow cryocooling possibility.<sup>38</sup> The introduction of a new microsecond pulse GD supply of Element GD allows measurement of gallium without use of cryocooling.<sup>39</sup> Lastly, elements with higher diffusion coefficient may enrich into the surface during sputtering due to elevated temperature.<sup>40</sup>

### 2.4.3 Sputtering rate

Sputtering rate describes the amount of sample material removed per unit time and hence reflects the sputtering yield at a particular set of conditions. Boumans<sup>34, 41</sup> described sputtering rate using equation 2-16.

$$Q = C_Q \cdot i_g \cdot (V_g - V_0) \quad (2-16)$$

Where  $Q$  is sputtering rate,  $i_g$  and  $V_g$  are discharge current and voltage, respectively.  $C_Q$  is a material dependent sputtering constant with unit of  $\mu\text{gW}^{-1}\text{s}^{-1}$  while  $V_0$  is threshold voltage below which there is no sputtering. The threshold voltage,  $V_0$  is described by equation 2-17.

$$V_0 = \frac{(M_1 + M_2)^2}{4M_1M_2} U_0 \quad (2-17)$$

Where  $M_1$  and  $M_2$  are the masses of impinging ion and cathode material, respectively, while  $U_0$  is the heat of sublimation.

For practical purpose, sputtering rate (Q) is related to sputtering yield (S) by following equation (2-18).<sup>34</sup>

$$S = \frac{10^{-6} Q N e}{M} \quad (2-18)$$

Where  $N$ ,  $e$  and  $M$  are Avogadro's constant, electronic charge, and atomic mass of cathode respectively.

GDMS operates in the abnormal discharge mode where, at a constant pressure, the increase in current leads to increase in voltage (Figure 2-1). The opposite, i.e., increase in voltage leads to increase in current, is also true. The non-linear behaviour of current-voltage curve as shown in Figure 2-4 is understood to be associated with sample heating in Element GD, which is normally observed at higher discharge gas pressures (Figure 2-4, left).<sup>42</sup> Further, it may also be challenging to reproduce the same current-voltage behaviour, which may alter the sputtering rates.

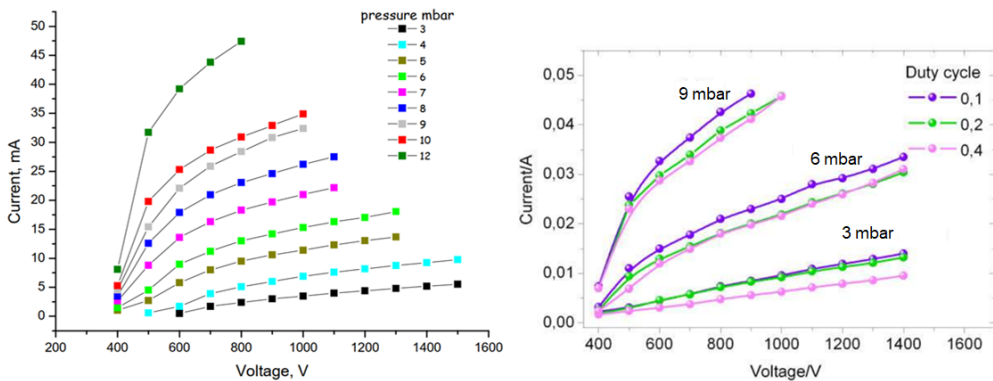


**Figure 2-4:** Current - Voltage relationship curve for continuous dc-GDMS<sup>42</sup> (left) and pulsed-dc-GDMS (right).<sup>43</sup>, reprinted from IOP publishing Copyright © 2008 and Efimova, V. PhD dissertation Copyright © 2011 Technische Universität Dresden with some modification respectively.

Efimova et al. suggested that heat generation during sputtering process can be reduced by use of pulsed mode instead of continuous direct current.<sup>43</sup> Although non-linear behaviour is also seen with pulsed-dc-GDMS at higher discharge gas

pressure<sup>43</sup>, the degree of non-linearity is less with pulsed mode (Figure 2-4, right). Further, use of pulsed mode transmitted greater instantaneous power increasing the detection sensitivity.<sup>43</sup> It is worth pointing out that slow-flow instruments (Astrum, VG9000) operate at much lower power (<5 W) as compared to fast-flow instruments, which uses 30 – 50 W. The terms fast-flow and slow-flow are used after the discharge gas flow rates. The flow rates are in range of 300 – 500 ml/min for fast-flow instrument while it is about 3-order less for slow-flow instruments.

Bogaerts et al. suggested that use of higher gas flow rates contributes to gas heating in Element GD as compared to VG9000.<sup>44</sup> Kasik carried out voltage-current characteristics using VG9000, which is a slow flow instrument with cryocooling possibility.<sup>45</sup> Although variation in voltage-current characteristics was observed with slow flow instruments, it is claimed that it is stable after some time as a result of liquid nitrogen cooling.<sup>45</sup> Hence, there are two possible ways to reduce sample heating or any possibility of elemental evaporation or non-uniform sample sputtering, i.e., either by using pulsed operation mode at lower duty cycles or using instruments with cryocooling possibility.

Besides sample heating, there are other factors that influence the sputtering rate. Further, Ferreira et al. demonstrated that there is redeposition of sputtered atoms where there is an equilibrium between sputtering and redeposition events.<sup>46</sup> This determines the shape of the sputtered crater. Placement of masks with diameter less than that of tantalum front plate anode can reduce material redeposition in the circumference of the sputtered crater.<sup>47</sup> Besides, an equipotential exists in front of the cathode which is influenced by glow discharge parameters. This equipotential can be changed by changing discharge conditions. Hence if voltage is continuously increased while keeping current constant, the crater shape changes from U-shape to W-shape (shown in Figure 2-5).<sup>48</sup> Hence, it is possible to empirically determine the discharge conditions where homogenous sputtering can be attained. Pisonero et al. performed such experiments for Element GD<sup>49</sup>, and Bogaerts for VG9000.<sup>50</sup>

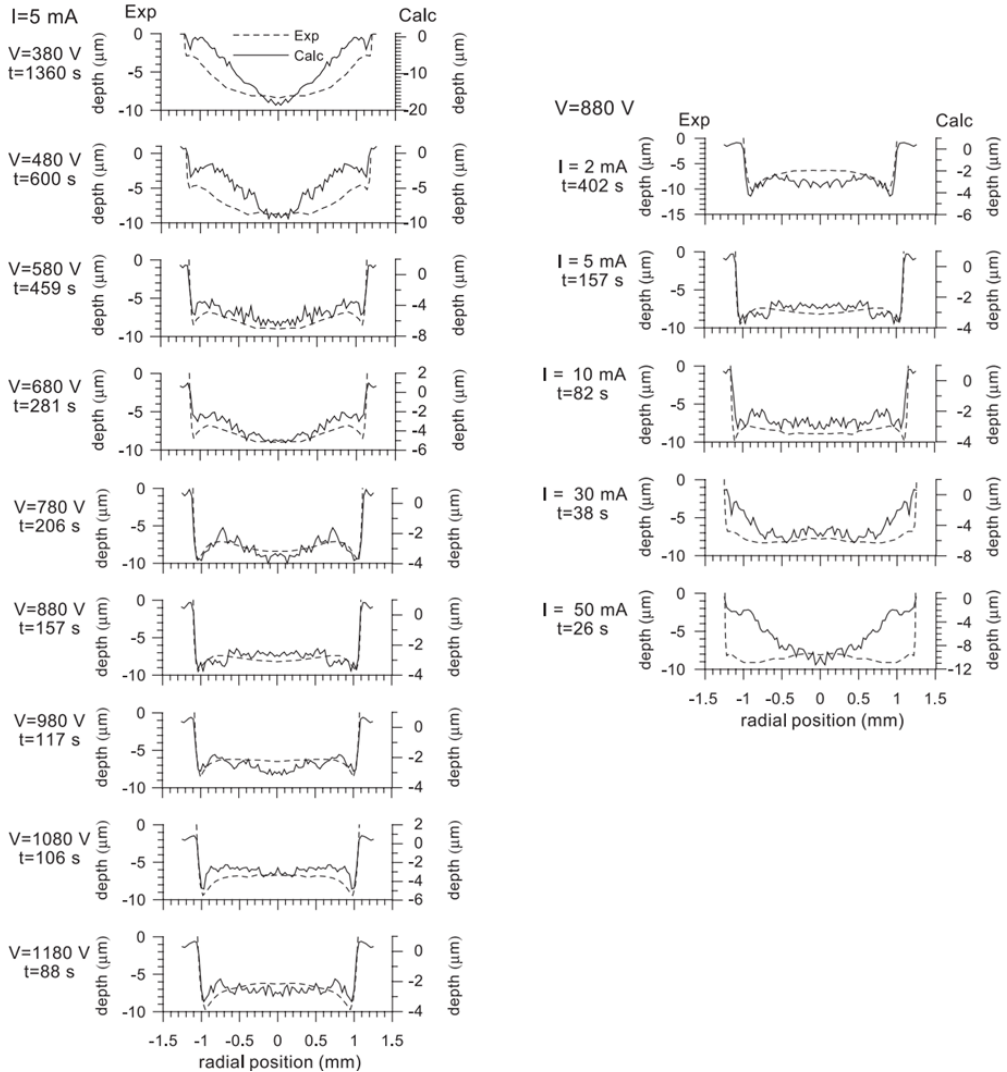


**Figure 2-5:** Evolution of crater profiles from U-shape to W-shape with change in voltage at fixed current (left panel) and change in current at fixed voltage (right panel), *reprinted with permission from*<sup>48</sup> *Copyright © 2004 Elsevier B.V.*

**CHAPTER 3**  
**Glow discharge mass spectrometry**

Glow discharge mass spectrometry (GDMS) utilizes glow discharge plasma for cathodic sputtering and ionization of atoms in the plasma. Subsequently, ions are analysed based on their mass to charge ratio leading to multi-elemental characterization of the specimen under investigation. A typical mass spectrometer consists of an ionization source, mass analyzers and detectors. In addition, supporting systems such as sampler interface, ion optics, and pumping systems support the characterization of the ions (as shown in Table 3-1). In this section, a brief overview is given about glow discharge mass spectrometry and its applications.

**Table 3-1:** Different parts of a glow discharge mass spectrometer with their role (reprinted with modifications from<sup>39</sup> Royal Society of Chemistry © 2015).

Events	Components of glow discharge mass spectrometer
Solid sample introduction	Sample introducing probe
Atoms sputtered from sample surface Ionization of sputtered atoms in GD-plasma	Glow discharge plasma
Sampling of ions from reduced pressure into higher vacuum	Interface (sampler)/skimmer cones
Acceleration, focusing and transmission of ions	Lens system
Mass to charge separation, directional and energy focusing	Electrostatic and magnetic sector field analyzers
Detection of ions	Detectors

### 3.1 Glow discharge operation modes

The glow discharge sources can be operated in either direct current (dc), radio frequency (RF) or pulsed mode of either dc or RF. The dc mode is the simplest and most common mode of operation yielding stable ion population in plasma; particularly

slow-flow/low-power sector field glow discharge mass spectrometry (SF-GDMS) is known to be a robust tool with good reproducibility<sup>51</sup>. Table 3-2 presents a list of commercially available GDMS instruments with their features. The dc mode has current, voltage and pressure (or discharge gas flow rate) as discharge parameters. The main drawback of this mode of operation is the inability to measure non-conductive samples directly as positive charge build-up due to arriving ions on the sample surface has no means to be neutralized by the flow of electrons.

**Table 3-2:** Overview of the commercially available GDMS instruments with some of their features (*reprinted from*<sup>52</sup> *Copyright © 2019 ASM International*<sup>®</sup>).

<b>Instrument</b>	<b>Samples</b>	<b>Power supply</b>	<b>Mass analyzer</b>
Element GD	Pin and flat	Direct current and micro-pulsed direct current	Sector field
Autoconcept GD 90	Pin and flat	Direct current and radio frequency	Sector field
Astrum	Pin and flat	Direct current	Sector field
Plasma profiling TOFMS	Flat	Radio frequency and pulsed radio frequency	Time of flight
Lumas 30	Combined hollow cathode	Pulsed direct current	Time of flight

On the contrary, RF mode can be used for direct analysis of non-conductive samples. RF mode uses alternating current typically at a frequency of 13.56 MHz. Hence, during each half cycle positive ions and electrons bombard the cathode surface alternatively. During negative half cycle, the positive charge build-up during positive half cycle is neutralized. In fact, higher mobility of the electrons as compared to positive ions yields negative self-bias over time allowing continuous sputtering<sup>53</sup>. Besides direct analysis of non-conductors, RF mode also generates molecular ions, hence allowing possibility to analyse polymers and organic materials<sup>54-56</sup>. The use of pulsed mode adds further variability in addition to classical discharge parameters (current, voltage and pressure). The pulse width and frequency are two additional parameters in pulsed mode<sup>43</sup>. This mode utilizes pulse duration generally applied in either millisecond or microsecond duration. The pulse mode generates higher voltage and current for the same average power as compared to continuous discharge, hence leading to higher

sputtering and intensity<sup>57-59</sup>. Further, the sample heating is reduced. Another advantage is the possibility of time-gated detection<sup>60, 61</sup>, allowing improved signal to noise ratio and reduction of interferences<sup>62</sup>.

### 3.2 Glow discharge geometries

For the generation of glow discharge, cathode and anode electrodes are required. The sample under investigation itself acts as the cathode. The property of the cathode influences the glow discharge plasma and sputtering. It is worth mentioning that the shape of the anode plays a key role in determining equipotential and influences the crater shape<sup>63</sup>. Moreover, the GD geometry determines and limits the form of sample that can be analysed. Further, the relative sensitivity factors are known to be glow discharge cell specific<sup>51, 64</sup>. The most common geometries<sup>65, 66</sup> are presented in Figure 3-1. The coaxial cathode geometry (Figure 3-1a) is a common geometry in commercial GDMS instruments allowing analysis of pin samples. This generally requires drilling or machining of samples into pin form. Further, this geometry does not allow depth profiling. The planar geometry (Figure 3-1b) is the simplest geometry for analysis of flat samples or disc samples. The Grimm-type cell geometry is a popular design available in commercial instruments. It was first invented by Grimm in 1967.<sup>67</sup> In this geometry, the distance between cathode and anode is reduced, which leads to generation of confined (restricted) discharge due to cylindrical hollow anode (Figure 3-1c). This configuration has a pumping system close to the sample, thereby reducing the redeposition of sputtered atoms. The virtue of the pumping system is the possibility to operate instruments using Grimm-type at higher pressures. Further, this feature allows homogenous sputtering under specific discharge conditions and, therefore, suited for depth profile analysis.<sup>68</sup> There has been attempts to improve the crater shape, depth resolution and analytical sensitivity by modifying the original Grimm geometry.<sup>69-71</sup>

Another popular GD geometry is the hollow-cathode, which consists of three planar cathodes placed close to each other such that the negative glow regions coalesce into a single negative glow.<sup>65, 66</sup> In this way, the sputtering and ionization processes become more effective. Alternatively, the sample can be machined to follow a hollow



cathode (Figure 3-1d). The cylindrical hollow-cathode design (Figure 3-1e) is the most popular geometry among various hollow cathode designs. Here, the sample is placed towards the end of cylindrical cathodes. The hollow cathode plume (Figure 3-1f) allows sample placement at the end of a cylindrical tube with a small opening in the middle of the sample, thus allowing plasma being pushed through the orifice.<sup>65, 66</sup> In recent years, studies have combined the Grimm cell and hollow cathode design, where the reconstructed geometry is termed as combined hollow cathode (CHC). The reconstructed geometry resulted into enhanced sensitivity for dielectric materials.<sup>72</sup> A review article<sup>73</sup> for the hollow cathode geometry and other original research articles using the commercially available instrument Lumas 30 (Table 3-2) are available.<sup>74, 75</sup>

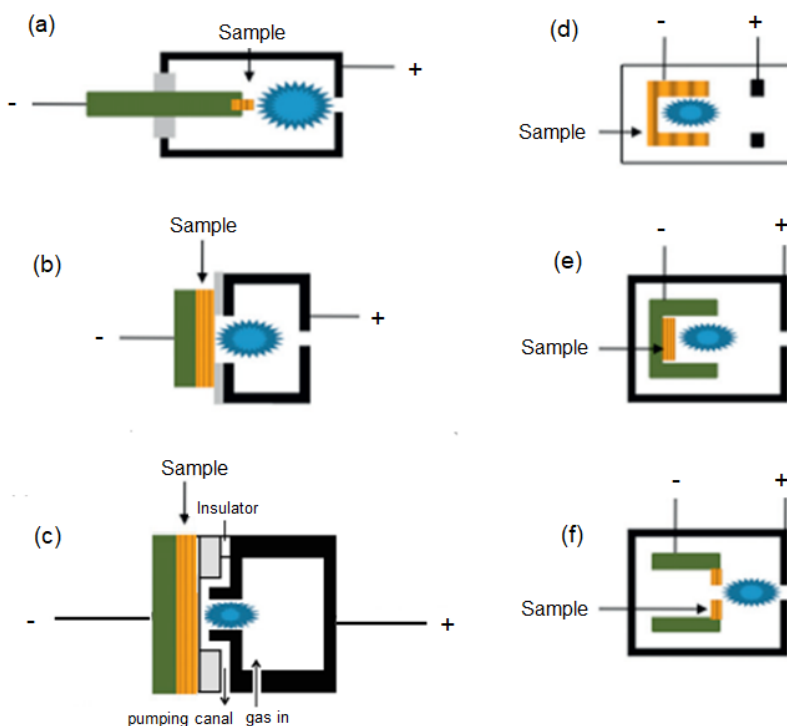


**Figure 3-1:** Diagrammatic representations of the various GD source configurations: (a) coaxial cathode, (b) planar diode, (c) Grimm-type source, (d) hollow-cathode lamp, (e) cylindrical hollow-cathode design, and (f) hollow-cathode plume (*reprinted with modification from*<sup>65</sup> © 2017 Elsevier Ltd. All rights reserved). Blue spark in each figure represents glow discharge plasma.

### 3.3 Mass analyzers

There is a wide range of analyzers, among which sector field mass analyzer and time of flight mass analyzer are available on current commercial instruments. In this section, sector field mass analyzers are presented. For other mass analyzers, readers are recommended to check the reference, Marcus and Broekaert et al.<sup>9</sup>

#### 3.3.1 Magnetic sector and double-focusing mass analyzers

A magnetic sector analyzer utilizes magnetic field to disperse ions with different mass to charge ratio ( $m/z$ ) across a focal plane. At first, the ions extracted from the ion source are accelerated into the magnetic sector by applying an acceleration voltage,  $V$ . The loss of potential energy for accelerating ions is equal to the gain in kinetic energy ( $KE$ ) described by equation 3-1.

$$KE = z e V = \frac{m v^2}{2} \quad (3-1)$$

Here “ $z$ ” is the charge number of an ion with mass “ $m$ ” moving with a velocity “ $v$ ”.

As the ions enter the sector, two forces act on them, a centripetal force,  $F_M$  as a result of magnetic field that pulls the ion inward, while a centrifugal force,  $F_C$  as a result of the acceleration voltage that pushes the ions outward (as shown in equation 3-2 and 3-3 respectively).

$$F_M = B z e v \quad (3-2)$$

$$F_C = \frac{m v^2}{r} \quad (3-3)$$

Here “ $B$ ” and “ $r$ ” are the magnetic field strength and the radius of the magnetic sector, respectively.

For any ion to pass through the magnetic sector (shown schematically in Figure 3-2), centripetal and centrifugal forces must be equal leading to following equation 3-4.

$$B z e v = \frac{mv^2}{r} \quad (3-4)$$

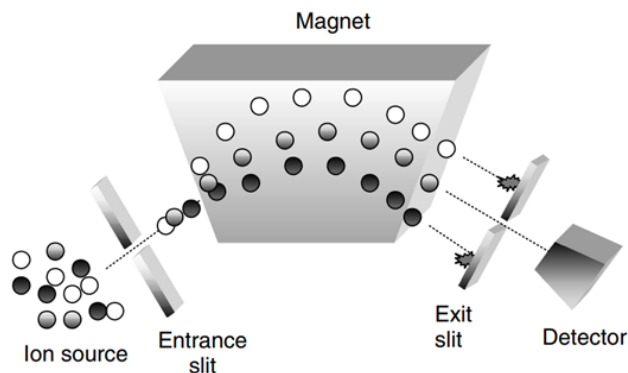


**Figure 3-2:** Single focusing magnetic sector analyzer (reprinted with permission from<sup>9</sup> Copyright © 2003 John Wiley & Sons, Ltd).

The equations 3-1 and 3-4 are rearranged after canceling out velocity to express it in terms of  $m/z$  as equation 3-5. Hence, mass spectrum with different  $m/z$  can be achieved by modifying one parameter while keeping other two variables constant.

$$\frac{m}{z} = \frac{B^2 r^2 e}{2V} \quad (3-5)$$

It is worth mentioning that the magnetic sector does not correct for the velocity distribution prior to acceleration of ions. Hence, ions with same mass but different velocity will have different “ $r$ ”. This leads to the broadening of peaks and poor resolution. Hence a double focusing mass analyzer with electrostatic sector prior to the magnetic sector is needed to correct for the velocity spread. A schematic view of the double focusing analyzer i.e., electrostatic analyzer and magnetic sector analyzer are shown in Figure 3-3.

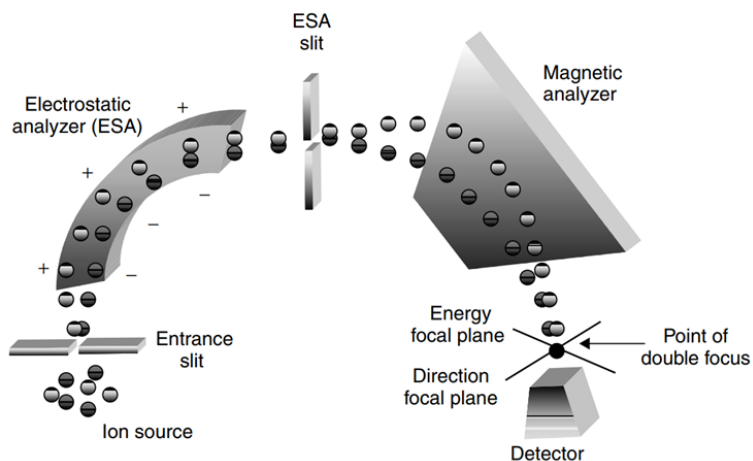


**Figure 3-3:** Double focusing analyzer- electrostatic analyzer and magnetic sector analyzer coupled in Neir-Johnson geometry (reprinted with permission from<sup>9</sup> *Copyright © 2003 John Wiley & Sons, Ltd*).

An ion entering an electrostatic field of strength  $E$  can pass through an electrostatic sector of radius  $r$  if the electrostatic force is equal to the centrifugal force expressed as equation 3-6.

$$\frac{m v^2}{r} = e z E \quad (3-6)$$

Here, the ions are focused for their energy regardless of their velocity and then the magnetic sector focuses ions in terms of  $m/z$  ratio, thereby leading to better resolved peaks.

### 3.4 Quantification approaches in GDMS

There are either semi-quantitative or quantitative approaches in GDMS. The merits and drawbacks of these approaches are introduced shortly.

#### 3.4.1 Ion beam ratio

The ion beam ratio is a semi-quantitative approach, which considers the ratio of the abundance corrected analyte intensity with respect to abundance corrected matrix intensity (equation 3-7). This is referred to as the abundance corrected ion beam ratio ( $IBR_{X/M}$ ). Here,  $C_{X/M}$  is the mass fraction of element/isotope  $x$  present in matrix  $M$ , while  $I_{xi}$ ,  $A_{xi}$  and  $I_{Mi}$ ,  $A_{Mi}$  represent the intensity and natural abundance of analyte and matrix, respectively. This approach of quantification does not consider the matrix effect and processes occurring in the plasma. Therefore, this approach results into high uncertainty<sup>76</sup> and is less used.

$$C_{X/M} = \frac{I_{xi}}{I_{Mi}} \times \frac{A_{Mi}}{A_{xi}} = IBR_{X/M} \quad (3-7)$$

#### 3.4.2 Calibrated materials and relative sensitivity factors

To reduce the uncertainty caused by the variation due to sputtering, diffusion, ionization, transmission, and detection of ion species, use of standards is necessary.<sup>77</sup> As discharge condition is one of the fundamental factors affecting each of these processes, same operating conditions should be used. Further, discharge gas, the GD ion source and similar matrix composition of standards should be considered. Thus, a correction factor termed as relative sensitivity factor (RSF) is multiplied to the abundance corrected ion beam ratio considering all the events explained above as incorporated into equation 3-8.

$$C_{X/M} = \frac{I_{xi}}{I_{Mi}} \times \frac{A_{Mi}}{A_{xi}} \times RSF_{X/M} = IBR_{X/M} \times RSF_{X/M} \quad (3-8)$$

$RSF_{X/M}$  represents the relative sensitivity factor of a specific analyte  $x$  present in a specific matrix  $M$ . RSFs are estimated mathematically as inverse of the slope of calibration curve  $IBR_{X/M'}$  versus mass fraction  $C_{X/M'}$  (equation 3-9). The ion

beam ratio  $IBR_{X/M}$  is generated by measurement of calibrated reference material (CRM), reference material (RM) or synthetic standards by GDMS.  $C_{X/M}$  is the reported value in the certificate of CRM during its procurement and is usually certified by a range of different analytical techniques. Most of the values in RM are determined by measurements based on other complimentary analytical techniques, which in turn are calibrated by other certified materials.

$$RSF_{X/M} = \frac{C_{X/M}}{IBR_{X/M}} \quad (3-9)$$

It is important to emphasize that multiple calibrated materials are recommended to determine RSFs. However, alternatively, on limited availability of calibrated materials, RSFs are calculated based on single calibrated material with origin (zero intercept) as a second point.<sup>78</sup> The latter approach can be used as high resolution GDMS instrument usually generates low blank values due to virtually no detector background and minimal memory effects (except for gaseous elements). There could be deviations from this as linear calibration curve using multiple synthetic standards result into an intercept.<sup>79</sup> Nevertheless, due to limited availability of CRM and RM, particularly in  $\mu\text{g}/\text{kg}$  level, and unsuitability of preparing synthetic standards, a linear curve passing through origin is widely expected/assumed.

### 3.4.3 Standard relative sensitivity factors

To compensate the problem of limited availability of CRM, RM or synthetic standards, semi-quantitative approach of quantifying with standard RSF ( $\text{stdRSF}_x$ ) can also be adopted (equation 3-10). The standard RSF values represent a set of universal RSFs values derived from measurements of CRM and RM of various matrices. The standard RSF values are normalized to iron. Iron is used as a reference point as it is certified in almost all CRMs and RMs. Certified materials are known to contain iron as a major, minor or trace impurity element. The uncertainty associated with this approach is less as compared to that of the ion beam ratio approach.<sup>76</sup>

$$stdRSF_x = \frac{RSF_{x/M}}{RSF_{Fe/M}} = \frac{I_{Fe}}{I_x} \times \frac{C_{x/M}}{C_{Fe/M}} \quad (3-10)$$

where  $stdRSF_x$  is a standard RSF of an element/isotope  $x$ .  $RSF_{x/M}$  and  $RSF_{Fe/M}$  represent RSF of element/isotope  $x$  and  $Fe$  in matrix  $M$ , respectively.  $I_{Fe}$  and  $I_x$  refer to the abundance corrected intensity of iron and isotope of interest respectively.  $C_{x/M}$  and  $C_{Fe/M}$  represent the mass fraction of a trace element/isotope  $x$  and iron present in matrix  $M$ , respectively.

## 3.5 Applications

In general, glow discharge mass spectrometry offers two major applications, bulk analysis and depth profiling. Both applications are presented below.

### 3.5.1 Bulk analysis

The prerequisite for bulk analysis is sufficiently homogenous sample material with evenly distributed impurities. Besides homogeneity, signal stability is also important. Prior to data acquisition, it is usually recommended to test homogeneity and signal stability. Further, cleaning of the sample surface by use of etchants and pre-sputtering is a common practice for removal of surface contamination. After this is assured, bulk data analysis is acquired. Literature review of bulk analysis of metals, semiconductors, powders, non-conductive samples are briefly mentioned.

#### A. Metals

Sector field glow discharge mass spectrometry provides wide dynamic range with detection limits down to sub-ppb levels and provides possibility of accurate quantification after RSFs are used. This makes it suitable for industrial quality control applications of high purity metals and reference materials where multielement characterization is desired.<sup>80, 81</sup> Likewise, GDMS is also used for characterization of precious metals.<sup>82, 83</sup>

For accurate quantification, relative sensitivity factors are available for aluminum and magnesium<sup>84</sup>, copper<sup>85-87</sup>, zinc<sup>76, 85</sup>. Moreover, considering limited availability of CRMs and RMs, matrix independent calibration approaches are also investigated.<sup>88-90</sup> Therefore, GDMS can be a method of choice where finding appropriate reference material is a problem, e.g. in LA-ICPMS or SIMS analysis.<sup>91</sup> Further round-robin analysis are available for some metals, for instance aluminum<sup>51</sup> and copper.<sup>64</sup> Likewise, comparison of copper analysis with several other techniques such as ICP-OES, ICP-MS, spark source etc. is available.<sup>92</sup>



## **B. Bulk analysis for solar cell silicon applications**

GDMS bulk analysis is widely used for photovoltaic applications. There are several publications reporting the decrease of solar cell efficiency in the presence of impurity elements in the range of few ppb to several ppb.<sup>93-95</sup> The ability of sector field GDMS to detect impurities in this range allows quality control of feedstock material, crucible, and coating materials used for making silicon ingots. Di Sabatino et al. have measured limits of detection<sup>96</sup> for solar cell silicon application and RSF determination for flat shaped samples using Element GD.<sup>78</sup> This was performed for p- and n- type doped silicon ingots. Further, Zhang et al. determined RSF using a different approach.<sup>97</sup> For this silicon powders with various impurity content were used to generate silicon tablets, which were analysed by Element GD.

## **C. Powders**

Powders as such cannot be analysed directly. It should be processed into a different form that can be accommodated into the GDMS, i.e., pin<sup>83, 98</sup> or discs.<sup>99, 100</sup> Alternatively, it could be pressed or placed onto a mechanical support such as metal sheets<sup>101, 102</sup> or comb/spoon, respectively. If the amount of sample powder is not sufficient for processing into a measurable sample form, then pure powder can be used in different proportions as filler material.<sup>9</sup> However, use of filler material introduces other analytical variables which could influence the mechanical stability or effectiveness of final material analysis. For instance, different ratios of analyte to host powder mixture can lead to changes in sputtering rate.<sup>9</sup> For analysis of powders where limit of detection is critical, cleaner filler material is the obvious choice. Recently in 2019, Dong et al. developed a porous cage carrier method for analysis of soil samples in pin geometry.<sup>103</sup> The authors used tantalum sheets of 5N purity to make a carrier with a circular cross-sectional area in the range from 20 to 38 mm<sup>2</sup>, length from 15 to 17 mm and diameter of hole size from 1.5 mm to 2.0 mm.

## **D. Non-conductive samples**

Non-conductive samples should be analysed by either RF-GDMS or their conductivity should be sufficiently increased so that the charge build-up during sputtering process

is neutralized. Milton and Hutton developed the secondary cathode approach, where a conductive mask is placed over the sample material to be analysed.<sup>104</sup> In this approach during the sputtering process, a conductive film is produced above the non-conductive sample which then sustains the sputtering process.<sup>104</sup> This approach is successfully applied for analysis of nuclear samples.<sup>105, 106</sup> Qian et al. demonstrated that coating at the sample surface is also a suitable approach to analyse non-conductive sample.<sup>107</sup>

### 3.5.2 Depth profiling

Depth profiling allows measuring the change in concentration as function of the sample depth. It is an approach particularly recommend for inhomogeneous or layered materials. For obtaining an optimum depth profile, the shape of the crater is important. This should be preferably with flat bottom and steep walls perpendicular to the surface. Crater shape is demonstrated to be related with operational parameters such as current, voltage and pressure, which can be changed empirically to obtain optimum crater with flat bottom.<sup>48, 50</sup> These parameters are understood to influence the equipotential in front of the sample material being sputtered which can be changed by changing the discharge parameters.<sup>48</sup>

For obtaining optimum depth resolution, besides the crater shape, the crater roughness at the bottom plays a crucial role. Roughness can depend on several parameters such as indentations due to impinging ions<sup>108</sup>, differences in sputtering yield of one element compared to other.<sup>11</sup>

It is generally agreed that RF-TOF-GDMS is better than sector field GDMS for depth profiling if low detection limits are not required. The major reason is that SF-GDMS uses sequential detection which is slow. TOF analyzers which are fast allow acquiring a full spectrum quasi-simultaneously. PP-TOF-GDMS introduced by Horiba Scientific in 2014 allows RF- and pulsed mode. There are several works reported for analysis of thin (10-100 nm) and ultrathin (<10 nm) layers, as reported in references given here.<sup>109, 110</sup> Likewise, in 2020, using  $\mu$ s-pulsed dc-combined hollow cathode GD geometry coupled with TOF mass analyzer, Gubal et al. profiled impurity content in

both dielectric and conductive samples.<sup>111</sup> Despite all of its advantages, a major limitation is that GDMS instruments relying on TOF analyzers provide detection limit in ppm level as compared to sector field instruments which can detect up to sub-ppb levels. There are in-house GDMS instruments using quadrupole as mass analyzer which is also regarded as fast analyzer as compared to sector field. Depth profiling using quadrupole based instruments is performed for ion implanted sample<sup>112</sup> and hard coatings.<sup>113</sup>

Despite of the limitations of slow data acquisition, sector field GDMS is still preferred for applications such as solar cell research, where sub-ppb levels of impurity detection is desired. Di Sabatino et al. used Element GD for profiling impurities present in silicon analysing several trace impurities at ppb-levels.<sup>114</sup> Further, using the same instrument copper diffusion in silicon substrate was profiled.<sup>40</sup> Other relevant works using sector field GDMS include profiling of elements in nickel-based superalloys<sup>115</sup> and profiling of aluminide coatings.<sup>116, 117</sup>

### 3.6 Glow discharge mass spectrometry as compared to other techniques

Solid sampling analytical techniques allow direct measurement of solid samples. Such techniques have clear advantages over other techniques, which require dissolving of solid samples into liquid form for instance, inductively coupled plasma mass spectrometry (ICP-MS). The sample dissolution may lead to analyte loss and may be a source of undesired contamination. Based on excitation source, in general solid sampling techniques can be classified as electron probe, X-ray probe, laser probe, ion probe, and plasma-based methods.<sup>9</sup>

The electron probe methods such as Auger electron spectroscopy (AES) and electron probe micro analyzer (EPMA) use high-energy electrons of tens of kilovolts for analysing samples. The impinging of electrons into sample surface results in generation of Auger electrons and characteristic X-rays, respectively. AES offers the advantage of excellent lateral and spatial resolution (~ 10 nm), provides high-resolution elemental maps, and can be used for depth profiling of top layers (<10 nm). The major drawback is that the detection limits are in order of percent. EPMA can measure elements up to several ppm but is essentially a bulk analytical technique.<sup>118</sup>

An X-ray probe method, which is complimentary to AES, is X-ray photoelectron spectroscopy (XPS). XPS has less sample charging issue, generates better signal to noise ratio and can analyse insulating materials and does less damage to the sample surface as compared to AES.<sup>119</sup> It can provide chemical bonding information and has comparable detection limit as AES. In terms of detection limits, X-ray fluorescence spectrometry can detect in order of 10-50 ppm.

In terms of detection limits, the instruments that can come close to GDMS are laser ablation inductively coupled plasma mass spectrometry (LA-ICP-MS) and secondary ion mass spectrometry (SIMS). LA-ICP-MS uses short pulse high power laser beam to evaporate a sample in an inert gas at atmospheric pressure. Generated aerosol is flushed by carrier gas into the ICP-MS where it is vaporized, atomized and ionized. The fact that atomization and ionization are separated in space and time makes it

possible to use matrix independent calibration approach for quantification. SIMS utilizes a focused ion beam to sputter the sample. Due to complex physical processes of ionization and sputtering, generally SIMS requires use of matrix matched standards in contrary to GDMS where non-matrix matched standards is much more established.<sup>90</sup> Another technique is sputtered neutral mass spectrometry (SNMS), which uses laser or electron induced ionization of sputtered atoms. Hence, this technique suffers less problem as compared to SIMS for producing specific matrix matched standards close to sample composition. The other major drawback of SIMS is the need of ultra-high vacuum as the probing ions are often scattered. Therefore, poor vacuum conditions lead to reduced signal to noise ratio and also requires longer analysis time. The virtue of SIMS is excellent lateral and depth resolution. LA-ICP-MS also provides good lateral and depth resolution, however, suffers problem with accuracy and precision. The reason being the aerosol generation and transport is not fully reproducible. Further, generation and transport of aerosol is dependent on aerosol particle size hence contributing to strong matrix effects.<sup>91</sup> The major drawback of GDMS as compared to LA-ICP-MS and SIMS is poor lateral resolution. Further, both LA-ICP-MS and SIMS/SNMS are also popular for analysing complex matrices such as biological samples.<sup>120-123</sup> A comparison of the various characteristics of GDMS, LA-ICP-MS and SIMS/SNMS are presented in Table 3-3.

The other plasma-based technique besides GDMS is glow discharge optical emission spectroscopy (GDOES), which is an established depth profiling technique with wide applications but it can only detect down to ppm level.<sup>9</sup> The spark and arc based glow discharge are sensitive techniques mainly used for bulk analysis but are understood to be erratic in terms of reproducibility.<sup>9</sup>

**Table 3-3** Comparison of various features of GDMS, LA-ICP-MS and SIMS/SNMS  
(reprinted with permission from<sup>91</sup> © The Royal Society of Chemistry 2009).

	GD-MS	LA-ICP-MS	SIMS/SNMS
Analytical Information	Elemental/Molecular Isotopic	Elemental Isotopic	Elemental/Molecular Isotopic
Sample Vacuum Conditions	1–10 torr	760 torr (atmospheric)	<10–8 torr
Sample Throughput	~min/sample	~min/sample	~hour/sample
Depth Resolution	~nm	~100 nm	≅nm
Lateral Resolution	~mm	~μm	≅100 nm
Limits of Detection	≅μg/g	μg/g–ng/g	≅ng/g
Quantitative Analysis	Possible use of matrix and non-matrix matched calibration samples	Generally, matrix-matched calibration samples	Matrix-matched calibration samples required
Sample Size and Shape Requirements	Usually, flat surface with an area bigger than the GD anode diameter (4–8 mm)	Generally, limited by size of ablation cell.	Limited by size of sample holder
Typical sample consumption	(100 ng–100 μg)	(10 pg–100 ng)	(pg–ng)
Typical precision values	<3%	<5%	<10%
More information on sample requirements	Conductivity for dc-GD; Press pellets for the analysis of powders; Porous samples require special holder	Stable form (solid or pressed powder and dry or cooled-frozen)	Suitable for high vacuum conditions; usually flat surface; cells usually cryofixed and freeze-dried before embedding in resin

**CHAPTER 4**  
**Astrum GDMS**

## 4.1 Introduction

Astrum glow discharge mass spectrometer was first introduced in 2010. It has low pressure ion source similar to VG9000 and offers cryocooling possibility. The mass spectrometer has double focusing mass analyzers, i.e., electrostatic analyzer and magnetic analyzer coupled in Neir-Johnson geometry (schematically shown in Figure 4-1). The dual detection system with Faraday cup and electron multiplier covers wide dynamic range from percentage down to sup-ppb level of concentration. The instrument has operator definable, software driven variable source and collector slit assembly that offers resolving power in range of 300 to 10,000.<sup>124</sup> There are two valves among which first valve separates sample loading and glow discharge chamber. The second valve separates glow discharge chamber from the transfer region of the mass spectrometer. A rotary pump evacuates the sample-loading chamber while turbo-molecular pumps backed up by rotary pump evacuate the glow discharge chamber and transfer region. The sample exchange is an efficient process requiring about 2-3 minutes including the venting and pumping of sample loading chamber.

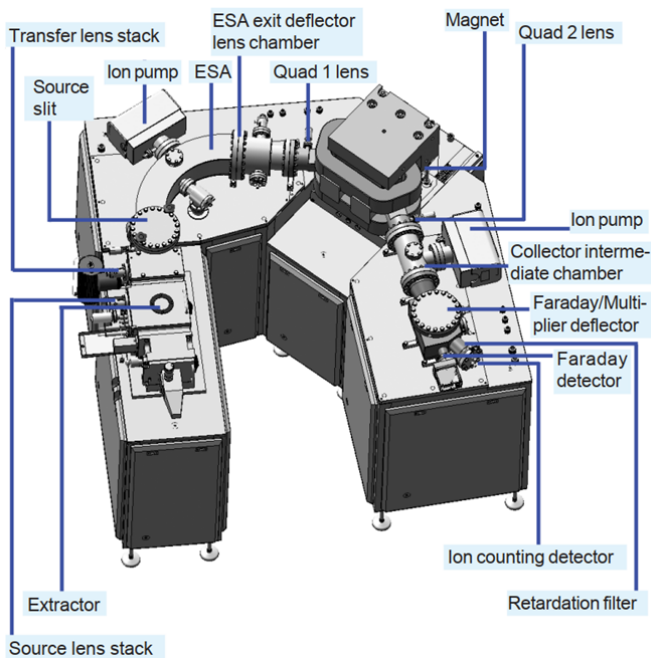


**Figure 4-1:** Schematic view of Astrum GDMS (reprinted from<sup>124</sup> © Nu Instruments UK, System Manual, Issue 1.1.1).



## 4.2 Operation of glow discharge

Astrum GDMS is powered by continuous direct current. For this type of instrument glow discharge current, voltage and discharge gas flow rate are the operating parameters. Astrum GDMS allows current, and voltage input up to 8 mA and 2 kV, respectively. The rate of discharge gas flow depends on the type of geometry used, glow discharge current and voltage setting desired as well as on the material property, e.g., the electrical conductivity of the sample. The typical flow rates fall within the range of 0.2 – 0.8 ml/min for standard operating conditions of 2 mA, 1 kV with pin geometry requiring slightly higher flow rate as compared to flat geometry.

Among three GD parameters (current, voltage and discharge gas flow) only combination of two can be controlled independently, i.e., current and discharge gas flow or voltage and discharge gas flow. The third parameter (voltage or current respectively) are dependent. Once two independent parameters are setup into the glow discharge software setting, the dependent parameter results as a readback value. However, the upper limit of the dependent parameter (third parameter) should also be defined in the software setting, which may slightly fluctuate, i.e., voltage in constant current mode (current and discharge gas flow independent) and current in constant voltage mode (voltage and discharge gas flow independent). The ions generated in the proximity of the cell exit orifice are extracted and consequently accelerated by voltage of about 6 kV towards the mass analyzer.

### 4.3 Tuning of the Astrum GDMS

The ion trajectories and beam shape are not well defined after extraction from the glow discharge cell. A series of ion optics lenses referred to as source lens stack (source V1 and source H1) and transfer lens stack (transfer H1 and H2, transfer V1 and V2, transfer horizontal and vertical lenses) are placed (shown in Figure 4-2) to focus and shape the ion beam at various stages of the mass spectrometer. The series of horizontal and vertical lenses orient the ion beam horizontally and vertically, where the aim is to supply optimum ion beam shape with maximum transmission onto the source slit. A rectangular beam is preferred over circular beam for maximum transmission.<sup>124</sup> The input values to the lenses are user defined through software. After the adjustable source slit, the ion beam is shaped by ion optic element Ent H1 before entering the electrostatic analyzer.

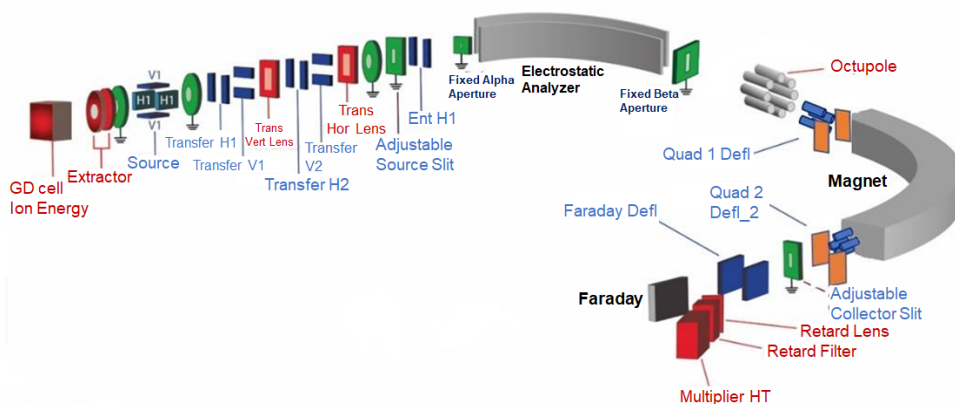


**Figure 4-2:** Schematic representation of beam path of Astrum GDMS (*reprinted with modifications from*<sup>124</sup> © Nu Instruments UK, System Manual, Issue 1.1.1).

The electrostatic analyzer section consists of an electrostatic analyzer (ESA) and fixed apertures. A flight tube section between the ESA and the magnet consists of an octupole. The magnet section consists of two quadrupoles referred to as Quad 1 and Quad 2 before and after the magnetic sector and the lenses deflector 1 and deflector 2 after each quadrupole. The collector chamber consists of adjustable collector slit and finally the detector chamber consisting of a Faraday cup, electron multiplier, deflector lenses, retardation filter and lens assembly.

The ion peak shape is important for the resolution. The ESA corrects for the ion energy spread particularly by removing low energy ions that appears at low mass side of a peak hence allowing only a narrow range of ions to pass through the ESA. Additionally, through the software it is possible to correct for the ion beam curvature and rotation in the octupole setting. The magnet is calibrated for various masses, i.e.,  $^{12}\text{C}^+$ ,  $(^{40}\text{Ar})^{2+}$ ,  $^{36}\text{Ar}^+$ ,  $(^{40}\text{Ar})_2^+$ ,  $(^{40}\text{Ar})_3^+$ ,  $^{181}\text{Ta}^+$ ,  $^{181}\text{Ta}+^{40}\text{Ar}^+$  using tantalum matrix where each of these species can be adjusted for their specific quadrupole 2 (Quad 2) value. In general, both Quad 1 and Quad 2 values determine the final peak shape. However, in practice Quad 1 is kept fixed and is instrument specific while Quad 2 is adjusted for ion peak shape.

The ion beam enters the magnetic sector where ions are separated based on their mass to charge ratio. The ion with lighter  $m/z$  has larger deflection. The ion with specific mass to charge ratio are selected by the magnetic field. This follows diversion of ion towards the detectors after exiting the magnetic sector. This feature of magnetic sector makes it a sequential analyzer. The magnet can work in the range of 1 to 300  $m/z$ .

The deflector lens setting directs the ion beam either to the Faraday cup or to the secondary electron multiplier where values are observed to be about + 3 V and -162 V, respectively. The electron multiplier measures intensities less than  $2 \times 10^6$  counts per second (cps) or  $3.2 \times 10^{-13}$  A as 1 cps is equivalent to  $1.6 \times 10^{-19}$  A. Hence, Faraday cup is used for ions with intensity above  $3.2 \times 10^{-13}$  A. Both detectors, the Faraday cup and the electron multiplier, must be cross calibrated. The ion count efficiency (ICE) is calculated based on signal of  $^{180}\text{Ta}^+$  and  $^{181}\text{Ta}^+$ , which are detected by electron multiplier and Faraday cup, respectively. This ratio of intensities is typically observed to be over 75%, which is inserted to the instrument method and is automatically taken into consideration during concentration determination of impurity elements. The ICE has to be measured regularly as its value may reduce over time due to degradation of electron multiplier. The voltage of Multiplier HT in the instrument setting is increased to compensate for the decline in ICE.

Besides, the retardation filter and lens assembly have voltages below 6 kV and 4.6 kV, respectively. These values are acceleration and extraction potential respectively. This assembly corrects for the abundance sensitivity which affects accuracy and precision of low intensity peaks for instance in the mass range of high intensity peak or matrix signal. There are also settings (IC-Disc) for reducing the instrument noise so that the detection sensitivity can be improved.

#### 4.4 Glow discharge cell and sample holder

Astrum uses slow-flow/low-power glow discharge cell similar to VG9000. Two different geometries of GD cell each for flat and pin sample analysis are presented in Figure 4-3. Powder samples can also be analysed by Astrum either by pressing it against a high purity metal sheet to be analysed in flat geometry or by producing pins and thus to be analysed in pin geometry.

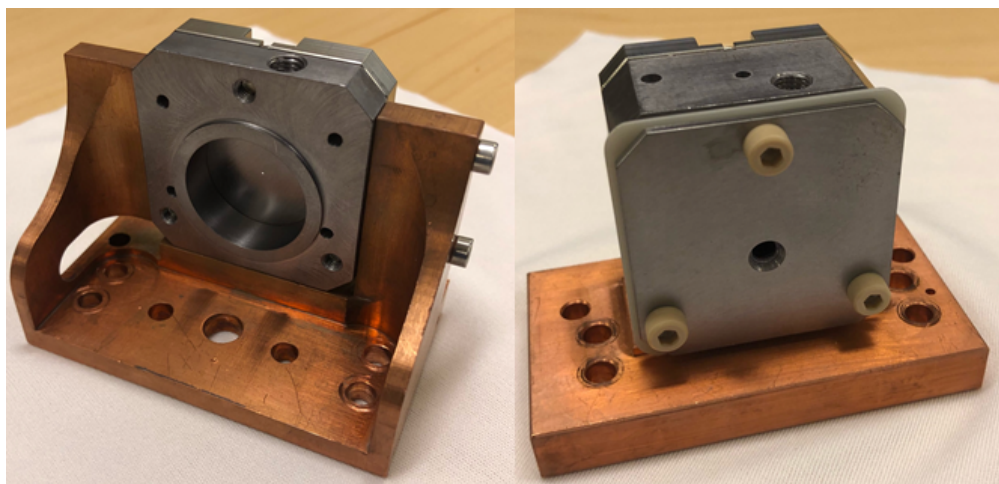


**Figure 4-3:** Images of flat (left) and pin (right) glow discharge cell geometry of Astrum GDMS, respectively.

The sample holder for analysis of flat and pin samples are presented as Figure 4-4. The main body of the discharge cell that is exposed to plasma is made up of tantalum. Insulator alumina ceramics are placed to separate cathode and anode part of the glow discharge cell. For analysis of different matrices, it is recommended to use different

sets of GD cell and the sample holders. The tantalum parts of the GD cell and sample holders can be etch cleaned firstly with hydrogen fluoride followed by heating up of tantalum parts at 80 °C in aqua-regia (1:3 ratio of nitric acid to hydrochloric acid) and rinsing with deionized water.

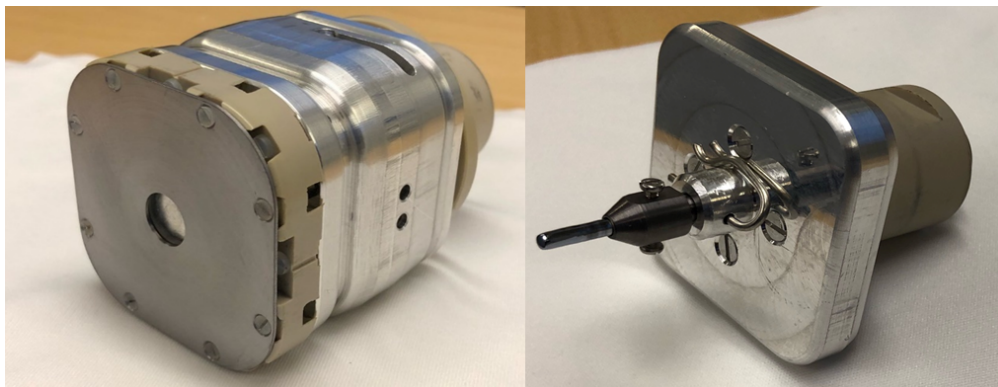


**Figure 4-4:** Images of flat (left) and pin (right) sample holders for of Astrum GDMS, respectively.

Similarly, for trace elemental analysis it is recommended to clean etch tantalum parts of source lens stack. The tantalum parts are presented in Figure 4-5.

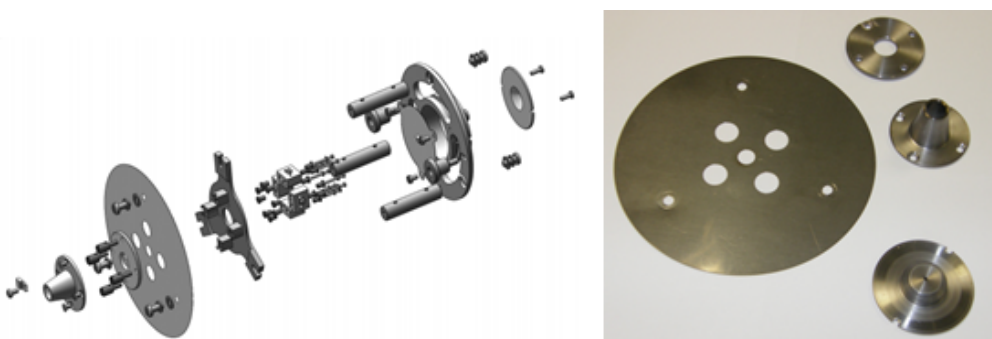


**Figure 4-5:** Schematic view of source lens stack (left) and image of tantalum parts of source lens stack that can be etched (right), respectively (*reprinted from*<sup>124</sup>, © Nu Instruments UK, System Manual, Issue 1.1.1).

**CHAPTER 5**  
**Summary of Papers**

## 5.1 Paper I: Tantalum pin analysis

Astrum GDMS is a new instrument with only few works published.<sup>32, 125</sup> Further, until results from this PhD thesis were published there were no data presenting relative sensitivity factors or approaches to measure them in a systematic way using Astrum GDMS. This work allowed to set up a necessary foundation for measurement of RSFs for other matrices presented in this thesis.

Relative sensitivity factors depend on several variables, for instance glow discharge cell geometry, shape of anode, boundary conditions such as sample holder and diameter of anode front plate, and matrix composition. Further, RSFs are strongly influenced by glow discharge parameters, referred to as glow discharge current, -voltage and -gas flow. Given the limited data regarding glow discharge operational parameters for Astrum GDMS, it was important to study the influence of discharge parameters for change in concentration of impurities, while keeping all other parameters described above constant. Further, a novel approach of relating change in concentration of elements to their absolute intensity and that of discharge gas as a function of change in discharge parameters is discussed. Therefore, an experimental setup was designed where a sufficiently homogenous tantalum pin sample of >99.95% purity was chosen. The sample was screened for the entire periodic table for signal stability based on which sodium, silicon, phosphorous, niobium, tantalum, oxygen and argon were found to be stable and, hence, suitable for further analysis. To ensure that the change in concentration and absolute intensity of impurity elements are solely due to influence of discharge parameters, the stability of the same set of elements was tested again. The stable signal confirms that the change in concentration/absolute intensity is due to influence of change in discharge parameters.

The results of the study indicate that the changes in concentration of impurity elements depend on unequal changes in absolute intensity of impurity elements to that of matrix ion (tantalum) signal. Remarkably, the concentration and absolute intensity changes of silicon and phosphorus in the range of 0.5 – 5 mA at 1 kV and 3 mA at 0.6 – 1.5 kV demonstrated similar trend to that of oxygen in similar current and voltage setting. This

indicates the likelihood of phosphorus and silicon being predominantly ionized by electron impact as oxygen can only be ionized by electron impact. This can be explained through the relatively high first ionization energy of silicon (8.15 eV) and phosphorous (10.49 eV). The change of the absolute intensity of argon is also consistent with this finding. The change in ion beam ratio of argon, carbon and nitrogen agrees with the quantification changes of oxygen.

The concentration changes of sodium and niobium do not exhibit the same trend as for silicon and phosphorous. Sodium is negatively correlated to argon and oxygen at changing current, while niobium is negatively correlated to argon and has low positive correlation with oxygen. Hence, the ionization pattern of these two elements (Na and Nb) is likely to be different. The low first ionization energy of sodium (5.14 eV) might indicate the dominance of Penning ionization over electron impact. Niobium and tantalum share similar first ionization energy and its negative correlation with argon and oxygen seems to indicate that niobium and tantalum might ionize by similar ionization mechanism, predominantly Penning ionization. A similar study, published around the same time using Element GD, suggested that the change in concentration of elements with change in discharge condition can be linked to differences in atomic masses of ions.<sup>88</sup> Nevertheless, it is clear from the study that measuring of absolute intensity of elements and matrix ion as well as plotting of intensity of discharge gas can provide useful hints on ionization mechanisms of some elements. Interestingly, the correlation study indicates that changing the voltage do not influence signal of elements as compared to changing current, as all elements have high correlation value of > 0.8. Hence, keeping constant current is most likely the best approach for this type of analysis.

The internal reproducibility as a result of repetitive measurements in a single analysis was about ~5%. The external reproducibility as a result of sample exchange was < 10% for most discharge settings. Further, at low discharge gas flow close to 0.2 ml/min, particularly for phosphorus, the external reproducibility was higher than 10%.



## 5.2 Paper II: Silicon powder analysis

Paper II builds-up on the findings of paper I and is an extension of the work using a different sample form (powder) and matrix (silicon) analysed in a flat cell geometry. In this work, RSFs are calculated, and this is crucial for accurate measurement of impurities in silicon powders.

Before the measurements were done, stability of most of elements were ensured using indium sheet for mechanical support of silicon powders. Relevant impurity elements for solar cell silicon application were selected for optimization of discharge condition before RSFs were determined. For this, elements such as boron, phosphorous, cobalt, aluminum, iron, chromium, and copper were subjected to a much wider range of current and voltage setting (1 – 3.5 mA, 1 – 1.4 kV) using similar concept as in Paper I to study the change in concentration and intensity of impurity elements. The concentration of elements varies as a function of change in discharge setting, however, is largely unchanged for most of the elements in the range of 2 – 3 mA, 1.2 – 1.4 kV. Change in quantification and intensity of argon and oxygen is carried out in glow discharge current and voltage range of 1 – 5 mA and 1.2 – 1.6 kV to study if plotting of discharge parameters could be helpful for selecting optimum discharge condition for measuring RSFs.

The results demonstrate that the change in argon quantification is more or less unchanged in discharge setting of 2 – 3 mA and 1.2 – 1.4 kV. Further, beyond 3 mA in the range of 1.2 – 1.6 kV, argon quantification steadily increases while up to 2 mA in the same voltage range it is slightly decreasing. As concentration of impurity elements or argon is calculated in reference to silicon (matrix element), it is likely that in 2 – 3 mA and 1.2 – 1.4 kV all of the elements are ionized in a similar manner. As argon has much higher first ionization as compared to other elements, increase in power at higher discharge condition is a plausible explanation to the increase in quantification beyond 3 mA in 1.2 – 1.6 kV range. The slight decrease in argon quantification until 2 mA can possibly be related to increase in sputtering rate, thereby increasing the population of silicon ions. In addition, to check if this observation is consistent, a silicon sample was analysed in same geometry as was used for silicon

powder, i.e., flat geometry. Indeed, both oxygen and argon show the same trend. Therefore, at least for silicon matrix, it would be reasonable to state that measuring quantification of discharge gas or other elements that ionizes by electron impact can assist to determine the optimum discharge condition where concentration remains more or less unchanged. Similar work on other matrices should be carried to generalize this finding. Further, the discharge condition (2.3 mA, 0.7 kV) for obtaining optimum crater in silicon flat sample was considered before selecting optimum discharge condition for RSFs. Hence, 2.3 mA, 1.2 kV was selected to determine RSFs, which lies within discharge condition of 2 – 3 mA, 1.2 – 1.4 kV.

The RSFs were determined for 16 elements using silicon 57b certified powder and verified using certified values of 195 silicon powder both procured from National Institute of Standards and Technology (NIST, Maryland, USA). A maximum error of about 20 % (except calcium) was obtained for RSFs determination. Inductively coupled plasma mass spectrometry (ICP-MS) was carried out to validate the RSFs. Sample weight of 25 – 35 mg was used for ICP-MS analysis. The ICP-MS result suggested that the calcium value is 3-fold less than what is reported for silicon 57b powder in NIST certificate. When the reference value of calcium determined by ICP-MS is used the uncertainty value drop from ~80 % to ~10%. The reproducibility of RSFs was determined in a period of about nine months and was comparable for all elements, except phosphorous, niobium and tungsten. The differences in argon flow rates when measured second time, as well as variation in diffusion of heavy elements (Nb, W) could potentially be the reason for such variation in RSFs.

The measurement of indium to silicon ratio suggested that the sputtering rate of indium increases linearly with the discharge condition. This indicates that covering of indium sheet as much as possible with silicon powder would help to suppress the indium signal. However, it should be noted that the increase of amount of powder can lead to problems in the plasma sustenance due to powder sliding in between ceramics and tantalum front plate.

### 5.3 Paper III: Tantalum flat sample sputtering and roughness

Paper I dealt with designing experimental setup for optimization of glow discharge condition. In Paper II, this knowledge was used for finding optimum glow discharge condition for RSFs determination for silicon powder. Hence, the first two papers contributed to bulk analysis application of Astrum GDMS. Paper III presents the groundwork required prior to performing depth profile analysis, which is another application of GDMS besides bulk analysis.

The prerequisite for depth profiling is to obtain flat craters with low roughness. While the approach for obtaining flat craters using other types of dc-GDMS, such as Element GD or VG9000, is readily available, there was no published literature for optimization of crater shapes using Astrum GDMS. Hence, this work provides as many as 5 discharge conditions leading to generation of flat craters in tantalum samples: (i) 2 mA, 0.6 kV; (ii) 2.3 mA, 0.7 kV; (iii) 3 mA, 0.8 kV; (iv) 4 mA, 0.9 kV and (v) 5 mA, 1 kV. Further, voltage to current ratio in the range of 0.2 - 0.35 kV/mA is found to result into flat craters in tantalum. Hence, this work provides a good method for obtaining flat craters also for other matrices.

Another important finding of Paper III is the explanation for the common roughness observed by GDMS users after sputtering. For this, two types of tantalum material were selected. One with several small grains of micrometer size while another with few large grains of millimeter size. The sputtered control sample with many grains lead to roughness generation. When the number of grains were reduced, the roughness also reduced. There is a clear observation of differential sputtering of grains with different crystal orientation. This was confirmed by combination of crater profile obtained from mechanical profilometer as well as electron backscattered diffraction and scanning electron microscopy images. Therefore, it is reasonable to state that differential sputtering of grains is likely to contribute to the roughness at the crater bottom.

## 5.4 Paper IV: Steel-Aluminum joint depth profiling

Paper IV builds-up on Paper III where a similar approach of altering glow discharge condition for crater shape optimization is utilized. This led to determination of glow discharge condition (5 mA, 0.75 kV) for optimum crater shape for a base aluminum material.

Paper IV presents the diffusion of trace alloying elements such as chromium and nickel at the steel-aluminum bi-layered material produced by cold rolling process. Post rolling heat-treatment of 400 °C for 30 minutes was applied to the rolled material. The result of the study indicates diffusion of both chromium and nickel at the interface for both materials, i.e., non-heated and heat-treated material. One plausible explanation to this observation is diffusion of impurity elements already during the rolling process. However, slightly high content of both trace elements was found at the interface for heat-treated specimen. This can be attributed to the post rolling heat treatment. The scanning electron microscopy images demonstrated intermetallic layer formation for heat-treated material. The depth profile result demonstrated surprisingly high content of chromium in the aluminum layer for both materials. This observation was further verified through results of complimentary techniques such as electron probe micro-analyzer (EPMA) and energy dispersive X-ray spectroscopy (EDS). Higher diffusion of chromium to aluminum layer forming chromium-iron precipitates is expected to prevent further migration of iron into aluminum.

This manuscript presents short heat treatment experimental design using trace amount of impurity elements. The findings of the work can be helpful for designing optimum manufacturing of steel-aluminum joints in relation to material composition and heat treatment post rolling. Further, this work shows that slow-flow/low-power dc-GDMS is suitable for depth profile analysis of this type of sample although this is not a common application of SF-GDMS due to the slow data acquisition. The total sample analysis time for non-heated and heat-treated sample was about ~16 h and ~8.5 h, respectively. Nonetheless, with production of slow-flow/low-power GDMS like VG9000 discontinued since 2005, the depth profiling application of currently commercially available instruments such as Astrum and Auto concept GD 90 is necessary. Such applications are largely unexplored until this point of time.

## 5.5 Other interesting data

For tantalum pin study, quantification for carbon, nitrogen, and argon (shown in Figure 5-1) were found to follow the same trend as for oxygen presented in paper I, i.e., decrease in concentration with increase in current at a fixed voltage. Hence, the trend of elements ionized predominantly by electron impact using Astrum is established. This result is also consistent with nitrogen content in aluminum pin sample (shown in Figure 5-2, left).

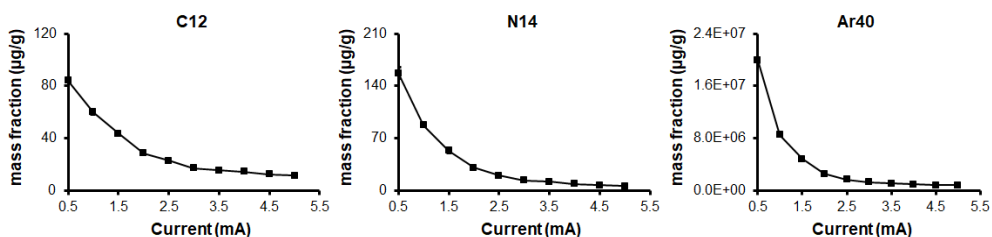


**Figure 5-1:** Quantification for carbon (left), nitrogen (middle), and argon (right) respectively, after analysis of tantalum pin sample at discharge condition of 0.5 – 5 mA at 1 kV.

One of the conclusions, after comparing the results from Paper I and II, is that the variation in concentration of elements is higher in pin geometry as compared to flat geometry. However, these results were for different matrices. Hence, pin and flat sample of the same matrix, i.e., aluminum, is analysed to study the influence of discharge parameters on the variation in quantification of nitrogen. The comparison is shown in Figure 5-2.

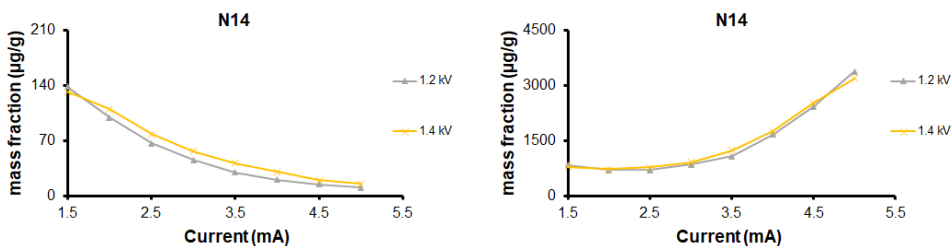


**Figure 5-2:** Mass fraction of nitrogen for pin (left) and flat (right) aluminum at discharge condition of 1 – 5 mA and 1.2 – 1.4 kV, respectively.

Interestingly, for a range of discharge current and voltage, the flat geometry demonstrated less variation in range of 1.5 – 3 mA for 1.2 – 1.4 kV, which is not the case for the pin geometry. This might be the explanation to why Astrum users observe more variation of relative sensitivity factors in pin geometry as compared to flat. Bogaerts and Gijbels<sup>126</sup> using VG9000 (similar to Astrum in terms of ion source and discharge parameters) has modelled argon ion to metastable argon ratio ( $Ar^+/Ar^*$ ) near the exit orifice from where ions are extracted.<sup>126</sup> The results suggest that the ratio is ten times higher in the flat geometry than for pin.<sup>126</sup> This indicates that the ratio of electron impact ionization to that of Penning ionization is higher in the flat geometry. More practical works in different matrices are needed to support this conclusion.

The current-voltage characteristics of Astrum using tantalum pin is presented in Figure 5-3. A non-linear behaviour is observed for low flow rates, while it becomes more linear at higher flow rates. This finding suggests that higher flow rates (>0.25 sccm) can give better reproducibility.

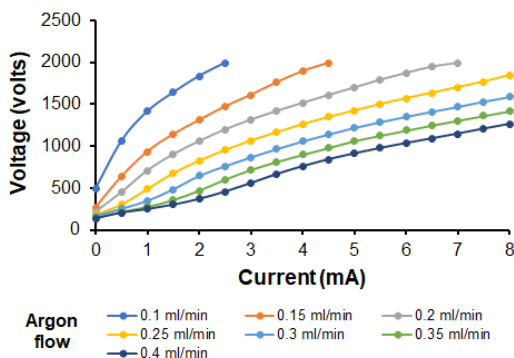


**Figure 5-3:** Current-voltage characteristics at different argon flow rate using tantalum pin for Astrum GDMS.

**CHAPTER 6**  
**Conclusions and Recommendations**

## 6.1 Conclusions

The following conclusions can be drawn from this PhD work.

1. The absolute intensity of matrix ion, impurity elements, and discharge gas increases with increase in current to a certain point, and then decrease for all voltage settings, i.e., follow more or less similar trend.
2. The change in absolute intensity of matrix and impurity elements, although follows the same trend, is unequal from one discharge setting to another, hence contributing to change in RSFs.
3. Measuring the absolute intensity and quantification of gaseous elements that are ionized only or predominantly by electron impact such as carbon, nitrogen, oxygen and argon can help to optimize the discharge parameters before determining RSFs.
4. Measurement of gaseous elements can help to determine ionization mechanism of some impurity elements.
5. It is likely that RSFs vary more in pin geometry as compared to flat geometry. However, more work is required to support this conclusion.
6. The sputtering rate can be changed by changing the discharge parameters and multiple combinations of discharge settings can lead to optimum crater shape.
7. The sputtering rate is consistent with Boumans' equation (2-16).
8. Sample roughness observed at crater bottom for polycrystalline materials is mainly due to differential sputtering of grains with different crystal orientation.
9. Preliminary studies of depth profiling indicate that Astrum GDMS can be used for diffusion studies for material science applications.



## 6.2 Limitations of the PhD work

The thesis work explored the capabilities of Astrum, which can analyse pin, flat and powder samples of different electrical conductivities. In Paper I only a few elements were selected for studying the effect of discharge parameters on concentration variation. This is the main limitation of the study. This limitation is tried to be compensated by studying more elements in Paper II. However, in Paper II only two powders were used to generate relative sensitivity factors. Based on literature, the calibration curve does not always pass-through origin, as there is involvement of the intercept. Therefore, various CRMs, RMs or synthetic standards with wide concentration range need to be analysed wherever possible to better estimate the RSFs and related uncertainty. The option of relying in on one or two standards should be minimized as much as possible. Although in Paper III it is clearly demonstrated that roughness arises as a result of differential sputtering, it was not possible to quantify the roughness as it is very challenging to perform electron backscattered diffraction (EBSD) on the entire GDMS crater. Further, continuous change of roughness during sputtering is another limitation to provide quantitative values of roughness measurement. Paper IV describes the GDMS capability on studying diffusion effect of a steel-aluminum joined sample using the cold rolling process. In order to reduce the thickness of the steel layer, the sample was polished which unfortunately could not be reproduced. Further, a long sputtering time of over 16 and 8 hours was required for the analysis of untreated and heat-treated samples, respectively. The main reason for this was the too thick steel layer on top of aluminum.

### 6.3 Recommendations and outlook

Two planned projects, i.e., determining RSFs for flat silicon samples and measuring the Astrum's limits of detection, could not be completed during the PhD work. Therefore, I would recommend performing the RSFs study using multiple sets of silicon samples. In addition, it would be worth comparing impurity concentration of boron and phosphorus in silicon ingots based on resistivity measurements to that measured by GDMS.

Further, the volume of discharge gas inside the glow discharge chamber depends on how tightly the sample holder probe is placed against the glow discharge cell. The placement of sample holder into the GDMS chamber is a manual process. This can lead to variation in argon flow during sample exchange. Hence to study the reproducibility of concentration for a long term, it would be worth also to regularly measure the argon flow values for the corresponding current and voltage setting. Moreover, there is limited information available about round robin analysis using the Astrum instruments, which would be interesting and important to carry out.

Based on a very limited study of depth profiling, it is clear that the glow discharge parameters have a good temporal stability and Astrum offers excellent signal stability. To further improve on depth profiling capabilities, layered or coated sample of thickness in the order of few microns on top of a substrate could be a good starting point for a continuation of the work performed in this thesis. Further, crater shape optimization should be done on actual sample rather than base material to generate the best possible crater shape. This is possibly the reason behind a non-ideal crater for the steel-aluminum joints investigated here.

**CHAPTER 7**  
**References**

## References

- [1] Rapp, D., and Englander-Golden, P. (1965) Total Cross Sections for Ionization and Attachment in Gases by Electron Impact. I. Positive Ionization, *The Journal of Chemical Physics* 43, 1464-1479.
- [2] Schram, B. L., De Heer, F. J., van der Wiel, M. J., and Kistemaker, J. (1965) Ionization cross sections for electrons (0.6–20 keV) in noble and diatomic gases, *Physica* 31, 94-112.
- [3] Smith, P. T. (1930) The Ionization of Helium, Neon, and Argon by Electron Impact, *Physical Review* 36, 1293-1302.
- [4] Paschen, F. (1889) Ueber die zum Funkenübergang in Luft, Wasserstoff und Kohlensäure bei verschiedenen Drucken erforderliche Potentialdifferenz, *Annalen der Physik* 273, 69-96.
- [5] Mahan, J. E. (2000) *Physical vapor deposition of thin films*, Wiley-Interscience, New York.
- [6] Hagstrum, H. D. (1956) Effect of Monolayer Adsorption on the Ejection of Electrons from Metals by Ions, *Physical Review* 104, 1516-1527.
- [7] Hagstrum, H. D. (1956) Auger Ejection of Electrons from Tungsten by Noble Gas Ions, *Physical Review* 104, 317-318.
- [8] Hagstrum, H. D. (1956) Auger Ejection of Electrons from Molybdenum by Noble Gas Ions, *Physical Review* 104, 672-683.
- [9] Marcus, R. K., and Broekaert A. C., J. (2003) *Glow Discharge Plasmas in Analytical Spectroscopy* John Wiley & Sons Ltd.
- [10] Schubert, G., Basner, R., Kersten, H., and Fehske, H. (2011) Determination of sheath parameters by test particles upon local electrode bias and plasma switching, *The European Physical Journal D* 63, 431-440.
- [11] Marcus, R. K. (1991) *Glow Discharge Spectroscopies*, Springer Science.
- [12] Murphy, E. L., and Good, R. H. (1956) Thermionic Emission, Field Emission, and the Transition Region, *Physical Review* 102, 1464-1473.
- [13] Fowler, R. H., Nordheim, L. (1928) Electron emission in intense electric fields, *Proc. R. Soc. Lond. A* 119, 173–181.
- [14] Trucchi, D. M., and Melosh, N. A. (2017) Electron-emission materials: Advances, applications, and models, *MRS Bulletin* 42, 488-492.
- [15] Chapman, B. N. (1980) *Glow discharge processes : sputtering and plasma etching* Wiley, New York.
- [16] Bogaerts, A., and Gijbels, R. (1998) Fundamental aspects and applications of glow discharge spectrometric techniques, *Spectrochimica Acta Part B: Atomic Spectroscopy* 53, 1-42.
- [17] Andrade, F. J., Wetzels, W. C., Chan, G. C. Y., Webb, M. R., Gamez, G., Ray, S. J., and Hieftje, G. M. (2006) A new, versatile, direct-current helium atmospheric-pressure glow discharge, *Journal of Analytical Atomic Spectrometry* 21, 1175-1184.
- [18] Weiss, Z., Steers, E. B. M., Pickering, J. C., and Mushtaq, S. (2014) Excitation and transition rate diagrams of singly ionized iron in analytical glow discharges in argon, neon and an argon–hydrogen mixture, *Journal of Analytical Atomic Spectrometry* 29, 2078-2090.
- [19] Wagatsuma, K., and Hirokawa, K. (1988) Effects of helium addition to an argon glow discharge plasma on emission lines of sputtered particles, *Analytical Chemistry* 60, 702-705.
- [20] Lange, B., Matschat, R., and Kipphardt, H. (2007) Enhancement of intensities in glow discharge mass spectrometry by using mixtures of argon and helium as plasma gases, *Analytical and Bioanalytical Chemistry* 389, 2287-2296.
- [21] Mushtaq, S., Steers, E. B. M., Pickering, J. C., and Putyera, K. (2014) Selective and non-selective excitation/ionization processes in analytical glow discharges: excitation of the ionic spectra in argon/helium mixed plasmas, *Journal of Analytical Atomic Spectrometry* 29, 681-695.
- [22] Smithwick, R. W., Lynch, D. W., and Franklin, J. C. (1993) Relative ion yields measured with a high-resolution glow discharge mass spectrometer operated with an argon/hydrogen mixture, *Journal of the American Society for Mass Spectrometry* 4, 278-285.
- [23] Mushtaq, S., Steers, E. B. M., Pickering, J. C., and Weinstein, V. (2012) Asymmetric charge transfer involving the ions of added gases (oxygen or hydrogen) in Grimm-type glow discharges in argon or neon, *Journal of Analytical Atomic Spectrometry* 27, 1264-1273.

- [24] Mushtaq, S., Steers, E. B. M., Pickering, J. C., and Weinstein, V. (2014) Effect of small quantities of oxygen in a neon glow discharge, *Journal of Analytical Atomic Spectrometry* 29, 2027-2041.
- [25] Flores, O., Castillo, F., Martinez, H., Villa, M., Villalobos, S., and Reyes, P. G. (2014) Characterization of direct current He-N<sub>2</sub> mixture plasma using optical emission spectroscopy and mass spectrometry, *Physics of Plasmas* 21, 053502.
- [26] Mushtaq, S., Steers, E. B. M., Pickering, J. C., and Šmid, P. (2014) Enhancement of analyte atomic lines with excitation energies of about 5 eV in the presence of molecular gases in analytical glow discharges, *Journal of Analytical Atomic Spectrometry* 29, 2022-2026.
- [27] Mushtaq, S., Steers, E. B. M., Hoffmann, V., Weiss, Z., and Pickering, J. C. (2016) Evidence for charge transfer from hydrogen molecular ions to copper atoms in a neon–hydrogen analytical glow discharge, *Journal of Analytical Atomic Spectrometry* 31, 2175-2181.
- [28] Bogaerts, A., and Gijbels, R. (1996) Relative sensitivity factors in glow discharge mass spectrometry: The role of charge transfer ionization, *Journal of Analytical Atomic Spectrometry* 11, 841-847.
- [29] Steers, E. B. M., and Fielding, R. J. (1987) Charge-transfer excitation processes in the Grimm lamp, *Journal of Analytical Atomic Spectrometry* 2, 239-244.
- [30] Steers, E. B. M., and Thorne, A. P. (1993) Application of high-resolution Fourier transform spectrometry to the study of glow discharge sources. Part 1. Excitation of iron and chromium spectra in a microwave boosted glow discharge source, *Journal of Analytical Atomic Spectrometry* 8, 309-315.
- [31] Danzmann, K., and Kock, M. (1981) Population densities in a titanium hollow cathode, *Journal of Physics B: Atomic and Molecular Physics* 14, 2989-2993.
- [32] Mushtaq, S., Steers, E. B. M., Barnhart, D., Churchill, G., Kasik, M., Richter, S., Pfeifer, J., and Putyera, K. (2017) The production of doubly charged sample ions by “charge transfer and ionization” (CTI) in analytical GD-MS, *Journal of Analytical Atomic Spectrometry* 32, 1721-1729.
- [33] Pack, R. T., Walker, R. B., and Kendrick, B. K. (1998) Three-body collision contributions to recombination and collision-induced dissociation. I. Cross sections, *The Journal of Chemical Physics* 109, 6701-6713.
- [34] Boumans, P. W. J. M. (1972) Sputtering in a glow discharge for spectrochemical analysis, *Analytical Chemistry* 44, 1219-1228.
- [35] Storey, A. P., Ray, S. J., Hoffmann, V., Voronov, M., Engelhard, C., Buscher, W., and Hieftje, G. M. (2016) Emergence and consequences of lateral sample heterogeneity in glow discharge spectrometry, *Spectrochimica Acta Part B: Atomic Spectroscopy* 126, 37-43.
- [36] Hagelaar, G. J. M., and Pitchford, L. C. (2002) Estimated mass loss due to evaporation for zinc cathodes in analytical glow discharges, *Journal of Analytical Atomic Spectrometry* 17, 1408-1410.
- [37] Weiss, Z., and Šmid, P. (2000) Zinc-based reference materials for glow discharge optical emission spectrometry: sputter factors and emission yields, *Journal of Analytical Atomic Spectrometry* 15, 1485-1492.
- [38] Kudermann, G., and Blaufuß, K.-H. (1987) Characterization of high purity gallium, *Microchimica Acta* 91, 269-274.
- [39] Venzago, C., and Pisonero, J. (2015) CHAPTER 13 Glow Discharge Mass Spectrometry, In *Sector Field Mass Spectrometry for Elemental and Isotopic Analysis*, pp 319-380, The Royal Society of Chemistry.
- [40] Modanese, C., Gaspar, G., Arnberg, L., and Di Sabatino, M. (2014) On copper diffusion in silicon measured by glow discharge mass spectrometry, *Analytical and Bioanalytical Chemistry* 406, 7455-7462.
- [41] Payling, R. (1994) Boumans' equation revisited. Part I: Characteristics of the glow discharge lamp, *Surface and Interface Analysis* 21, 785-790.

- [42] Hoffmann, V., Efimova, V. V., Voronov, M. V., Šmíd, P., Steers, E. B. M., and Eckert, J. (2008) Measurement of voltage and current in continuous and pulsed rf and dc glow discharges, *Journal of Physics: Conference Series* 133, 012017.
- [43] Efimova, V. (2011) Study in analytical glow discharge spectrometry and its application in materials science, In *Fakultät für Maschinenwesen, Institut für Werkstoffwissenschaft TECHNISCHE UNIVERSITÄT DRESDEN*.
- [44] Bogaerts, A., Gijbels, R., and Serikov, V. V. (2000) Calculation of gas heating in direct current argon glow discharges, *J Appl Phys* 87, 8334-8344.
- [45] Kasik, M., Michellon, C., and Pitchford, L. C. (2002) Effects of cathode heating in a GDMS system, *Journal of Analytical Atomic Spectrometry* 17, 1398-1399.
- [46] Ferreira, N. P., and Büger, P. A. (1978) Redeposition of Sputtered Material in a Glow-Discharge Lamp Measured by Means of an Ion Microprobe Mass Analyser, In *Zeitschrift für Naturforschung A*, p 141, National Physical Research Laboratory, Pretoria, South Africa.
- [47] Raith, A., Hutton, R. C., and Huneke, J. C. (1993) Optimization of quantitative depth profiling with glow discharge mass spectrometry. Part 1. Optimization studies on crater shape and time–depth conversion, *Journal of Analytical Atomic Spectrometry* 8, 867-873.
- [48] Bogaerts, A., Verscharen, W., and Steers, E. (2004) Computer simulations of crater profiles in glow discharge optical emission spectrometry: comparison with experiments and investigation of the underlying mechanisms, *Spectrochimica Acta Part B: Atomic Spectroscopy* 59, 1403-1411.
- [49] Pisonero, J., Feldmann, I., Bordel, N., Sanz-Medel, A., and Jakubowski, N. (2005) Depth profiling with modified dc-Grimm and rf-Grimm-type glow discharges operated with high gas flow rates and coupled to a high-resolution mass spectrometer, *Analytical and Bioanalytical Chemistry* 382, 1965-1974.
- [50] Bogaerts, A., and Gijbels, R. (1997) Calculation of crater profiles on a flat cathode in a direct current glow discharge, *Spectrochimica Acta Part B: Atomic Spectroscopy* 52, 765-777.
- [51] Venzago, C., Ohanessian-pierrard, L., Kasik, M., Collisi, U., and Baude, S. (1998) Round robin analysis of aluminium using glow discharge mass spectrometry, *Journal of Analytical Atomic Spectrometry* 13, 189-193.
- [52] Gonzalez-Gago, C., Bordel, N., and Pisonero, J. (2019) Glow Discharge Mass Spectrometry, In *Materials Characterization*, p 0, ASM International.
- [53] Winchester, M. R., and Payling, R. (2004) Radio-frequency glow discharge spectrometry:: A critical review, *Spectrochimica Acta Part B: Atomic Spectroscopy* 59, 607-666.
- [54] Kenneth Marcus, R. (2000) Direct polymer analysis by radio frequency glow discharge spectrometry. Invited Lecture, *Journal of Analytical Atomic Spectrometry* 15, 1271-1277.
- [55] Gibeau, T. E., Hartenstein, M. L., and Marcus, R. K. (1997) Cryogenically cooled sample holder for polymer sample analysis by radiofrequency glow discharge mass spectrometry, *Journal of the American Society for Mass Spectrometry* 8, 1214-1219.
- [56] Lobo, L., Tuccitto, N., Bordel, N., Pereiro, R., Pisonero, J., Licciardello, A., Tempez, A., Chapon, P., and Sanz-Medel, A. (2010) Polymer screening by radiofrequency glow discharge time-of-flight mass spectrometry, *Analytical and Bioanalytical Chemistry* 396, 2863-2869.
- [57] Klinger, J. A., Savickas, P. J., and Harrison, W. W. (1990) The pulsed glow discharge as an elemental ion source, *Journal of the American Society for Mass Spectrometry* 1, 138-143.
- [58] Muñiz, A. C., Pisonero, J., Lobo, L., Gonzalez, C., Bordel, N., Pereiro, R., Tempez, A., Chapon, P., Tuccitto, N., Licciardello, A., and Sanz-Medel, A. (2008) Pulsed radiofrequency glow discharge time of flight mass spectrometer for the direct analysis of bulk and thin coated glasses, *Journal of Analytical Atomic Spectrometry* 23, 1239-1246.
- [59] Harrison, W. W., and Hang, W. (1996) Powering the analytical glow discharge, *Fresenius' Journal of Analytical Chemistry* 355, 803-807.
- [60] Lewis, C. L., Oxley, E. S., Pan, C. K., Steiner, R. E., and King, F. L. (1999) Determination of  $^{40}\text{Ca}^+$  in the Presence of  $^{40}\text{Ar}^+$ : An Illustration of the Utility of Time-Gated Detection in Pulsed Glow Discharge Mass Spectrometry, *Analytical Chemistry* 71, 230-234.

- [61] Li, L., Millay, J. T., Turner, J. P., and King, F. L. (2004) Millisecond pulsed radio frequency glow discharge time of flight mass spectrometry: temporal and spatial variations in molecular energetics, *J Am Soc Mass Spectrom* 15, 87-102.
- [62] Oxley, E., Yang, C., Liu, J., and Harrison, W. W. (2003) Ion Transport Diagnostics in a Microsecond Pulsed Grimm-Type Glow Discharge Time-of-Flight Mass Spectrometer, *Analytical Chemistry* 75, 6478-6484.
- [63] Demény, D., Szücs, L., and Adamik, M. (1992) Influence of anode geometry on electric field distribution and crater profile using a glow discharge lamp, *Journal of Analytical Atomic Spectrometry* 7, 707-710.
- [64] Kasik, M., Venzago, C., and Dorka, R. (2003) Quantification in trace and ultratrace analyses using glow discharge techniques: round robin test on pure copper materials, *Journal of Analytical Atomic Spectrometry* 18, 603-611.
- [65] Quarles, C. D., Castro, J., and Marcus, R. K. (2017) Glow Discharge Mass Spectrometry, In *Encyclopedia of Spectroscopy and Spectrometry (Third Edition)* (Lindon, J. C., Tranter, G. E., and Koppenaal, D. W., Eds.), pp 30-36, Academic Press, Oxford.
- [66] Bogaerts, A. (1999) Glow Discharge Mass Spectrometry, Methods, In *Encyclopedia of Spectroscopy and Spectrometry* (Lindon, J. C., Ed.), pp 669-676, Elsevier, Oxford.
- [67] Grimm, W. (1968) Eine neue glimmentladungslampe für die optische emissions-spektralanalyse, *Spectrochimica Acta Part B: Atomic Spectroscopy* 23, 443-454.
- [68] Bengtson, A., and Danielsson, L. (1985) Depth profiling of thin films using a Grimm-type glow discharge lamp, *Thin Solid Films* 124, 231-236.
- [69] Banks, P. R., and Blades, M. W. (1991) Power, flow rate, and pressure effects in a jet-assisted glow discharge source, *Spectrochimica Acta Part B: Atomic Spectroscopy* 46, 501-515.
- [70] Kruger, R. A., Bombelka, R. M., and Laqua, K. (1980) Application of the Grimm magnetic field glow-discharge source to the analysis of mild and alloyed steel, *Spectrochimica Acta Part B: Atomic Spectroscopy* 35, 589-599.
- [71] Ko, J. B. (1984) New designs of glow discharge lamps for the analysis of metals by atomic emission spectroscopy, *Spectrochimica Acta Part B: Atomic Spectroscopy* 39, 1405-1423.
- [72] Gubal, A., Ganeev, A., Hoffmann, V., Voronov, M., Brackmann, V., and Oswald, S. (2017) Combined hollow cathode vs. Grimm cell: semiconductive and nonconductive samples, *Journal of Analytical Atomic Spectrometry* 32, 354-366.
- [73] Ganeev, A. A., Drobyshev, A. I., Gubal, A. R., Solovyev, N. D., Chuchina, V. A., Ivanenko, N. B., Kononov, A. S., Titova, A. D., and Gorbunov, I. S. (2019) Hollow Cathode and New Related Analytical Methods, *Journal of Analytical Chemistry* 74, 975-981.
- [74] Ganeev, A. A., Kuz'menkov, M. A., Lyubimtsev, V. A., Potapov, S. V., Drobyshev, A. I., Potemin, S. S., and Voronov, M. V. (2007) Pulsed discharge in a hollow cathode with the detection of ions in a time-of-flight mass spectrometer: Analytical capabilities in the analysis of solid samples, *Journal of Analytical Chemistry* 62, 444-453.
- [75] Ganeev, A. A., Gubal', A. R., Mosichev, V. I., Pershin, N. V., Petrov, S. N., Potapov, S. V., and Uskov, K. N. (2011) Lumas-30 time-of-flight mass spectrometer with pulsed glow discharge for direct determination of nitrogen in steel, *Journal of Analytical Chemistry* 66, 1411-1416.
- [76] Gusarova, T., Hofmann, T., Kipphardt, H., Venzago, C., Matschat, R., and Panne, U. (2010) Comparison of different calibration strategies for the analysis of zinc and other pure metals by using the GD-MS instruments VG 9000 and Element GD, *Journal of Analytical Atomic Spectrometry* 25, 314-321.
- [77] Vieth, W., and Huneke, J. C. (1991) Relative sensitivity factors in glow discharge mass spectrometry, *Spectrochimica Acta Part B: Atomic Spectroscopy* 46, 137-153.
- [78] Di Sabatino, M., Dons, A. L., Hinrichs, J., and Arnberg, L. (2011) Determination of relative sensitivity factors for trace element analysis of solar cell silicon by fast-flow glow discharge mass spectrometry, *Spectrochimica Acta Part B: Atomic Spectroscopy* 66, 144-148.

- [79] Matschat, R., Hinrichs, J., and Kipphardt, H. (2006) Application of glow discharge mass spectrometry to multielement ultra-trace determination in ultrahigh-purity copper and iron: a calibration approach achieving quantification and traceability, *Journal of Analytical Atomic Spectrometry* 386, 125-141.
- [80] Rudtsch, S., Fahr, M., Fischer, J., Gusarova, T., Kipphardt, H., and Matschat, R. (2008) High-Purity Fixed Points of the ITS-90 with Traceable Analysis of Impurity Contents, *International Journal of Thermophysics* 29, 139-150.
- [81] Kipphardt, H., Matschat, R., Vogl, J., Gusarova, T., Czerwensky, M., Heinrich, H.-J., Hioki, A., Konopelko, L. A., Methven, B., Miura, T., Petersen, O., Riebe, G., Sturgeon, R., Turk, G. C., and Yu, L. L. (2010) Purity determination as needed for the realisation of primary standards for elemental determination: status of international comparability, *Accreditation and Quality Assurance* 15, 29-37.
- [82] M. Wayne, D. (1997) Direct Determination of Trace Noble Metals (Palladium, Platinum and Rhodium) in Automobile Catalysts by Glow Discharge Mass Spectrometry, *Journal of Analytical Atomic Spectrometry* 12, 1195-1202.
- [83] van Straaten, M., Swenters, K., Gijbels, R., Verlinden, J., and Adriaenssens, E. (1994) Analysis of platinum powder by glow discharge mass spectrometry, *Journal of Analytical Atomic Spectrometry* 9, 1389-1397.
- [84] Yamada, K., and Uemoto, M. (2018) Evaluation of Relative Sensitivity Factors for Elemental Analysis of Aluminum and Magnesium Using Glow Discharge Mass Spectrometry with a Fast-Flow Grimm-type Ion Source, *Anal Sci* 34, 743-746.
- [85] Gusarova, T., Methven, B., Kipphardt, H., Sturgeon, R., Matschat, R., and Panne, U. (2011) Calibration of double focusing Glow Discharge Mass Spectrometry instruments with pin-shaped synthetic standards, *J Spectrochimica Acta Part B: Atomic Spectroscopy* 66, 847-854.
- [86] Zhang, J., Zhou, T., Cui, Y., Tang, Y., and Wu, B. (2020) Determination of relative sensitivity factors of elements in a copper matrix by using microsecond-pulsed and continuous direct current glow discharge mass spectrometry, *Journal of Analytical Atomic Spectrometry* 35, 2712-2722.
- [87] Zhang, J., Zhou, T., Tang, Y., Cui, Y., and Li, J. (2016) Determination of relative sensitivity factors of elements in high purity copper by doping-melting and doping-pressed methods using glow discharge mass spectrometry, *Journal of Analytical Atomic Spectrometry* 31, 2182-2191.
- [88] Gonzalez-Gago, C., Šmid, P., Hofmann, T., Venzago, C., Hoffmann, V., Gruner, W., Pfeifer, J., Richter, S., and Kipphardt, H. (2019) Investigations of matrix independent calibration approaches in fast flow glow discharge mass spectrometry, *Journal of Analytical Atomic Spectrometry* 34, 1109-1125.
- [89] McClenathan, D. M., and Hieftje, G. M. (2005) Absolute methods of quantitation in glow discharge mass spectrometry with a time-of-flight mass analyzer, *Journal of Analytical Atomic Spectrometry* 20, 1326-1331.
- [90] Wei, X., Qin, Z., Xiong, P., Wang, L., Zhang, H., Deng, D., and Liao, J. (2019) The direct quantification by glow discharge mass spectrometry with the universal relative sensitivity factors without matrix-matched standards, *Spectrochimica Acta Part B: Atomic Spectroscopy* 154, 43-49.
- [91] Pisonero, J., Fernández, B., and Günther, D. (2009) Critical revision of GD-MS, LA-ICP-MS and SIMS as inorganic mass spectrometric techniques for direct solid analysis, *Journal of Analytical Atomic Spectrometry* 24, 1145-1160.
- [92] Lange, B., Recknagel, S., Czerwensky, M., Matschat, R., Michaelis, M., Peplinski, B., and Panne, U. (2008) Analysis of pure copper – a comparison of analytical methods, *Microchimica Acta* 160, 97-107.
- [93] Coletti, G. (2013) Sensitivity of state-of-the-art and high efficiency crystalline silicon solar cells to metal impurities, *Progress in Photovoltaics: Research and Applications* 21, 1163-1170.
- [94] Hystad, M., Modanese, C., Di Sabatino, M., and Arnberg, L. (2012) Distribution and impact of chromium in compensated solar grade silicon, *Solar Energy Materials and Solar Cells* 103, 140-146.



- [95] Modanese, C., Di Sabatino, M., Sjøiland, A.-K., Peter, K., and Arnberg, L. (2011) Investigation of bulk and solar cell properties of ingots cast from compensated solar grade silicon, *Progress in Photovoltaics: Research and Applications* 19, 45-53.
- [96] Di Sabatino, M. (2014) Detection limits for glow discharge mass spectrometry (GDMS) analyses of impurities in solar cell silicon, *Measurement* 50, 135-140.
- [97] Zhang, J., Zhou, T., Tang, Y., Cui, Y., and Song, D. (2018) Rapid and quantitative analysis of impurities in silicon powders by glow discharge mass spectrometry, *Analytical and Bioanalytical Chemistry* 410, 7195-7201.
- [98] Duckworth, D. C., Barshick, C. M., and Smith, D. H. (1993) Analysis of soils by glow discharge mass spectrometry, *Journal of Analytical Atomic Spectrometry* 8, 875-879.
- [99] Woo, J. C., Jakubowski, N., and Stuewer, D. (1993) Analysis of aluminium oxide powder by glow discharge mass spectrometry with low mass resolution, *Journal of Analytical Atomic Spectrometry* 8, 881-889.
- [100] Tong, S. L., and Harrison, W. W. (1993) Glow discharge mass spectrometric analysis of non-conducting materials, *Spectrochimica Acta Part B: Atomic Spectroscopy* 48, 1237-1245.
- [101] Inoue, M., and Saka, T. (1999) Elemental analysis of powders by glow discharge mass spectrometry, *Analytica Chimica Acta* 395, 165-171.
- [102] Schelles, W., Maes, K. J. R., De Gendt, S., and Van Grieken, R. E. (1996) Glow Discharge Mass Spectrometric Analysis of Atmospheric Particulate Matter, *Analytical Chemistry* 68, 1136-1142.
- [103] Dong, J., Qian, R., Zhuo, S., Yu, P., Chen, Q., and Li, Z. (2019) Development and application of a porous cage carrier method for detecting trace elements in soils by direct current glow discharge mass spectrometry, *Journal of Analytical Atomic Spectrometry* 34, 2244-2251.
- [104] Milton, D. M. P., and Hutton, R. C. (1993) Investigations into the suitability of using a secondary cathode to analyse glass using glow discharge mass spectrometry, *Spectrochimica Acta Part B: Atomic Spectroscopy* 48, 39-52.
- [105] Aldave de las Heras, L., Hrneckec, E., Bildstein, O., and Betti, M. (2002) Neptunium determination by dc glow discharge mass spectrometry (dc-GDMS) in Irish Sea sediment samples, *Journal of Analytical Atomic Spectrometry* 17, 1011-1014.
- [106] Betti, M. (1996) Use of a direct current glow discharge mass spectrometer for the chemical characterization of samples of nuclear concern, *Journal of Analytical Atomic Spectrometry* 11, 855-860.
- [107] Qian, R., Zhuo, S., Wang, Z., and Robinson, P. K. (2013) Direct current glow discharge mass spectrometric analysis of non-conducting materials using a surface coating method, *Journal of Analytical Atomic Spectrometry* 28, 1061-1067.
- [108] Moreno, D., and Eliezer, D. (1994) Sputtering and roughness of the (0 01), (01 1) and (111) copper single-crystal planes, *Journal of Materials Science Letters* 13, 1591-1593.
- [109] Pisonero, J., Fernández, B., Pereiro, R., Bordel, N., and Sanz-Medel, A. (2006) Glow-discharge spectrometry for direct analysis of thin and ultra-thin solid films, *TrAC Trends in Analytical Chemistry* 25, 11-18.
- [110] Pisonero, J., Valledor, R., Licciardello, A., Quirós, C., Martín, J. I., Sanz-Medel, A., and Bordel, N. (2012) Pulsed rf-GD-TOFMS for depth profile analysis of ultrathin layers using the analyte prepeak region, *Analytical and Bioanalytical Chemistry* 403, 2437-2448.
- [111] Gubal, A., Chuchina, V., Lyalkin, Y., Mikhailovskii, V., Yakobson, V., Solovyev, N., and Ganeev, A. (2020) Depth profiling by pulsed glow discharge time-of-flight mass spectrometry with a combined hollow cathode cell, *Journal of Analytical Atomic Spectrometry* 35, 1587-1596.
- [112] Konarski, P., Kaczorek, K., Kaliński, D., Chmielewski, M., Pietrzak, K., and Barlak, M. (2013) Ion implanted inconel alloy – SIMS and GDMS depth profile analysis, *Surface and Interface Analysis* 45, 494-497.
- [113] Konarski, P., Kaczorek, K., Ćwil, M., and Marks, J. (2008) SIMS and GDMS depth profile analysis of hard coatings, *Vacuum* 82, 1133-1136.

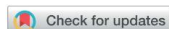
- [114] Di Sabatino, M., Modanese, C., and Arnberg, L. (2014) Depth profile analysis of solar cell silicon by GD-MS, *Journal of Analytical Atomic Spectrometry* 29, 2072-2077.
- [115] Su, K., Wang, X., and Putyera, K. (2010) Depth Resolved Trace Element Analysis of Ni-base Superalloys using Fast Flow- Glow Discharge Mass Spectrometry (FF-GDMS), *Yejin Fenxi/Metallurgical Analysis Vol 30 Suppl.1*, 165.
- [116] He, L. M., Meyer, J. D., Lee, W. Y., Putyera, K., and Walker, L. R. (2002) Depth profiling of Hf-doped aluminide coating by glow-discharge mass spectrometry, *Metallurgical and Materials Transactions A* 33, 3578-3582.
- [117] Spitsberg, I. T., and Putyera, K. (2001) Depth profile and quantitative trace element analysis of diffusion aluminided type layers on Ni-base superalloys using high-resolution glow-discharge mass spectrometry, *Surface and Coatings Technology* 139, 35-43.
- [118] Batanova, V. G., Sobolev, A. V., and Magnin, V. (2018) Trace element analysis by EPMA in geosciences: detection limit, precision and accuracy, *IOP Conference Series: Materials Science and Engineering* 304, 012001.
- [119] Sykes, D. (2017) Surface Chemical Analysis, In *Springer Handbook of Electronic and Photonic Materials* (Kasap, S., and Capper, P., Eds.), pp 1-1, Springer International Publishing, Cham.
- [120] Agüi-Gonzalez, P., Jähne, S., and Phan, N. T. N. (2019) SIMS imaging in neurobiology and cell biology, *Journal of Analytical Atomic Spectrometry* 34, 1355-1368.
- [121] Grovenor, C. R. M., Smart, K. E., Kilburn, M. R., Shore, B., Dilworth, J. R., Martin, B., Hawes, C., and Rickaby, R. E. M. (2006) Specimen preparation for NanoSIMS analysis of biological materials, *Applied Surface Science* 252, 6917-6924.
- [122] Martinez, M., and Baudalet, M. (2020) Calibration strategies for elemental analysis of biological samples by LA-ICP-MS and LIBS – A review, *Analytical and Bioanalytical Chemistry* 412, 27-36.
- [123] Yoon, S., and Lee, T. G. (2018) Biological tissue sample preparation for time-of-flight secondary ion mass spectrometry (ToF-SIMS) imaging, *Nano Convergence* 5, 24.
- [124] Instruments, N. Astrum System Manual Iss1.1.1, Nu Instruments Ltd.
- [125] Mushtaq, S., Steers, E. B. M., Churchill, G., Barnhart, D., Hoffmann, V., Pickering, J. C., and Putyera, K. (2016) Does asymmetric charge transfer play an important role as an ionization mode in low power-low pressure glow discharge mass spectrometry?, *Spectrochimica Acta Part B: Atomic Spectroscopy* 118, 56-61.
- [126] Bogaerts, A., and Gijbels, R. (1997) Modeling of Glow Discharge Sources with Flat and Pin Cathodes and Implications for Mass Spectrometric Analysis, *Journal of the American Society for Mass Spectrometry* 8, 1021-1029.

**CHAPTER 8**  
**Paper collection**

### **Paper I: Tantalum pin analysis**

**Paudel, G.**, Kasik, M., and Di Sabatino, M. (2019) Investigation of the intensity dependence of glow discharge mass spectrometry quantification on the discharge parameters, *Journal of Analytical Atomic Spectrometry* 34, 1829-1837.

Reproduced by permission of The Royal Society of Chemistry



Cite this: *J. Anal. At. Spectrom.*, 2019, 34, 1829

Received 31st March 2019  
Accepted 21st June 2019

DOI: 10.1039/c9ja00116f

rsc.li/jaas

## Investigation of the intensity dependence of glow discharge mass spectrometry quantification on the discharge parameters†

Gagan Paudel,<sup>a</sup> Martin Kasik<sup>b</sup> and Marisa Di Sabatino<sup>a</sup>

In direct current-glow discharge mass spectrometry (dc-GDMS), the current, voltage and argon pressure can be selected with two degrees of freedom to define the analytical conditions. The Astrum GD-MS allows control of the current or voltage up to 8 mA and 2000 V, respectively. It is crucial to study if and how variation in the operating parameters (current, voltage and Ar pressure) can effect the quantification of impurities. To study these effects, a tantalum pin (>99.9%) sample was analyzed from 0.5 mA to 5 mA at 1000 V and from 600 V to 1500 V at 3 mA. The results of the study indicate that the calculated concentrations of impurities vary differently as a function of changes in the operating parameters. Some elements are more sensitive to changes in the operating parameters than other elements. The variation in the quantification of impurities is associated with differences in the dependencies of the ion intensities of the trace and matrix elements under the discharge conditions. The difference in the relative sensitivity factors (RSFs) at different discharge settings can thus be attributed to these findings.

### A. Introduction

Glow discharge mass spectrometry (GDMS) is a solid sampling analytical technique; it requires minimal sample preparation for multi-elemental characterization of a wide range of solid specimens. GDMS is known to offer a wide linear dynamic range, low limits of detection,<sup>1</sup> and good internal and external reproducibility. Therefore, low-power/low-pressure GDMS are known for less variability from instrument to instrument.<sup>2</sup> Moreover, GDMS can be operated in different power supply modes and utilizes a variety of ion source designs.<sup>3</sup> This diversity allows freedom of choice for the analysis of samples (metals, semiconductors and insulators) with different electrical properties and forms (flat or pin-shaped samples, powders, etc.). Thus, GDMS is a useful technique for many applications, such as in high purity metals, aerospace super alloys, precious metals, dielectrics, depth-profiling of layers and coatings, semiconductors, polymers, and geological samples.<sup>4,5</sup>

Among the various commercially available GDMS instruments, radio-frequency-based, time of flight glow discharge mass spectrometers (rf-TOF-GDMS) are relatively fast; they are well-known for depth profiling, direct analysis of insulators and molecular mass spectrometry applications.<sup>6,7</sup> However, sector field GDMS instruments equipped with dc sources are the most

common commercial instruments, and they are preferred for the depth profiling of photovoltaics and many other applications because they offer better limits of detection.<sup>1</sup> In 2014, Di Sabatino *et al.* studied the diffusion profiles of common impurities in solar cell silicon.<sup>8</sup> Other merit points of dc-GDMS are their simple design and no need of complex power matching as in the case of rf-based instruments. The Astrum GD-MS (Nu Instruments) is one of the latest commercial developments, with a low pressure VG9000 (Thermo Scientific)-like ion source design coupled to a double focusing sector field mass analyser in the Nier-Johnson geometry. This instrument accommodates both flat and pin-shaped samples. A Faraday detector is used for the matrix as well as for major elements, whereas traces are detected by an electron multiplier. Unlike the Element GD (Thermo), the Astrum GD-MS offers the possibility of cryo-cooling to suppress interference from residual gases. It utilizes low-pressure discharge gas to maintain the glow discharge. In the GDMS community, the Astrum GD-MS is considered to be an immediate replacement for the VG9000 and is believed to provide similar analytical performance.

Standard relative sensitivity factors (stdRSFs) are normalized to iron<sup>9</sup> and allow semi-quantitative analysis, avoiding the use of calibration standards. Due to the possibility of achieving semi-quantitative analysis with good reproducibility, GDMS is becoming popular across industries and especially in contract laboratories, where wide varieties of samples are analyzed and turnaround time and throughput are regarded as crucial. The limited availability of calibrated solid matrix-matched standards has led to various attempts to develop synthetic matrix-matched standards.<sup>10</sup> However, it has been realized that this

<sup>a</sup>Department of Materials Science and Engineering, Norwegian University of Science and Technology, 7491 Trondheim, Norway. E-mail: gagan.paudel@ntnu.no

<sup>b</sup>MK2 Technologies Inc., Jamesville, NY 13078, USA

† Electronic supplementary information (ESI) available. See DOI: 10.1039/c9ja00116f

is not an easy task to perform routinely. In addition, preparing synthetic standards is feasible only for limited types of matrices for which suitable starting materials (usually fine, high purity powders that are easy to work with) are available. Hence, stdRSFs are an important starting point for GDMS quantification of any sample. Thus, studies that can elucidate and/or improve GDMS quantification are essential.

In the present work, we have investigated the effects of a range of discharge parameters to study if and how they alter the quantification of trace elements present in a tantalum pin sample. It is common among GDMS users to experience changes in relative sensitivity factors (RSFs) at different discharge parameters.<sup>5,11</sup> However, there is no adequate explanation for these changes. The current work attempts to explain one of the underlying causes and processes involved therein. The possible application of this work is discussed. Additionally, signal stability and quantification reproducibility are studied. The possible sources of discrepancy in reproducibility and practical considerations to minimize it are mentioned wherever applicable or thought necessary. However, this work is not intended to compare the analytical performance of the Astrum GD-MS with other GDMS instruments.

### Quantification in GDMS

Quantification in GDMS relies on calibration curves, similar to many other analytical techniques. However, experience among GDMS users/community and theoretical considerations show that GDMS exhibits linear calibration curves with certain uncertainty ranges. It should be noted that a concentration-dependent calibration curve has been reported.<sup>12</sup> However, due to the limited availability of certified samples at ultratrace levels, a linear calibration curve passing through the origin is assumed/expected. The RSF represents the slope of the calibration curve. The RSF takes into account sputtering process phenomena, a specific mix of ionization processes, transportation and differences in transmission and detection for each analyte.<sup>9</sup>

For high purity materials, the matrix element mass fraction is close to 100%. Thereby, the ion current of the matrix element is several orders of magnitude higher than the total ion current of the impurity elements. Thus, the ion current of the matrix element is a good approximation of the total ion current.<sup>1</sup> For GDMS quantification, the following eqn (1) can be used.

$$C_{X/M} = \frac{I_{X_i}}{I_{M_i}} \times \frac{A_{M_i}}{A_{X_i}} \times \text{RSF}_{X/M} \quad (1)$$

where  $C_{X/M}$  is the mass fraction of a trace element X present in a matrix M;  $I_{X_i}$  and  $I_{M_i}$  are the intensities of isotopes of the trace element X and matrix M, respectively; and  $A_{X_i}$  and  $A_{M_i}$  are natural isotopic abundances of isotopes of the trace element and of the matrix, respectively. The abundance-corrected ratio of the intensities is called the elemental ion beam ratio (IBR<sub>X/M</sub>). RSF<sub>X/M</sub> is the specific RSF of an element X in a matrix M. RSF<sub>X/M</sub> can be determined as the ratio mass fraction of  $C_{X/M}$  to IBR<sub>X/M</sub> (as indicated in the following eqn (2)) in matrix-matched

certified reference materials (CRM), reference materials (RM) and/or synthetic standards.

$$\text{RSF}_{X/M} = \frac{C_{X/M}}{\text{IBR}_{X/M}} \quad (2)$$

Because CRM, RM and/or synthetic standards are not readily available and/or challenging to prepare routinely, particularly for ultratrace levels, stdRSF is used instead. Iron is one of the most abundant elements in the Earth's crust and is typically certified to be present in most CRMs and RMs. Therefore, stdRSFs are normalized to iron. The following equation is used:

$$\text{stdRSF}_X = \frac{\text{RSF}_{X/M}}{\text{RSF}_{\text{Fe}/M}} = \frac{I_{\text{Fe}}}{I_X} \times \frac{C_{X/M}}{C_{\text{Fe}/M}} \quad (3)$$

where stdRSF<sub>X</sub> is the standard RSF of an element X and RSF<sub>X/M</sub> and RSF<sub>Fe/M</sub> are the RSFs of element X and Fe in the matrix M, respectively.  $I_{\text{Fe}}$  and  $I_X$  refer to the abundance corrected intensities of iron and the isotope of interest, respectively.  $C_{X/M}$  and  $C_{\text{Fe}/M}$  represent the mass fractions of a trace element X and iron present in matrix M, respectively. For various quantification models and approaches in GDMS, it is recommended to refer to.<sup>13</sup>

## B. Experimental

### Sample preparation

A pin-shaped tantalum sample (23 mm long and 3 mm in diameter) of 99.95% purity was provided by Nu Instruments. The specimen was etched with some modifications as described in ref. 14. Thereby, a solution with 1 : 1 : 2 hydrofluoric acid, nitric acid and distilled water was used as an etchant for 2 minutes. Thereafter, the pin was rinsed in distilled water followed by ethanol and finally dried using a hot gun before inserting into the Astrum GD-MS instrument (Nu Instruments, UK). The specimen was cryogenically cooled and pre-sputter cleaned at 3 mA, 1000 V for 30 minutes before starting the analysis. The instrument was tuned to obtain a Ta181 signal on the order of  $\sim 1.4 \times 10^{-9}$  and a resolution power of 4000 ( $M/\Delta M$ , 10% of peak height approach).

### Instrumentation

The Astrum glow discharge mass spectrometer (Nu Instruments, UK) was first commercialized in 2010. It is a double-focusing mass spectrometer with user-definable resolution power in the range of 300 to 10 000 ( $M/\Delta M$ , 10% of peak height approach).<sup>15</sup> The widths of the source and collector slits allow the operator to define the resolving power of the instrument. The sample loading and glow discharge chambers can be vented to atmospheric pressure for sample exchange and cell change, respectively, and/or for cleaning purposes. Two cell configurations are available, namely flat and pin, allowing the analysis of flat- and pin-shaped samples. Two sliding valves separate the sampling chamber, glow discharge chamber and transfer region of the instrument. The glow discharge chamber is evacuated by a turbomolecular pump which is backed by a rotary pump, while the

transfer region and analyser region are evacuated by a turbo-molecular pump and two ion pumps, respectively. The glow discharge can be initiated by defining the desired current, voltage and discharge gas flow using the instrument software and can be controlled through the instrument schematic. The Astrum GD-MS can be operated either in *constant current mode* or in *constant voltage mode*. In the magnet scan, the instrument can be tuned for ion beam transmission and peak shape and can be calibrated for specific masses, typically using tantalum. In the instrument method, the user can define parameters such as integration time, number of peak widths and steps, isotopes of interest, desired set of RSFs, and detector.

## Methods

To ensure that observed changes in quantification were solely due to the discharge parameters, a specific workflow was used. The workflow of the analysis is summarized in Fig. 1. First, the sample material was tested for homogeneity. The periodic table from Li to U was screened in discharge conditions (3 mA, 1000 V) to determine the best interference-free isotope for each element (this step is referred to as *the test analysis*). Subsequently, the selected isotopes were checked again for signal stability using the same conditions (this step is referred to as *the stability study 1*). With a resolution power of 4000, there was no issue of interference in the studied elements/isotopes. The next step (referred to as *the discharge study*) was the most important step, where the intensities of all isotopes selected in the previous steps (including argon) were monitored as a function of changing discharge conditions. The last step was the second signal stability test (referred to as *the stability study 2*). The glow discharge was switched off between each analytical step as well as before changing to a different discharge setting (*the discharge study*). Thereby, 0.5 to 5 mA at 1000 V and 600 to 1500 V at 3 mA were the discharge conditions used. For each discharge condition, five measurements were taken on each day. High purity (6N) argon gas was used as the discharge gas, and the quantification was based on stdRSFs. It is important to mention that

the set of stdRSFs used in this study is based on VG9000 and was supplied along with the Astrum GD-MS by Nu Instruments. Therefore, all discussed and graphically shown concentrations (mass fraction) are the result of calculations.

An integration time of 160 ms was used for the matrix element (Ta181), while for the other elements, an integration time of 80 ms was used. The number of peak widths and number of steps in the window were set to 4 and 100, respectively. Before each data acquisition, sufficient time was allowed for the voltage to stabilize. The sample was taken out of the ion source at the end of the day (*Day 1*) and re-inserted the following day (*Day 2*) to observe the external reproducibility of *the discharge study*. Thereby, five and ten replicates were taken to evaluate the internal and external reproducibility, respectively. RSD 1 and RSD 2 represent the relative standard deviations calculated based on five measurements taken on *Day 1* and *Day 2*, respectively. The equations used for determining the average and standard deviation (based on the mean) are mentioned in ref. 1.

## C. Results and discussion

### Signal stability and sample homogeneity

The prerequisite for the type of work presented here is sufficient sample homogeneity with impurities well above detection limits. In the quantification of low level analytes, relative standard deviations (RSDs) above 30% (ref. 2) can lead to ambiguity in data interpretation. Indeed, to obtain a stable signal, an ion population with low variation is required. First, the equilibrium between sputtering, ionization and ion transmission must be established; second, the intensities of the analytes must be above the statistic noise of the detector in order to achieve low RSD values. The first step of the workflow (Fig. 1) allowed the selection of the isotopes with the lowest RSDs. The signals of Ar40, Ta181, Si28, O16, P31, Na23, and Nb93 ions were sufficiently stable for more than one hour before and after the discharge study (Fig. 2). Hence, the sample can be considered to be sufficiently homogeneous, and the selected isotopes are suitable for the next steps.

### Reproducibility

The Astrum instrument can be operated in two modes, the so-called *constant current* and *constant voltage* modes, where the instrumental readbacks are used to stabilize the selected parameter (current or voltage) by allowing the other parameter to change accordingly. It was observed that occasional minor variations or “flickering” of current and voltage occurred in constant voltage mode and constant current mode, respectively. The variations were smaller in the range of  $\pm 0.05$  mA and were less frequent in constant current mode than in constant voltage mode. This observation is in agreement with the generally accepted explanation, *i.e.* a random spark leads to an increase in current and a decrease in voltage. Because regulation of the power supply attempts to reduce the current by lowering the voltage, the probability of generation of the next random spark is lowered, leading to less variation. In contrast, in constant

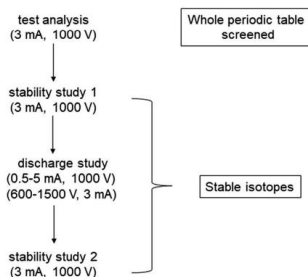


Fig. 1 The analytical workflow for studying the effects of discharge parameters on the quantification of impurities present in a homogeneous tantalum pin.



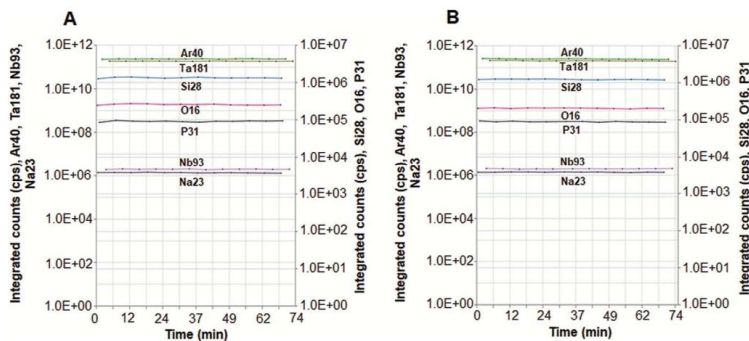


Fig. 2 The stability study of various elements/isotopes in the tantalum pin before (A) and after (B) discharge study, both measured at 3 mA and 1000 V.

voltage mode, the decreased voltage leads to an increase in voltage, *i.e.* the probability of a random spark is increased even further. It should be noted that these occasional minor variations in current did not produce noticeable effects on the reproducibility of the quantification. Hence, the constant current mode was considered as the preferred control mode for the Astrum instrument and especially for this study to minimize possible instrument-related effects which could hinder the reproducibility of the measured intensities.

The glow discharge is maintained by secondary electrons emitted from the cathode (sample) surface.<sup>16</sup> The stability of the glow discharge is governed by the stability of the boundary conditions and the stability of the energy and particle flow (atoms, ions and electrons) between the glow discharge and surrounding environment. Hence, it is not advised to acquire data before the voltage stabilizes.<sup>17</sup>

A low level of discharge gas flow hampers the discharge maintenance; hence, experiments with a discharge gas flow below  $\sim 0.1$  sccm are practically impossible. Indeed, at very low levels of discharge gas flow, it becomes very difficult to start, sustain and stabilize the plasma. At a discharge gas flow closer to the abovementioned level, due to the problem of sustaining the plasma, the external reproducibilities of P31, Na23 and Nb93 are affected when operated at 0.5 mA and 1000 V (see Fig. 3, 4, and Table 1). Thereby, the external RSDs are  $\sim 17\%$  and  $\sim 14\%$  for P31 at 0.5 and 1 mA, respectively, at 1000 V (Table 1). Additionally, better agreement is observed at a higher current (see Fig. 3, 4, and Table 1). In general, there is good agreement of quantification during operation at 600 to 1500 V and 3 mA (Fig. 3, 4 and Table 2).

It should be emphasized that for reproducibility, it is also important to minimize the effects of the instrument and the operator. The homogeneity of a sample can be evaluated and tested by various means, such as the presence of precipitates, which can seriously influence the population of ion species at

a given point in time and affect the RSD as reported by Modanese *et al.*<sup>18</sup> In a recent study, Storey *et al.* demonstrated the necessity of combining imaging tools with GDMS to identify heterogeneous inclusions.<sup>19</sup> We shall not discuss this point further because it is not in the scope of the present study.

From the instrument point of view, because the discharge gas flow affects both the current and voltage, it is crucial to check the stability of the argon flow. The reproducibility is considerably affected if the discharge gas flow is not uniform. The Astrum software allows the operator to monitor the signal stability of the desired isotope. In general, it is recommended to plot the intensity of the discharge gas or that of the matrix element as the instrumental readback of the discharge gas fluctuates. It is not surprising to observe “flickering” by

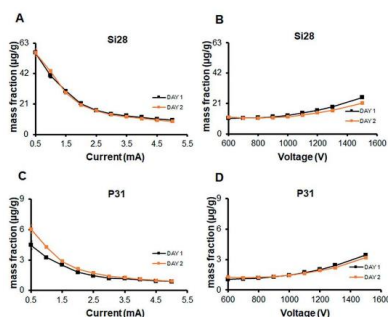


Fig. 3 The changes in the quantification of impurities in the tantalum pin, Si28 (A and B) and P31 (C and D), on different days upon changes in current and voltage.



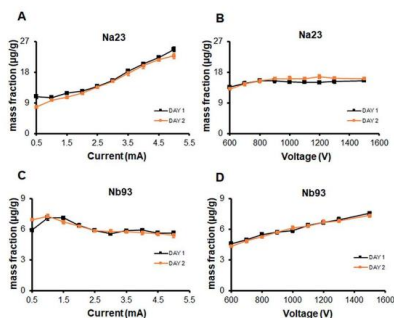


Fig. 4 The changes in the quantification of impurities in the tantalum pin, Na23 (A and B) and Nb93 (C and D), on different days upon changes in current and voltage.

approximately  $\pm 0.01 \text{ mL min}^{-1}$  (scm, where scm is standard cubic centimetres per minute). However, in the experience of the authors, this fluctuation does not produce a noticeable effect on the reproducibility of the quantification. The discharge gas flow rate varies from sample/matrix to sample/matrix depending on the desired current and/or voltage setting. However, in general, 0.2 to 1  $\text{mL min}^{-1}$  (scm) are typical observed values. The monograph by Nelis and Payling provides detailed practical information on the smooth operation of GD-based instruments and other considerations in the laboratory.<sup>29</sup>

Similarly, the operator manually assembles the GD cell, mounts the sample into the sample holder, and inserts the sample holder into the GD chamber. Maximum care is needed to avoid unwanted discharge gas leakage, which would randomly alter the discharge gas flow, *i.e.* the discharge current and/or discharge voltage. For example, a firm and consistent push of the sample probe against the anode body is important to avoid gaps. Thus, to maintain external reproducibility, the

operator should aim to replicate the same position when inserting the sample. Thereby, the same length of pin should always extend out of the sample holder. The length and cross-section of the sample should be kept constant as much as possible.

#### Discharge study and importance of integrated intensities

Tables S1 and S2† summarize the average values (average of both days) with fold changes after normalizing to 3 mA and 1000 V. As can be observed from Fig. 3, the quantification of Si28 and P31 follows the same trend, *i.e.* decrease with increasing current and increase with increasing voltage. Thereby, the calculated concentrations of Si28 and P31 change  $\sim 4$  to 0.7-fold when operated with current supplies of 0.5 mA and 5 mA, respectively (Table S1†). Similarly, the concentration of Si28 changes 0.9 to  $\sim 2$  fold when operated at voltages of 600 V and 1500 V, respectively (Table S2†). Comparable values were seen for P31 (Table S2†). A linear increase in the concentration of Na23 from 0.6 to 1.5 fold was observed with increasing current supply from 0.5 to 5 mA (Fig. 4 and Table S1†). For Nb93, the concentration changed slightly more than 1-fold up to 2 mA; beyond that, the quantification remained steady (Fig. 4 and Table S1†). Na23 was found to be unaffected by changes in voltage, while Nb93 linearly changed 0.7 to 1.2 fold from 600 to 1500 V (Fig. 4 and Table S2†).

The integrated intensities of the individual analytes and the matrix element are plotted together in Fig. 5. These graphs illustrate why the calculated concentrations of some analytes are nearly independent of the discharge conditions while others change dramatically. Thereby, rapid increment of the sodium intensity compared to that of tantalum (Fig. 5A and C) leads to a linear increment in the sodium concentration from 0.5 mA to 5 mA (Fig. 4A). Likewise, the phosphorus intensity rises slowly compared to that of tantalum (Fig. 5A and E), leading to a rapid decrease in its concentration (Fig. 3C). This effect is more dramatic compared to the voltage increment (Fig. 3D). A similar effect to phosphorus was observed with silicon (Fig. 5A, G and 3A, B). Likewise, at lower currents (up to 2 mA), the niobium intensity increased at a slightly faster rate compared to that of

Table 1 The internal (IR) and external quantification reproducibilities (ER) of various impurities present in a tantalum pin upon changes in current

Current (mA)	Si28			P31			Na23			Nb93		
	IR (%)			IR (%)			IR (%)			IR (%)		
	RSD1	RSD2	ER (%)	RSD1	RSD2	ER (%)	RSD1	RSD2	ER (%)	RSD1	RSD2	ER (%)
0.5	0.9	4.8	3.2	8.8	6.6	17.4	5.2	5.4	17.9	3.7	1.5	8.7
1.0	4.2	3.2	4.8	2.5	2.4	14.4	3.8	3.1	5.1	3.3	3.0	3.1
1.5	3.2	2.5	3.5	4.0	3.8	7.9	3.3	2.6	6.4	2.4	2.8	3.9
2.0	1.8	3.3	3.2	0.9	1.8	9.1	0.9	1.1	3.0	3.2	0.8	2.3
2.5	3.1	2.3	2.6	3.1	2.7	9.6	4.0	1.5	2.9	0.5	2.6	1.8
3.0	1.9	2.5	2.6	2.2	3.8	9.2	1.4	2.8	2.2	2.0	3.6	3.4
3.5	2.0	4.1	4.0	2.9	3.3	5.4	3.2	4.5	4.1	1.8	2.3	2.2
4.0	1.7	4.6	5.3	3.2	2.7	3.7	1.2	4.0	3.0	2.5	4.2	3.8
4.5	2.3	2.4	4.4	2.7	2.9	4.1	2.7	2.0	2.7	1.6	3.5	2.6
5.0	1.3	3.3	5.5	1.4	3.2	2.8	2.8	3.8	5.2	2.4	4.9	4.1

Table 2 The internal (IR) and external quantification reproducibilities (ER) of various impurities present in the tantalum pin upon changes in voltage

Voltage (V)	Si28			P31			Na23			Nb93		
	IR (%)		ER (%)	IR (%)		ER (%)	IR (%)		ER (%)	IR (%)		ER (%)
	RSD1	RSD2		RSD1	RSD2		RSD1	RSD2		RSD1	RSD2	
600	2.5	1.7	4.9	5.7	2.5	10.6	2.2	2.5	3.0	2.5	1.8	3.5
700	3.8	4.4	3.9	5.0	3.7	6.7	4.3	4.3	4.1	3.3	4.1	3.7
800	4.3	3.8	4.0	2.9	2.2	4.0	1.5	3.5	2.6	2.9	2.0	3.2
900	4.2	2.0	4.2	4.5	2.1	3.5	4.1	2.3	3.8	3.0	1.2	2.2
1000	2.0	4.4	4.6	1.2	3.5	2.4	2.5	4.3	4.8	3.0	3.6	3.8
1100	3.3	1.0	5.7	2.2	2.1	3.2	2.5	2.5	4.2	1.1	2.7	1.9
1200	2.8	1.2	5.8	2.6	1.4	3.5	2.6	3.8	6.3	2.1	3.6	2.8
1300	4.3	3.4	8.4	2.5	3.1	5.8	4.4	2.9	4.7	3.1	2.3	2.7
1500	1.8	3.4	9.2	2.0	3.2	4.6	1.3	2.7	2.8	1.7	2.7	2.6

tantalum (Fig. 5A and I). However, similar changes in intensity at higher currents (beyond 2 mA) led to steady quantification (Fig. 4C).

If the dependence of the matrix element intensity on the discharge conditions exhibits the same or a similar pattern to that of an analyte, the  $IBR_{X/M}$  of the analyte does not change with the discharge conditions. Hence, the resulting concentration does not change, *i.e.* RSF is independent or nearly independent of the discharge conditions. For example, as can be seen from Fig. 5B and D, the tantalum intensity changes in a similar way to the sodium intensity; hence, the concentration of sodium is independent of the voltage increment (Fig. 4B). The phosphorus intensity increases faster with increasing voltage than that of tantalum; hence, the phosphorus concentration tends to increase with increasing voltage (Fig. 5B, F and 3D). A similar effect was observed with silicon (Fig. 5B, H and 3B). The higher increment of niobium intensity compared to that of tantalum as a function of voltage leads to a linear increment of the Nb concentration (Fig. 5B, J and 4D). Still, the effect is less drastic compared to those of silicon and phosphorus as a function of current (Fig. 3A and C). Thus, the comparative changes in the intensities of individual analytes to that of the matrix element are much more profound with increasing current than with increasing voltage. It is plausible that the faster increments in intensity of some isotopes over others is linked to differences in the ionization energies and/or transport of the isotopes. However, because the ions are extracted in proximity to the GD cell exit orifice, it is challenging to distinguish which process plays the dominant role. Because diffusion and convection are major transport mechanisms towards the orifice, at higher flow rates, lighter elements are expected to diffuse faster than heavier elements. It is likely that the rapid increment of sodium intensity compared to that of tantalum can be linked to this. Also, the contribution of the low ionization energy of sodium (5.1 eV) should not be neglected. A similar explanation was reported in a recent publication by Gonzalez-Gago *et al.* in an Element GD instrument, where the RSFs of lighter elements decrease compared to that of the matrix at higher discharge gas flow rates.<sup>13</sup> Because the Element GD and Astrum GD-MS differ from each other considerably in

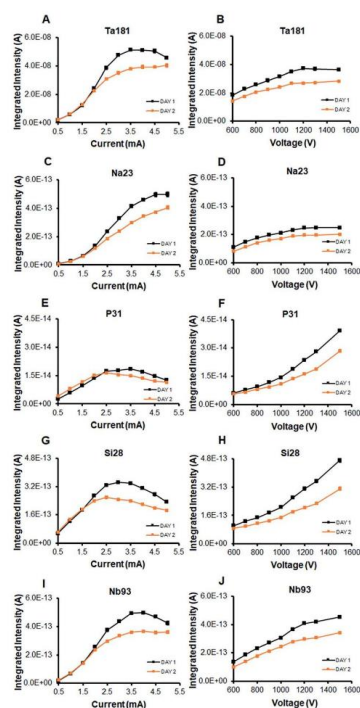


Fig. 5 The changes in the integrated intensities of Ta181 (A and B), Na23 (C and D), P31 (E and F), Si28 (G and H), and Nb93 (I and J) as a function of changes in current (left panel) and voltage (right panel).

terms of discharge parameters, such as gas flow rates and current, few conclusions can be drawn.

The approach of comparing changes in the intensities of the matrix and analytes can aid the selection of the optimal parameters to reduce quantification uncertainty according to an analytical goal/task and sample/matrix. As explained above, for most isotopes presented in this study, there are minimal or small changes in the concentrations of impurities in the 600 to 1500 V range compared to 0.5 to 5 mA. Indeed, the intensities of all isotopes are positively correlated with good correlation factors (all above 0.8) in the 600 to 1500 V range (Table 3). However, the spread of the correlation factors observed in the 0.5 to 5 mA range is much wider (Table 4). This indicates that voltage change has less impact on the changes in ionization from element to element regardless of differences in their ionization energies. Thereby, both the matrix and the impurity elements are ionized more similarly during voltage changes than during current changes. This again shows that constant current mode is a better choice for GDMS operation because the quantification is less sensitive to random discharge voltage fluctuations. However, there are noticeably strong correlations and similarities at current changes in the 0.5 to 5 mA range between different groups of elements. This indicates similarities in the ionization and transport of elements within each group. For example, the strongly correlated group of tantalum, niobium and sodium is not correlated with the group of oxygen and argon, which are also mutually strongly correlated.

It is also useful to compare the trends of the analytes and the matrix element with that of the discharge gas (argon in our case). The argon intensity changes with both current and voltage increments (Fig. 6A and B). Unlike with voltage

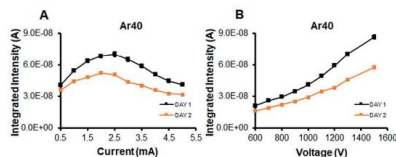


Fig. 6 The changes in the integrated intensity of Ar40 upon changes in current (A) and voltage (B).

increment, the argon intensity does not necessarily always increase with increasing current. The intensity of argon reaches its maximum around 2.5 mA, then starts to decline (Fig. 6A). It is beyond the scope and purpose of this study to provide a detailed explanation; however, some possible explanations for this observation are worth mentioning.

Both current and voltage increment require changing of a third parameter, Ar flow (discharge gas pressure). Thereby, the current increases with increasing argon flow, while the voltage decreases with increasing argon flow (Fig. 7). Changes in Ar flow (pressure) in both modes of operation have an influence not only on the different ionization processes, but also on the transport of the sputtered material. It should be mentioned that the mean free paths of all plasma particles, including fast-energetic electrons, originating at and near the cathode (sample) surface are indirectly proportional to the discharge gas pressure. The fast-energetic electrons are solely responsible for ionizing argon atoms. This means if fewer fast energetic electrons reach the area in proximity of the exit slit, from where all detected ions are extracted, a lower argon intensity should be observed. The intensity of argon indeed saturates and then declines after a certain point of the argon flow (Fig. 6A). This suggests that the number of fast-energetic electrons reaching proximity of the ion exit slit decreases from that point despite the increasing production of fast-energetic electrons with increasing discharge current. A plausible explanation is a decline in the mean free path with increasing argon pressure. Wagatsuma *et al.* performed a similar study with discharge gas intensity (argon) and matrix ions (Ni, Fe). The results are in agreement with each other.<sup>21</sup>

The argument presented above is consistent with the opposite situation, where the discharge current is kept constant and

Table 3 The correlation study based on the average integrated intensities (average of both days) of various isotopes under discharge conditions of 600 to 1500 V, 3 mA

Correlation	Ta181	O16	Ar40	Na23	Si28	P31	Nb93
Ta181	1.000						
O16	0.823	1.000					
Ar40	0.874	0.993	1.000				
Na23	0.998	0.809	0.861	1.000			
Si28	0.861	0.997	0.997	0.848	1.000		
P31	0.833	1.000	0.994	0.820	0.999	1.000	
Nb93	0.984	0.911	0.946	0.977	0.938	0.918	1.000

Table 4 The correlation study based on the average integrated intensities (average of both days) of various isotopes under discharge conditions of 0.5 to 5 mA, 1000 V

Correlation	Ta181	O16	Ar40	Na23	Si28	P31	Nb93
Ta181	1.000						
O16	-0.015	1.000					
Ar40	-0.132	0.989	1.000				
Na23	0.952	-0.292	-0.408	1.000			
Si28	0.827	0.548	0.447	0.626	1.000		
P31	0.836	0.531	0.430	0.639	0.999	1.000	
Nb93	0.998	0.039	-0.079	0.936	0.856	0.865	1.000

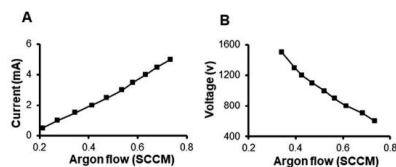


Fig. 7 The relationship between current and voltage with argon flow using a Ta pin at 1000 V (A) and 3 mA (B).

the voltage is increased with decreasing argon flow (Fig. 6B). The mean free path increases; hence, more fast electrons are delivered to the ion exit slit, *i.e.* the argon intensity continuously increases with the discharge voltage.

It is commonly agreed that there are three major ionization mechanisms responsible for the ionization of species in glow discharge plasma, namely electron impact, Penning ionization and asymmetric charge transfer ionization. Additionally, in fast-flow GD instruments such as the Element GD, a post-ionization mechanism, referred to as secondary discharge ionization, has been reported to ionize species in the region close to the skimmer.<sup>22</sup> However, this is rather unlikely in slow-flow instruments such as the Astrum GD-MS, where a lower current density means lower pressure and the probability of ignition of a secondary discharge is reduced.

All analytes can be ionized by their electron impact (interaction with fast energetic electrons). Most analytes with first ionization potentials below the metastable energies of argon (11.55 eV and 11.72 eV), *i.e.* excluding Ar and few other elements, can be ionized by the Penning ionization process. Ionization by direct energy transfer can be important for a few elements under specific conditions, where the difference in energy levels between the analyte ion and that of argon is about 0.2 to 1 eV.<sup>23</sup> This means that a slightly to considerably different mix of ionization processes ionizes each analyte. Thus, it is not surprising that the dependence of the intensities of some elements on the discharge conditions is similar but that other elements are correlated less or not at all. For example, the intensity of phosphorus closely but not exactly follows the argon intensity. This may be due to the fact that the first ionization potential of phosphorus is relatively high, about 10.49 eV. Thus, Penning ionization is still possible but most likely does not contribute strongly, *i.e.* the electron impact ionization is dominant in the mix. The intensity of oxygen, which has a higher first ionization potential than argon, follows an even more similar pattern to the argon intensity (Fig. 8). Remarkably, the changes in the calculated concentrations of silicon and phosphorus as a function of the discharge parameters show similar trends to that of oxygen (Fig. 3A–D and 9). It is probably not surprising that there is an obvious similarity between the dependence of the intensities of Ta and Nb as a function of both current and voltage (Fig. 5A, B, I and J) because tantalum and niobium are very closely related elements in many aspects, such as first ionization energy. It should be emphasized that elements with first ionization potentials below the metastable

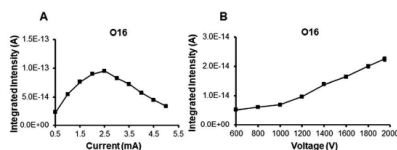


Fig. 8 The changes in the integrated intensities of O16 upon changes in current (A) and voltage (B).

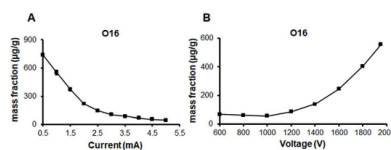


Fig. 9 The changes in the quantification of O16 present in the tantalum pin upon changes in current (A) and voltage (B).

energies of argon can be ionized by both electron impact and Penning ionization.

As mentioned in eqn (2), the RSF is the slope of the standard mass fraction of an element *versus* its measured abundance-corrected ratio of intensities,  $IBR_{X/M}$ . The tantalum pin used for this study is not a certified sample. However, with bulk certified standards, the mass fraction is known (certified/fixed point); thus, changes in  $IBR_{X/M}$  lead to changes in the RSF at different discharge settings. As discussed, comparison of the absolute intensities of trace elements to those of the matrix and discharge gas ion can provide useful information on the uncertainty associated with RSF; this provides clues to the possible mechanisms of ionization and similarities/differences in the ionization of various elements. It is therefore important to consider the discharge conditions used for the certification of standards to achieve better evaluation of RSF uncertainties, measurements and establishment. It should also be noted that the surface temperature may change due to variation of the discharge power. The thermal conductivity of the sample plays a significant role in this effect.<sup>17</sup> These effects may contribute to changes in the absolute intensities with changing GD conditions; this illustrates the importance of monitoring the absolute intensities when optimizing and selecting GD conditions for a given matrix.

## D. Conclusions

This study describes the impact of discharge parameters on quantification. It is shown that the calculated concentration of impurities is dependent on the discharge parameters and can vary as much as several fold. This observation is explained by the differences in the trends of the intensities of trace and matrix elements as well as the discharge gas (argon). Although most of the integrated intensities of the isotopes show similar trends with changes in current/voltage, they are not exactly the same. This leads to changes in  $IBR$  under different discharge settings. Remarkably, this phenomenon can be attributed to the changes in RSF under different discharge conditions. The method of mapping the intensities as a function of the discharge conditions can aid the selection of optimal parameters for a specific analytical task and goal. However, a wide range of matrices and sample forms containing various trace elements must be further tested to confirm and investigate the reasons and phenomena behind this observation. Attention should be paid to minimize any variation related to external



reproducibility, such as sample introduction and discharge gas leakage.

## Conflicts of interest

The authors have no conflicts to declare.

## Acknowledgements

The authors are thankful to Nu Instruments representatives James Wright, Benoit Disch and Christopher Page for fruitful discussions on various occasions.

## Notes and references

- 1 M. Di Sabatino, *Measurement*, 2014, **50**, 135–140.
- 2 C. Venzago, L. Ohanessian-pierrard, M. Kasik, U. Collisi and S. Baude, *J. Anal. At. Spectrom.*, 1998, **13**, 189–193.
- 3 C. D. Quarles, J. Castro and R. K. Marcus, in *Encyclopedia of Spectroscopy and Spectrometry*, ed. J. C. Lindon, G. E. Tranter and D. W. Koppenaal, Academic Press, Oxford, Third edn, 2017, pp. 30–36, DOI: 10.1016/b978-0-12-803224-4.00056-x.
- 4 A. A. Ganeev, A. R. Gubal, K. N. Uskov and S. V. Potapov, *Russ. Chem. Bull.*, 2012, **61**, 752–767.
- 5 C. Venzago and J. Pisonero, in *Sector Field Mass Spectrometry for Elemental and Isotopic Analysis*, The Royal Society of Chemistry, 2015, pp. 319–380, DOI: 10.1039/9781849735407-00319.
- 6 L. Lobo, B. Fernández and R. Pereiro, *J. Anal. At. Spectrom.*, 2017, **32**, 920–930.
- 7 J. Pisonero, J. M. Costa, R. Pereiro, N. Bordel and A. J. A. Sanz-Medel, *Anal. Bioanal. Chem.*, 2004, **379**, 17–29.
- 8 M. Di Sabatino, C. Modanese and L. Arnberg, *J. Anal. At. Spectrom.*, 2014, **29**, 2072–2077.
- 9 W. Vieth and J. C. Huneke, *Spectrochim. Acta, Part B*, 1991, **46**, 137–153.
- 10 R. Matschat, J. Hinrichs and H. J. A. Kipphardt, *Anal. Bioanal. Chem.*, 2006, **386**, 125–141.
- 11 T. Gusarova, PhD thesis, *Bundesanstalt für Materialforschung und -prüfung*, BAM, 2010.
- 12 T. Saka, M. Yamaguchi and K. Ito, *Anal. Sci.*, 2001, **17**, 1841–1844.
- 13 C. Gonzalez-Gago, P. Šmíd, T. Hofmann, C. Venzago, V. Hoffmann, W. Gruner, J. Pfeifer, S. Richter and H. Kipphardt, *J. Anal. At. Spectrom.*, 2019, **34**, 1109–1125.
- 14 P. Walker and W. H. Tarn, *CRC Handbook of Metal Etchants*, CRC Press, Florida, 1990.
- 15 N. Instruments, *Astrum System Manual Iss1.1.1*, Nu Instruments Ltd.
- 16 B. N. Chapman, *Glow discharge processes: sputtering and plasma etching*, Wiley, New York, 1980.
- 17 M. Kasik, C. Michellon and L. C. Pitchford, *J. Anal. At. Spectrom.*, 2002, **17**, 1398–1399.
- 18 C. Modanese, L. Arnberg and M. Di Sabatino, *Mater. Sci. Eng., B*, 2014, **180**, 27–32.
- 19 A. P. Storey, S. J. Ray, V. Hoffmann, M. Voronov, C. Engelhard, W. Buscher and G. M. Hieftje, *Spectrochim. Acta, Part B*, 2016, **126**, 37–43.
- 20 T. Nelis and R. Payling, *Glow discharge Optical Emission Spectroscopy: A Practical Guide*, The Royal Society of Chemistry, 2003.
- 21 K. Wagatsuma, T. Saka, M. Yamaguchi and K. Ito, *J. Anal. At. Spectrom.*, 2002, **17**, 1359–1362.
- 22 M. Voronov and V. Hoffmann, *J. Anal. At. Spectrom.*, 2007, **22**, 1184–1188.
- 23 A. Bogaerts and R. Gijbels, *Spectrochim. Acta, Part B*, 1998, **53**, 1–42.

## Supplementary Information

### List of supplementary information

**Table S1:** The average and fold change of impurities present in tantalum pin upon change in current when normalized against 3 mA, 1000 V.....S1

**Table S2:** The average and fold change of impurities present in tantalum pin upon change in voltage when normalized against 3 mA, 1000 V.....S2

**Table S1:** The average and fold change of impurities present in tantalum pin upon change in current when normalized against 3 mA, 1000 V

Current (mA)	Si28		P31		Na23		Nb93	
	Average (ppm)	Fold change	Average (ppm)	Fold change	Average (ppm)	Fold change	Average (ppm)	Fold change
0.5	56.4	4.1	5.3	4.1	9.3	0.6	6.4	1.1
1.0	41.9	3.1	3.8	2.9	10.2	0.7	7.2	1.3
1.5	29.3	2.1	2.7	2.1	11.3	0.7	6.9	1.2
2.0	20.8	1.5	2.0	1.5	12.2	0.8	6.3	1.1
2.5	16.3	1.2	1.6	1.2	13.8	0.9	5.9	1.0
3.0	13.7	1.0	1.3	1.0	15.5	1.0	5.7	1.0
3.5	12.4	0.9	1.2	0.9	18.1	1.2	5.8	1.0
4.0	11.2	0.8	1.1	0.8	20.2	1.3	5.8	1.0
4.5	10.2	0.7	1.0	0.7	22.0	1.4	5.6	1.0
5.0	9.3	0.7	0.9	0.7	23.8	1.5	5.5	1.0

**Table S2:** The average and fold change of impurities present in tantalum pin upon change in voltage when normalized against 3 mA, 1000 V

Voltage (V)	Si28		P31		Na23		Nb93	
	Average (ppm)	Fold change	Average (ppm)	Fold change	Average (ppm)	Fold change	Average (ppm)	Fold change
600	11.2	0.9	1.1	0.8	13.5	0.9	4.5	0.7
700	10.9	0.9	1.1	0.8	14.7	0.9	4.9	0.8
800	10.9	0.9	1.2	0.8	15.6	1.0	5.4	0.9
900	11.5	0.9	1.3	0.9	15.8	1.0	5.7	1.0
1000	12.2	1.0	1.4	1.0	15.7	1.0	6.0	1.0
1100	13.7	1.1	1.7	1.2	15.7	1.0	6.4	1.1
1200	15.4	1.3	2.0	1.4	15.9	1.0	6.7	1.1
1300	17.3	1.4	2.3	1.6	15.8	1.0	6.9	1.2
1500	23.2	1.9	3.3	2.3	15.9	1.0	7.5	1.2

## **Paper II: Silicon powder analysis**

**Paudel, G.**, and Di Sabatino, M. (2020) Quantification of discharge gas to optimize discharge parameters for relative sensitivity factors (RSFs) determination by slow-flow glow discharge mass spectrometry (GDMS), *Journal of Analytical Atomic Spectrometry* 35, 2748-2757.

Reproduced by permission of The Royal Society of Chemistry





Cite this: *J. Anal. At. Spectrom.*, 2020, **35**, 2748  
DOI: 10.1039/d0ja00281j

## Quantification of discharge gas to optimize discharge parameters for relative sensitivity factors (RSFs) determination by slow-flow glow discharge mass spectrometry (GDMS)<sup>†</sup>

Gagan Paudel<sup>‡\*</sup> and Marisa Di Sabatino

Accurate determination of impurities present in a matrix by glow discharge mass spectrometry (GDMS) requires use of relative sensitivity factors (RSFs). In general, RSFs are obtained from reference materials with a comparable matrix composition as that of the sample being measured. Further, RSFs are sensitive to variation in discharge conditions. Thus, in the present study, various combinations of glow discharge parameters, namely current, voltage and argon flow are studied on a powder certified reference material, NIST silicon 57b, using indium sheets. Likewise, quantification of discharge gas, argon is carried out to facilitate the optimization of GDMS parameters. Furthermore, discharge parameters leading to optimum crater in a flat silicon sample is also considered before selecting optimum discharge condition for RSFs determination. As a result, two sets of RSFs are built – one based on calibrated values reported by NIST and the other based on values obtained after analysis of the same powder by inductively coupled plasma mass spectrometry (ICP-MS). Both sets of RSFs are tested further using another powder certified reference material, NIST 195, using both certified and ICP-MS values. The results of this study indicate that there is no considerable variation in concentration for most of the elements/isotopes including argon when discharge current and voltage are in range of 2–3 mA and 1.2–1.4 kV, respectively. It is found that for most of the elements, RSFs built based on both ICP-MS analysis and certified NIST values give comparable result with error below 20%. However, calcium showed ~80% discrepancy based on certified values as compared to ~10% based on ICP-MS values.

Received 10th June 2020  
Accepted 1st October 2020  
DOI: 10.1039/d0ja00281j  
rsc.li/jaas

### A. Introduction

Glow discharge mass spectrometry (GDMS) consists of glow discharge plasma as an ionization source, which supplies ions to the mass analyser where they are separated based on mass to charge ratio, thus allowing multi-elemental characterization. Various forms of GD sources are reported in the literature.<sup>1,2</sup> Coaxial cathode and Grimm-type source are the most common geometries used in commercial instruments. These GD cell designs allow analysis of pin- and flat-shaped samples, respectively. Further, glow discharge can be operated either in direct current (dc), radio frequency (RF) or pulsed power mode (either dc or RF). While instruments relying in RF power supply can analyse samples regardless of their electrical conductivity, analysis of materials by dc-GDMS require specimen to be sufficiently conductive. Thus, metals and semiconductors can be directly analysed by dc-GDMS, while insulators require some

adjustments. The electrical conductivity of non-conductors can be enhanced by placement of high purity metallic mask, which on sputtering is redeposited on the sample surface forming a thin conductive film.<sup>3,4</sup> Qian *et al.* demonstrated that there could be other means of enhancing the surface conductivity of insulators, such as by coating the sample surface with a conductive metal layer.<sup>5</sup> For characterization of non-conductive powders, they are mixed with high purity metal powders in different proportions and finally processed into pins<sup>6,7</sup> or discs.<sup>8,9</sup> Alternatively, non-conductive powders are pressed into discs without being mixed with conductive filler material. In such instances, a high purity secondary cathode is used to sustain the sputtering process and hence the GD plasma.<sup>10,11</sup> Semi-conductive powders can be either processed into pins or discs and directly analysed, because the use of secondary cathode as such is not required to sustain the GD plasma. Nevertheless, there are approaches where high purity metal sheets are commonly used as a mechanical support against which sufficiently conductive powder sample is adhered or pressed as in the present study. Hence, in this study, commonly applied secondary cathodes, *i.e.* indium sheets, are used to characterize semi-conductive silicon powders.

*Department of Materials Science and Engineering, Norwegian University of Science and Technology, 7491 Trondheim, Norway. E-mail: gagan.paudel@ntnu.no*

<sup>†</sup> Electronic supplementary information (ESI) available. See DOI: 10.1039/d0ja00281j

Accurate elemental characterization of any specimen requires measurement of reference materials of similar composition to that of the sample being measured. In general, both the sample and reference material are analysed simultaneously. Alternatively, relative sensitivity factors (RSFs) built using certified reference materials can be used for quantitative elemental characterisation. One of the major drawbacks of solid-sampling analytical technique, such as GDMS, is the limited availability of calibrated materials and procedures which hinders obtaining quantitative data output. Matschat *et al.* demonstrated that it is possible to dilute high purity powders with impurities in  $\mu\text{g kg}^{-1}$  to  $\text{mg kg}^{-1}$  level to produce pressed calibrated materials. This was performed for zinc and iron powders.<sup>12</sup> The work of Matschat and co-workers was adopted by Gusarova *et al.* to obtain synthetic standards both in flat- and pin-geometry that lead to estimation of RSFs for zinc and copper powders.<sup>13,14</sup> Zhang *et al.* also used similar powder pressing method for building RSFs.<sup>15</sup> These works are promising to provide calibrated materials to compensate the problem of limited availability of matrix matched standards.

The instrument used in the present study, Astrum GDMS, allows cryocooling. Therefore, the powder pressed into indium sheets can be directly analysed without facing any problems despite of low melting point of indium. This approach of sample analysis can be performed routinely and is not time-consuming. To be mentioned measurements of powders and atmospheric particulate matter using indium sheets<sup>16</sup> or metal foils<sup>17</sup> have been previously successfully performed using VG 9000. VG 9000 also offers cryocooling possibility. However, its production is suspended since 2005.

In 2018, Zhang *et al.* estimated RSF of doped impurities in silicon powder using mechanically stable indium-silicon pellets.<sup>18</sup> Earlier in 2011, Di Sabatino *et al.* determined RSFs of doped impurities in silicon ingots.<sup>19</sup> For both works, element GD was used. It is worth mentioning that, in principle, the RSFs are transferable from one instrument to another given that same GD ion source and discharge conditions are adopted.<sup>20,21</sup> Since Astrum GDMS has low-power/low-pressure design unlike the Grimm-type design of element GD, RSFs estimated using element GD cannot be used on Astrum GDMS. Currently, due to the limited availability of matrix matched RSFs using Astrum, the instrument supplier recommends using RSFs determined for VG 9000 using six different matrices to obtain semi-quantitative data.<sup>22</sup> Therefore, in order to increase the quantification accuracy of the Astrum GDMS measurements, RSFs should be determined specifically for the matrix used (*i.e.* silicon powder in this study).

To be stressed, it is common among GDMS users to analyse discharge gas and other elements such as carbon, nitrogen and oxygen with an aim of estimating contribution of interfering peaks to desired peak of interest at a certain mass to charge ratio. To knowledge of the authors, until now it is not demonstrated that measuring discharge gas or other gaseous elements can also be beneficial for optimizing discharge parameters and hence eventually contributing for RSFs determination. Therefore, a few most important analytes for solar cell silicon together with argon were subjected to a range of current and voltage

settings for optimization of discharge parameters using manually pressed NIST certified powders against high purity indium sheets. This followed generation and verification of RSFs for 16 elements using optimum discharge condition. Additionally, the powders from NIST were also analysed by inductively coupled plasma mass spectrometry (ICP-MS); thus, the RSFs built can be further compared and verified. Moreover, RSFs built are also compared against standard RSFs supplied by the instrument manufacturer along with Astrum GDMS.

### Quantification approaches in GDMS

In glow discharge mass spectrometry following equation is generally used for quantification of trace elements present in a specific matrix.

$$C_{X/M} = \frac{I_{X_i}}{I_{M_i}} \times \frac{A_{M_i}}{A_{X_i}} \times \text{RSF}_{X/M} \quad (1)$$

Here,  $C_{X/M}$  is the mass fraction of element/isotope X present in matrix M, while  $I_{X_i}$ ,  $A_{X_i}$  and  $I_{M_i}$ ,  $A_{M_i}$  represent the intensity and natural abundance of analyte and matrix, respectively.  $\text{RSF}_{X/M}$  represents the relative sensitivity factor of specific analyte X present in a specific matrix M. RSFs are estimated mathematically as inverse of the slope of calibration curve  $\text{IBR}_{X'/M}$  versus mass fraction  $C_{X'/M'}$  (eqn (2)). The abundance corrected ion beam ratio  $\text{IBR}_{X'/M'}$  is generated by measurement of calibrated reference material (CRM), reference material (RM) or synthetic standards by GDMS.

$$\text{RSF}_{X/M} = \frac{C_{X'/M'}}{\text{IBR}_{X'/M'}} \quad (2)$$

If matrix specific RSFs is not available, generally semi-quantitative approach is adopted where standard RSF ( $\text{stdRSF}_X$ ) is used as in eqn (3).

$$\text{stdRSF}_X = \frac{\text{RSF}_{X/M}}{\text{RSF}_{\text{Fe}/M}} = \frac{I_{\text{Fe}}}{I_X} \times \frac{C_{X'/M'}}{C_{\text{Fe}'/M'}} \quad (3)$$

Here,  $\text{RSF}_{X/M}$  and  $\text{RSF}_{\text{Fe}/M}$  represent RSF of element/isotope X and Fe in matrix M, respectively.  $I_{\text{Fe}}$  and  $I_X$  refer to abundance corrected intensity of iron and isotope of interest, respectively.  $C_{X'/M'}$  and  $C_{\text{Fe}'/M'}$  represent mass fraction of a trace element/isotope X and iron present in matrix M, respectively.

## B. Experimental

### Sample preparation

Two CRMs, namely NIST 57b silicon and NIST 195 ferrosilicon powder, were procured from National Institute of Standards and Technology (NIST, Maryland, USA). The 7N indium pellets, each of about 1 g in weight, were sourced from RASA industries Ltd. (Tokyo, Japan). Each indium pellet was pressed by mechanical press to obtain indium sheets. This followed treatment of indium sheets with etchant nitric acid for about 1 min. After that it was rinsed 3 times with deionized water and dried in ethanol. The reagents used were of ultrapure grade and

care was taken to avoid contamination. It is recommended to perform etching procedure inside acid fume hood. Nitric oxide formed during the etching procedure as a by-product reacts with air to form nitrous dioxide (yellow fume) that can lead to mucus membrane irritation. Further, it is important to keep indium sheets away from one another during etching. If indium sheets come in contact with each other, they are burnt and can even catch fire. Therefore, the best option is to perform etching of one indium sheet at a time. This way the intensity of yellow fume is also reduced.

#### GDMS method

The instrument (Astrum, Nu Instruments, UK) was tuned and calibrated for different masses with tantalum at discharge condition of 2 mA, 1 kV. Ta181 signal intensity of  $1.2 \times 10^{-9}$  was observed with magnet scan at resolution power of about 4000 ( $M/\Delta M$ , 10% of peak height approach). The instrument was cryogenically cooled and 6N argon was used as discharge gas. For this study, a flat cell GD design was used. The tantalum front plate of the flat sample holder has orifice of 10 mm in diameter. Silicon powders in range of 25–35 mg was pressed manually against the indium sheets and set into the flat sample holder before inserting into the instrument. A tantalum flat sample was placed beneath the silicon pressed indium for mechanical support and to avoid the plasma hitting other parts of sample holder if by chance indium sheet is ruptured. The NIST 57b silicon powder was cooled for about 15 minutes before sputtering for about 15 minutes at discharge condition of 2 mA, 1 kV. Before each measurement, the signal stability of elements/isotopes were checked using the same discharge condition (2 mA, 1 kV). Silicon 57b powder was subjected to discharge condition of 1–3.5 mA and 1–1.4 kV with the aim of checking variation in RSF measurement for a few selected isotopes. Therefore, semi-quantitative approach using standard RSF<sup>22</sup> was used to determine mass fraction of B11, Al27, P31, Cr52, Fe56, Co59 and Cu63 at various current and voltage settings. These elements are relevant for solar cell silicon application.<sup>23,24</sup> Thus, it is necessary to estimate variation in quantification as a result of change in discharge parameters. Further, to understand more about ionization mechanisms and sputtering related effects Ar40 was measured at a slightly different discharge condition range of 1–5 mA and 1.2–1.6 kV. The RSF was calculated based on two sets of external replicates taken at two different dates using NIST 57b silicon powder at discharge condition of 2.3 mA, 1.2 kV using argon flow rates of 0.41 ml min<sup>-1</sup> and 0.35 ml min<sup>-1</sup> respectively. The RSF data was verified at the same discharge condition (2.3 mA, 1.2 kV using argon flow of 0.39 ml min<sup>-1</sup>) using NIST 195 ferrosilicon powder. The instrument was operated in a constant current mode. Indium blank correction was not performed in this study. The matrix signal, Si28 and Fe56 (for NIST 195) and discharge gas signal, Ar40 were detected using Faraday detector. All other isotopes were detected using electron multiplier. The integration time of 160 ms and 80 ms were used for matrix and impurity element/isotope, respectively. The number of peak widths and steps in the method setup used were 4 and 100,

respectively. All measurements were performed at resolution power of 4000 ( $M/\Delta M$ , 10% of peak height approach).

#### ICP-MS sample preparation

Approximately 30 mg of silicon powders were dissolved in 1.5 ml nitric acid followed by addition of 0.5 ml hydrofluoric acid (HF). The clear solution obtained was then diluted to 220 ml using deionized water before ICP-MS analysis. The ICP-MS used is element 2 by Thermo Fischer Scientific (Germany). This procedure is recommended to be performed on Teflon bottles and experiment performer should be careful while adding HF. It is recommended to add HF dropwise to avoid bumping. As HF is hazardous acid its handling requires adequate training regarding use of personal protectives, antidotes usage in case of accidents *etc.* This procedure should be strictly performed in special fume hoods dedicated for HF handling.

#### Interferences

In general, GDMS results into monoatomic or molecular interferences. Since most of the elements exist as multiple isotopes it is possible to select most suitable isotope for material characterization. Selection of some of the isotopes used in this study is discussed. In case argon is used as discharge gas, as in present study, Ca40 which is the most abundant isotope of calcium cannot be used because of the presence of monoatomic interference, Ar40. Instead Ca42 or Ca44 can be used. Therefore, mass fraction values of Ca42 and Ca44 were checked that resulted into similar values. Latter is used in this study. While analysing silicon matrix it is common to observe molecular interference – Si28Si28 that could interfere with the characterization of most abundant isotope of iron, Fe56. At resolution power of 4000 ( $M/\Delta M$ , 10% of peak height approach), the molecular interference appears at the right of the actual iron isotope, Fe56 and is clearly distinguishable. Likewise, most abundant isotope of titanium and nickel, Ti48 and Ni58 suffer monoatomic interference from Ca48 and Fe58, respectively. Nevertheless, Ti48 and Ti47 resulted into similar mass fraction values hence the former is used. Instead of Ni58, Ni60 is used in this study as mass fraction of both Ni60 and Ni62 resulted into comparable values. Likewise, same strategy was adopted for other elements with multiple isotopes.

## C. Result and discussion

#### Indium sheet preparation

There could be several possibilities to source high purity indium which comes in various forms. The indium pellets used in the present study are of uniform size and are manually malleable to process into indium sheets without need of prior cutting (Fig. 1A and B). The indium sheets used in this study are approximately of diameter and thickness 30 mm and 0.40 mm respectively. It is possible to obtain thinner or thicker sheets but are not recommended. Thinner sheets are very soft and weak to handle, while thicker sheets have smaller diameter leading to problems while setting it up on the sample holder. Also, the

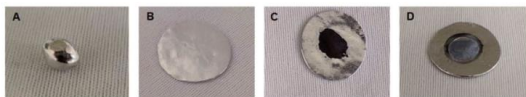


Fig. 1 7N indium pellet (A), indium pellet after mechanical pressing (B), silicon powder pressed on an etched indium sheet (C), and silicon pressed on an etched indium sheet after GDMS analysis (D).

tantalum front plate of the sample holder is about 10 mm in diameter; therefore, indium sheet should be sufficiently large to ensure that glow discharge plasma does not hit other parts of the sample holder. As an extra caution, it is recommended to

place a high purity material beneath powder pressed indium sheet. It is necessary to stress that considering 10 mm tantalum front plate orifice used, 25–35 mg powder was pressed into the indium sheet (Fig. 1C). Caution should be applied not to

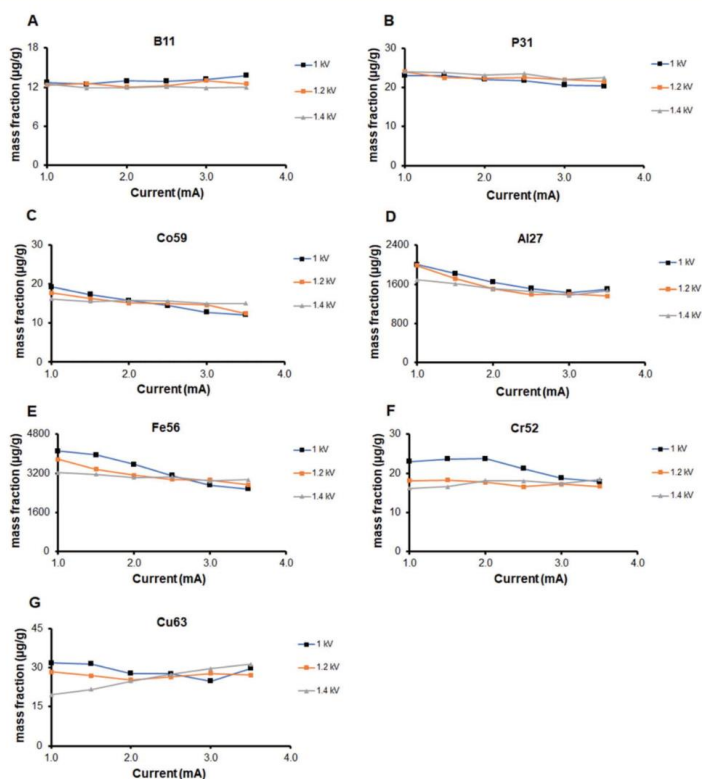


Fig. 2 Variation in concentration of various elements/isotopes, boron (A), phosphorous (B), cobalt (C), aluminium (D), iron (E), chromium (F), and copper (G) upon analysing indium pressed 57b silicon powder with discharge condition in range of 1–3.5 mA and 1–1.4 kV, plotted using standard RSF.



increase the powder diameter far beyond 10 mm otherwise this could lead to a gap between tantalum front plate and indium sheet leading to challenges in plasma sustenance. Fig. 1D demonstrates the sputtered area of indium pressed silicon after a successful analysis. Further, before studying the effect of discharge condition in mass fraction variation and RSF estimation/verification, signal stability of isotopes was checked. A representative figure is shown (Fig. S1†) as an example where most of the isotopes are sufficiently stable within 10 minutes of sputtering. Therefore, the method of powder pressed indium approach is reliable and allows enough time for data acquisition.

#### Optimization of discharge condition

The result of changes in mass fraction of selected analytes in NIST 57b as a function of change in discharge condition are presented in Fig. 2. The argon flow rates used to obtain specific discharge condition is presented as Fig. S2.† The primary dopants for p- and n-type silicon, namely boron and phosphorus, are least affected by the changes in discharge conditions (Fig. 2A and B). Other common impurity elements present in silicon demonstrated some notable changes in their concentration. To evaluate the magnitude of change in concentration, 2.5 mA and 1.2 kV is taken as a reference point. The variation of cobalt is in range of 0.8–1.3 folds when compared against concentration at 2.5 mA, 1.2 kV (Fig. 2C). The concentration of cobalt is least affected in current and voltage range of 2–3 mA and 1.2–1.4 kV, respectively. Aluminium, iron and chromium vary by comparable factor of 1–1.4 with minimum deviation in range of range of 2–3 mA and 1.2–1.4 kV (Fig. 2 D–F). However, for copper the variation is least in range of 2–3 mA and 1–1.2 kV while a linear increase is observed in range of 1–3.5 mA at 1.4 kV (Fig. 2G). As proposed theoretically

by Vieth and Huneke, there could be many processes impacting the RSFs and hence the final concentration of analytes.<sup>22</sup> It is beyond the scope of this paper to discuss all of the details, however, a few occurring within the GD cell are discussed. Paudel *et al.*, using the same instrument (Astrum GDMS), demonstrated that the variation in concentration of analytes is due to differences in absolute intensity changes of analytes as compared to matrix element.<sup>25</sup> One of many factors that can bring about changes in absolute intensities is ionization energy of elements. Both boron and silicon possess similar first ionization energy (8.30 eV and 8.15 eV) which is likely to contribute to similar absolute intensity change from one discharge condition to another (Fig. S3A and B†). Hence, minimal changes in concentration (Fig. 2A). This also applies to phosphorus although it has slightly higher first ionization energy (10.49 eV) (Fig. 2B and S3A and C†). It is worth mentioning that the likelihood of both silicon and phosphorus to be ionized by electron impact using Astrum GDMS is known.<sup>25</sup> Electron impact is a non-selective ionization mechanism, which can ionize all elements including the discharge gas, argon in this study. Thus, measurement of argon helps to track the range of discharge condition where all elements are ionized in more or less similar manner. Therefore, an additional experiment was performed after obtaining Fig. 2, where argon was measured using NIST 57b powder at a different discharge condition in range of 1–5 mA and 1.2–1.6 kV (Fig. 3A). The relationship between argon flow rate with current and voltage is shown in Fig. 3B. Three distinct regions can be observed in Fig. 3A, (i) slight drop of argon concentration in 1–2 mA, 1.2–1.6 kV range; (ii) concentration nearly unchanged in 2–3 mA, 1.2–1.6 kV range; and (iii) increase of concentration beyond 3 mA at 1.2–1.6 kV. It is reasonable to expect that sputtering rate increases with increase in discharge current and voltage<sup>26,27</sup> which would likely

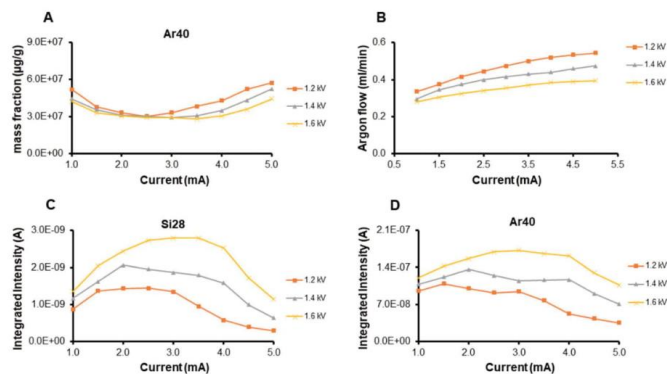


Fig. 3 Variation in quantification of argon (A) obtained after subjecting it to the change in argon flow at various discharge conditions (B). Subsequent change in absolute intensity of silicon (C), and argon (D), respectively, upon analysing indium pressed 57b powder at discharge condition in range of 1–5 mA and 1.2–1.6 kV.

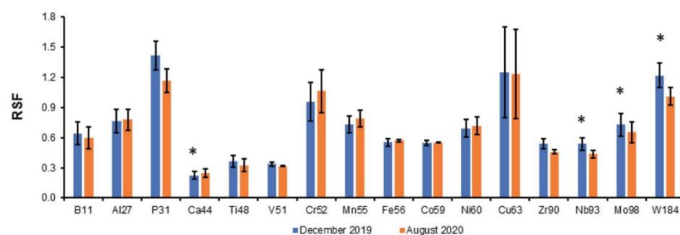


Fig. 4 Comparison of relative sensitivity factors (RSFs) obtained at different times after analysing NIST 57b silicon powder at discharge condition of 2.3 mA, 1.2 kV, \* represents RSFs calculated based on ICP-MS measurements while others are based on silicon 57b certified values.

contribute to increment in silicon ion population. This explains why a relatively sharp increase in absolute intensity of silicon is observed as compared to argon in 1–2 mA, 1.2–1.6 kV range (Fig. 3C and D). The second part of the curve is most interesting as it is likely that in this range of discharge condition (2–3 mA, 1.2–1.6 kV) both silicon and argon are ionized in more or less similar manner. The last part of the curve suggests that the population of argon ions is higher as compared to silicon ions which can be explained through high first ionization energy of argon (15.76 eV) as compared to silicon (8.15 eV). This observation is consistent and can be verified further by Fig. S4† where quantification change of oxygen and argon shows similar trend. For this study a different form of sample was chosen *i.e.* a flat silicon sample. Further, the range of minimum deviation in concentration of most elements are also in range of 2–3 mA and 1.2–1.4 kV (except copper) (Fig. 2). As mass fraction of all elements are calculated based on silicon (eqn (1)), it is plausible that most of the elements are ionized in similar manner in this range (Fig. 2 and 3A) regardless of different ionization energies.

Besides electron impact, there are other ionizations mechanisms such as asymmetric charge transfer ionization (ACT) and Penning ionization that play a role in ionization process. To determine the contribution of each ionization mechanisms, modelling works are necessary especially at/around the exit aperture of GD cell. However, the authors are not aware of modelling works in Astrum. The instrument that comes close to Astrum in terms of GD cell design and discharge parameters used

is VG 9000. Bogaerts and co-workers have developed models using VG 9000 suggesting elements that can be ionized by ACT.<sup>28</sup> Among the elements in Fig. 2, cobalt, iron, chromium and copper are likely candidates to be ionized by ACT as these elements lie within energy levels close to argon (0.2–1 eV).<sup>28</sup> Likewise, theoretically all elements except for argon in the present study can be ionized by Penning ionization mechanism. However, the contribution of each ionization mechanism most likely is not same at all discharge settings which probably explains why there are some discrepancies in concentration in some discharge condition while there is minimum variation in others. Due to inadequacies of modelling work, many conclusions cannot be drawn.

Lastly, for fast-flow GDMS instrument, element GD, Gonzalez-Gago *et al.* argued that variation of RSFs, and thus concentration, can be attributed to atomic mass differences of matrix and analytes. This leads to variation in diffusion and transportation of ions towards the exit orifice of GD cell from where they are extracted.<sup>29</sup> Astrum uses discharge gas flow rate which are 3 orders lower as compared to element GD (Fig. S2†). Nevertheless, diffusion related effects are also likely with Astrum GDMS. This potentially is the explanation for why higher atomic mass containing elements such as niobium, molybdenum and tungsten show variation in RSF values (Fig. 4).

#### Indium to silicon intensity ratio

There could be several criteria based on which a specific discharge condition is chosen for sample analysis. In this study

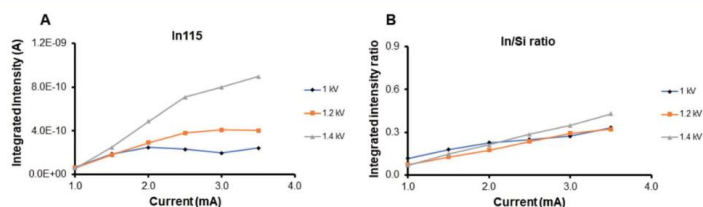


Fig. 5 Variation in integrated intensity of indium (A) and indium to silicon integrated intensity ratio (B) upon analysing indium pressed 57b powder at discharge condition in range of 1–3.5 mA and 1–1.4 kV.

emphasis is given to minimize the variation in RSF. For studies involving use of secondary cathodes, discharge condition can also be selected with an aim of obtaining lower intensity of indium as compared to matrix ion. In experience of the authors, when indium and silicon are analysed separately the integrated intensity of indium is at least one order higher than that of silicon. However, in this study as indium lies beneath silicon powder, former is less exposed to plasma and results into lower intensity as compared to silicon ion (Fig. 5A and S3A†). This is not surprising as there is decrease in surface area of indium. Thus, one way of increasing silicon intensity further, while decreasing that of indium, could be to increase the amount of powder pressed into indium sheets. Nevertheless, attention should be paid to avoid creating a gap in between tantalum front plate and ceramics, as this could lead to instability in plasma resulting to current and/or voltage fluctuation.

The ratio of indium to silicon shows a linear trend when analysed from lower to higher current. Likewise, highest In : Si ratio is seen at voltage of 1.4 kV (Fig. 5B). This is likely because of higher sputtering rates of indium as compared to that of silicon. Therefore, theoretically, application of higher power should likely lead to further increase in relative sputtering rate although some discrepancies is observed when compared practically at lower power (Fig. 5B). Lastly, one should keep in mind that when silicon powder is sputtered, more indium is exposed, leading to further increase in indium intensity. Thus, use of too little powder is not advised. Therefore, a compromise between use of two extreme cases of powder amount is required.

### RSF determination and verification

This study is aimed to determine RSFs using discharge condition where its variation is minimum. As current and voltage in range of 2–3 mA and 1.2–1.4 kV, respectively leads to minimal deviation in quantification for most of the elements including argon, it is therefore appropriate to take a discharge setting within this range. To facilitate comparison of silicon powder analysis with that of flat silicon samples, discharge setting leading to optimum crater in flat silicon sample was obtained (Fig. S5†). Since discharge current setting of 2.3 mA used for obtaining flat crater is within the range of 2–3 mA, 2.3 mA and 1.2 kV is finally considered as optimum discharge current and voltage respectively for RSFs determination.

The average values along with relative standard deviation (RSD), calculated based on expanded uncertainties as reported in NIST certificates of silicon 57b and ferrosilicon 195, are given in Table S1.† Likewise, ICP-MS reference values with three other elements that are not reported in the certificates, namely niobium, molybdenum and tungsten, are also presented in Table S1.† As can be observed, the uncertainty associated with ICP-MS analysis is in range of 1–19%, while that for most of the elements it is below 5% indicating that ICP-MS analysis was successful. Table 1 summarizes the results of RSFs estimated based on NIST certificates 57b, verification of estimated RSFs using ferrosilicon 195 values and comparison against stdRSF as reported by Vieth and Huneke.<sup>22</sup> It is worth mentioning that stdRSF is normalized against iron. However, in this work these

Table 1 Summary of estimation of relative sensitivity factors based on values reported in NIST 57b and 195 certificates<sup>a</sup>

Element/ isotope	Determination of RSF based on NIST 57b			Verification of RSF based on NIST 195			Comparison against stdRSF			
	Reference $C_{X,SI95}$ ( $\mu\text{g g}^{-1}$ )	Measured $\text{IBR}_{X,SI95}$ ( $\mu\text{g g}^{-1}$ )	RSF	Measured $\text{IBR}_{X,SI95}$ ( $\mu\text{g g}^{-1}$ )	Mass fraction on applying RSF ( $\mu\text{g g}^{-1}$ )	Reference $C_{X,SI95}$ ( $\mu\text{g g}^{-1}$ )	Error <sub>RSF</sub> (%)	stdRSF <sub>SI95</sub> ( $\mu\text{g g}^{-1}$ )	Mass fraction on applying stdRSF ( $\mu\text{g g}^{-1}$ )	Error <sub>stdRSF</sub> (%)
B11	12.5 ± 2.1	19.8 ± 0.9	0.63 ± 0.11	16.2 ± 0.9	10.2	10.5 ± 1.6	3	0.62	10.0	4
Al27	1690.0 ± 220.0	2207.7 ± 135.5	0.77 ± 0.11	711.3 ± 43.6	544.5	460.0 ± 90.0	18	0.71	505.0	−10
F31	16.3 ± 1.5	12.1 ± 1.1	1.36 ± 0.17	119.0 ± 6.4	160.5	190 ± 88	16	1.79	213.0	−12
Cr44	22.2 ± 4.5	33.9 ± 2.6	0.70 ± 0.15	1505.6 ± 108.8	987.4	540.0 ± 190	−83	0.29	436.6	19
Ti48	346.0 ± 49.0	985.8 ± 101.6	0.35 ± 0.06	1021.7 ± 53.1	358.6	367.0 ± 38.0	2	0.21	214.6	42
V51	25.0	76.0 ± 4.4	0.33 ± 0.02	55.6 ± 4.1	18.3	—	—	0.28	15.6	—
Cr52	17.3 ± 3.3	17.8 ± 1.1	0.98 ± 0.20	421.9 ± 22.9	410.4	474.0 ± 39	13	1.14	481.0	−1
Mn55	78.2 ± 7.2	105.3 ± 6.9	0.75 ± 0.09	1962.8 ± 49.3	1457.8	1710.0 ± 50.0	15	0.76	1491.7	13
Fe56	3400.0 ± 60.0	6150.2 ± 358.6	0.55 ± 0.02	373 507.2 ± 231.8	206 486.2	236 200.0 ± 1200	13	0.51	190 488.7	19
Co59	14.0	25.7 ± 1.1	0.55 ± 0.02	56.9 ± 1.0	31.1	—	—	0.58	33.0	—
Ni60	15.3 ± 1.7	21.6 ± 0.8	0.71 ± 0.08	413.4 ± 13.0	292.3	318.0 ± 20.0	8	0.79	326.6	−3
Cu63	17.2 ± 5.8	13.9 ± 1.3	1.25 ± 0.44	304.6 ± 29.9	376.4	468.0 ± 24.0	20	2.53	770.6	−65
Zr90	17.8 ± 0.6	34.4 ± 3.5	0.52 ± 0.06	192.9 ± 8.5	99.8	110.0 ± 66.0	9	0.33	63.7	42

<sup>a</sup> Measured  $\text{IBR}_{X,SI95}$  is based on two sets external replicates each of 15 and 5 measurements respectively while  $\text{IBR}_{X,SI95}$  is based on 3 measurements. stdRSF is normalized to silicon.

Table 2 Summary of estimation of relative sensitivity factors based on values obtained after analysing NIST 57b and 195 powders by ICP-MS<sup>a</sup>

Element/ isotope	Determination of RSF based on NIST 57b			Verification of RSF based on NIST 195			Comparison against stdRSF		
	Reference $C_{X,NIST57b}$ ( $\mu\text{g g}^{-1}$ )	Measured $IBR_{X,NIST57b}$ ( $\mu\text{g g}^{-1}$ )	RSF	Measured $IBR_{X,NIST195}$ ( $\mu\text{g g}^{-1}$ )	Reference $C_{X,NIST195}$ ( $\mu\text{g g}^{-1}$ )	ErrorRSF (%)	stdRSF <sub>K,SN</sub>	Mass fraction on applying stdRSF ( $\mu\text{g g}^{-1}$ )	Error <sub>stdRSF</sub> (%)
B11	13.1 ± 1.4	19.8 ± 0.9	0.66 ± 0.08	16.2 ± 0.9	9.4 ± 0.4	-14	0.62	10.0	-7
Al27	1548.9 ± 86.4	2207.7 ± 135.5	0.70 ± 0.06	711.3 ± 43.6	434.3 ± 14.1	-15	0.71	505.0	-16
P31	14.3 ± 0.7	12.1 ± 1.1	1.19 ± 0.12	119.0 ± 6.4	139.0 ± 2.8	-1	1.79	213.0	-53
Ca44	7.7 ± 1.2	33.9 ± 2.6	0.23 ± 0.04	1505.6 ± 108.8	387.7 ± 29.9	11	0.29	436.6	-13
Ti48	302.8 ± 11.1	985.8 ± 101.6	0.31 ± 0.03	1021.7 ± 53.1	322.2 ± 14.1	3	0.21	214.6	33
V51	23.7 ± 1.0	76.0 ± 4.4	0.31 ± 0.02	55.6 ± 4.1	19.6 ± 0.6	11	0.28	15.6	21
Cr52	15.9 ± 0.6	17.8 ± 1.1	0.90 ± 0.07	421.9 ± 22.9	378.9 ± 6.9	0	1.14	481.0	-27
Mn55	70 ± 2.7	105.3 ± 6.9	0.67 ± 0.05	1962.8 ± 49.3	1398.8 ± 60.1	7	0.76	1491.7	-7
Fe56	3160.3 ± 178.3	6150.2 ± 358.6	0.51 ± 0.04	373 507.2 ± 2315.8	204 555.2 ± 4573.8	6	0.51	190 488.7	7
Co59	11.9 ± 0.6	25.7 ± 1.1	0.50 ± 0.04	56.9 ± 1.0	24.7 ± 0.3	-7	0.58	33.0	-34
Ni60	16.3 ± 0.5	21.6 ± 0.8	0.75 ± 0.04	413.4 ± 13.0	266.3 ± 5.4	-17	0.79	326.6	-23
Cu63	21.5 ± 0.8	13.9 ± 1.3	1.56 ± 0.16	304.6 ± 29.9	387.9 ± 7.5	-21	2.53	770.6	-99
Zn90	19.2 ± 1.5	34.4 ± 3.5	0.56 ± 0.07	192.9 ± 8.5	110.6 ± 7.1	2	0.33	63.7	42
Ni93	1.3 ± 0.1	2.8 ± 0.3	0.47 ± 0.07	4.7 ± 0.1	2.8 ± 0.1	20	0.34	1.6	43
Mo98	2.8 ± 0.4	4.1 ± 0.3	0.68 ± 0.11	98.3 ± 5.9	72.3 ± 0.9	6	0.66	64.9	10
W184	39.3 ± 3.1	36.3 ± 3.7	1.09 ± 0.14	10.7 ± 0.6	13.9 ± 0.5	17	0.74	7.9	43

<sup>a</sup> Measured  $IBR_{X,NIST57b}$  is based on two sets external replicates each of 15 and 5 measurements respectively while  $IBR_{X,NIST195}$  are based on 3 measurements.  $C_{X,NIST57b}$  and  $C_{X,NIST195}$  are based on 3 ICP-MS measurements. stdRSF is normalized to silicon.



values are adjusted after normalizing to silicon, since this is the matrix (*i.e.*  $RSF_{Si}$  equals to 1). The RSF is estimated using eqn (2). The mass fraction for 195 is calculated using eqn (1), where abundance ion beam ratio,  $IBR_{X/Si195}$ , was obtained after GDMS analysis. The external reproducibility of measured abundance corrected ion beam ratio for both powders are quite high, *i.e.* RSD below 10% for most of the elements/isotopes. As can be observed from Table 1, for most of the elements the estimated RSF is close to what is reported by Vieth and Huneke<sup>22</sup> after normalizing to silicon. When compared against the mass fraction values reported in NIST 195 certificate, the error for all elements is below 20% except for calcium (~80% error). The RSF determined for vanadium and cobalt is not verified, as these values are not reported in ferrosilicon 195 certificate. Therefore, it was necessary to validate the results further using another complimentary technique that was not used for reporting the values in NIST certificates, for example, ICP-MS as used in this study. Although NIST recommends using 200–250 mg of powders to compare analytical results as reported in NIST certificates, approximately 30 mg of powders was used for ICP-MS analysis. The use of 30 mg of powders for ICP-MS analysis is close to 25–35 mg powder used for obtaining abundance corrected ion beam ratio by Astrum GDMS. As can be observed from Table S1,† for most of the elements the mass fraction values are comparable to NIST certified values, except for calcium. The variation in mass fraction value of calcium is about 3-folds as compared to ICP-MS values. This is likely the reason why error estimation for calcium was higher based on 57b certified value (Table 1). Indeed, a better correspondence is observed for calcium based on ICP-MS values (Table 2). The RSF estimates for all other elements are comparable to what was obtained in Table 1. The differences in matrix composition of 57b and ferrosilicon 195 powders can be expected to contribute to some discrepancies in RSF estimation. In other similar studies, Zhang *et al.* reported that the error estimate can vary as much as by 30% when matrix composition varies.<sup>18</sup> The discrepancy is about 20% in this study.

## D. Conclusions

This study describes the use of indium sheets for direct measurement of silicon powders using minimal sample preparation steps. Deployment of indium sheets for analysis of silicon powders resulted into stable signal for most of the elements presented in this study. The variation in argon flow was quantified along with other impurity elements to identify a range of discharge conditions where the deviation is minimum. Further, discharge setting leading to optimum crater in flat silicon sample was also considered before finalizing the optimum discharge parameters for RSF determination. The RSF was estimated and verified by subjecting CRMs 57b and 195 to the discharge condition of 2.3 mA and 1.2 kV using NIST certified values. The estimated RSFs were further verified by ICP-MS analysis, where comparable data was obtained with error below 20% for most elements. The observation of minimal deviation of mass fraction of various elements in a certain current and voltage range was predicted by plotting variation in

quantification of discharge gas flow. This is a novel finding and this approach can be useful for selecting optimum discharge parameters for other matrices also. Nevertheless, more investigations on various matrices and sample forms are needed to generalize the conclusion that plotting discharge gas can be useful for RSF determination.

## Conflicts of interest

There are no conflicts to declare.

## Acknowledgements

The authors are thankful to senior engineer Syverin Lierhagen at Department of Chemistry at the Norwegian University of Science and Technology (NTNU) for ICP-MS analysis and fruitful discussions. Dr Øyvind Sunde Sortland at Department of Materials Science and Engineering at NTNU is thanked for providing silicon flat sample.

## Notes and references

- 1 A. Bogaerts, in *Encyclopedia of Spectroscopy and Spectrometry*, ed. J. C. Lindon, Elsevier, Oxford, 1999, pp. 669–676, DOI: 10.1006/rwsp.2000.0107.
- 2 C. D. Quarles, J. Castro and R. K. Marcus, in *Encyclopedia of Spectroscopy and Spectrometry*, ed. J. C. Lindon, G. E. Tranter and D. W. Koppenaal, Academic Press, Oxford, 3rd edn, 2017, pp. 30–36, DOI: 10.1016/B978-0-12-803224-4.00056-X.
- 3 R. K. Marcus and J. A. C. Broekaert, *Glow Discharge Plasmas in Analytical Spectroscopy* John Wiley & Sons Ltd, 2003.
- 4 D. M. P. Milton and R. C. Hutton, *Spectrochim. Acta, Part B*, 1993, **48**, 39–52.
- 5 R. Qian, S. Zhuo, Z. Wang and P. K. Robinson, *J. Anal. At. Spectrom.*, 2013, **28**, 1061–1067.
- 6 D. C. Duckworth, C. M. Barshick and D. H. Smith, *J. Anal. At. Spectrom.*, 1993, **8**, 875–879.
- 7 M. van Straaten, K. Swenters, R. Gijbels, J. Verlinden and E. Adriaenssens, *J. Anal. At. Spectrom.*, 1994, **9**, 1389–1397.
- 8 S. L. Tong and W. W. Harrison, *Spectrochim. Acta, Part B*, 1993, **48**, 1237–1245.
- 9 J. C. Woo, N. Jakubowski and D. Stuewer, *J. Anal. At. Spectrom.*, 1993, **8**, 881–889.
- 10 L. Aldave de las Heras, E. Hrncecek, O. Bildstein and M. Betti, *J. Anal. At. Spectrom.*, 2002, **17**, 1011–1014.
- 11 M. Betti, *J. Anal. At. Spectrom.*, 1996, **11**, 855–860.
- 12 R. Matschat, J. Hinrichs and H. Kipphardt, *J. Anal. At. Spectrom.*, 2006, **386**, 125–141.
- 13 T. Gusarova, T. Hofmann, H. Kipphardt, C. Venzago, R. Matschat and U. Panne, *J. Anal. At. Spectrom.*, 2010, **25**, 314–321.
- 14 T. Gusarova, B. Methven, H. Kipphardt, R. Sturgeon, R. Matschat and U. Panne, *Spectrochim. Acta, Part B*, 2011, **66**, 847–854.
- 15 J. Zhang, T. Zhou, Y. Tang, Y. Cui and J. Li, *J. Anal. At. Spectrom.*, 2016, **31**, 2182–2191.
- 16 M. Inoue and T. Saka, *Anal. Chim. Acta*, 1999, **395**, 165–171.

- 17 W. Schelles, K. J. R. Maes, S. De Gendt and R. E. Van Grieken, *Anal. Chem.*, 1996, **68**, 1136–1142.
- 18 J. Zhang, T. Zhou, Y. Tang, Y. Cui and D. Song, *Anal. Bioanal. Chem.*, 2018, **410**, 7195–7201.
- 19 M. Di Sabatino, A. L. Dons, J. Hinrichs and L. Arnberg, *Spectrochim. Acta, Part B*, 2011, **66**, 144–148.
- 20 C. Venzago, L. Ohanessian-pierrard, M. Kasik, U. Collisi and S. Baude, *J. Anal. At. Spectrom.*, 1998, **13**, 189–193.
- 21 M. Kasik, C. Venzago and R. Dorka, *J. Anal. At. Spectrom.*, 2003, **18**, 603–611.
- 22 W. Vieth and J. C. Huneke, *Spectrochim. Acta, Part B*, 1991, **46**, 137–153.
- 23 G. Coletti, *Prog. Photovoltaics*, 2013, **21**, 1163–1170.
- 24 G. Stokkan, M. Di Sabatino, R. Søndén, M. Juel, A. Autfuffe, K. Adamczyk, H. V. Skarstad, K. E. Ekstrøm, M. S. Wiig, C. C. You, H. Haug and M. M'Hamdi, *Phys. Status Solidi A*, 2017, **214**, 1700319.
- 25 G. Paudel, M. Kasik and M. Di Sabatino, *J. Anal. At. Spectrom.*, 2019, **34**, 1829–1837.
- 26 P. W. J. M. Boumans, *Anal. Chem.*, 1972, **44**, 1219–1228.
- 27 G. Paudel, S. Khromov, M. Kasik, H. J. Roven and M. Di Sabatino, *J. Anal. At. Spectrom.*, 2020, **35**, 1450–1457.
- 28 A. Bogaerts and R. Gijbels, *J. Anal. At. Spectrom.*, 1996, **11**, 841–847.
- 29 C. Gonzalez-Gago, P. Šmíd, T. Hofmann, C. Venzago, V. Hoffmann, W. Gruner, J. Pfeifer, S. Richter and H. Kipphardt, *J. Anal. At. Spectrom.*, 2019, **34**, 1109–1125.

## Supplementary information

<b>Figure S1:</b> Signal stability of various elements/isotopes upon analysis of indium pressed 57b silicon powder at a discharge condition of 2 mA and 1 kV using argon flow rate of 0.50 ml/min.....	2
<b>Figure S2:</b> Relation between argon flow rate and current at various voltages upon analysing indium pressed 57b silicon powder.....	2
<b>Figure S3:</b> Variation in absolute intensities of various elements/isotopes, silicon (A), boron (B), phosphorous (C), cobalt (D), aluminium (E), iron (F), chromium (G), and copper (H) upon analysing indium pressed 57b silicon powder with discharge condition in range of 1 – 3.5 mA and 1 – 1.4 kV.....	3
<b>Figure S4:</b> Variation in quantification of oxygen (A) and argon (B) upon analysing upgrade metallurgical grade flat silicon sample at discharge condition in range of 0.5 – 5 mA and 1.2 – 1.6 kV, plotted using standard RSF.....	4
<b>Figure S5:</b> Crater profile of flat silicon sample after sputtering for 2.5 h at discharge condition of 2.3 mA, 0.7 kV using argon flow of 0.4 ml/min.....	4
<b>Table S1:</b> Summary of average and uncertainty associated with various elements based on NIST certificates and after ICP-MS analysis.....	4

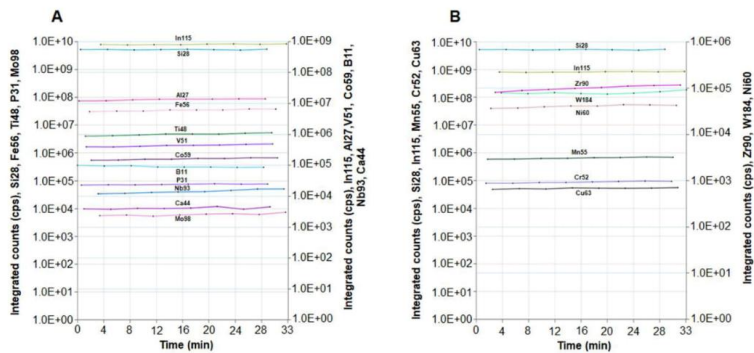


**Figure S1:** Signal stability of various elements/isotopes upon analysis of indium pressed 57b silicon powder at a discharge condition of 2 mA and 1 kV using argon flow rate of 0.50 ml/min.

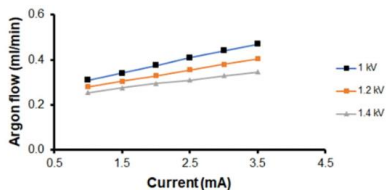


**Figure S2:** Relation between argon flow rate and current at various voltages upon analysing indium pressed 57b silicon powder.

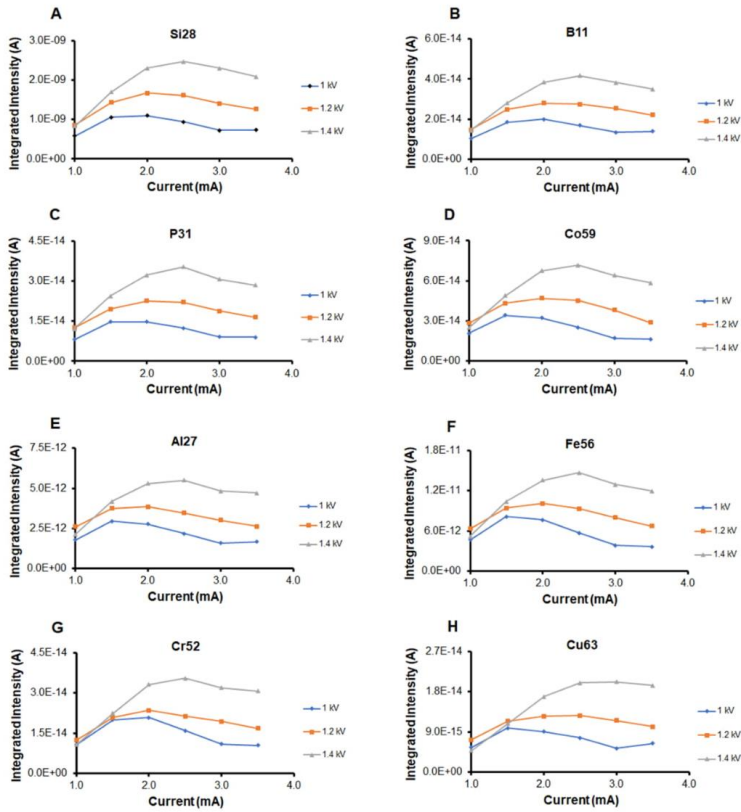


**Figure S3:** Variation in absolute intensities of various elements/isotopes, silicon (A), boron (B), phosphorous (C), cobalt (D), aluminium (E), iron (F), chromium (G), and copper (H) upon analysing indium pressed 57b silicon powder with discharge condition in range of 1 – 3.5 mA and 1 – 1.4 kV.

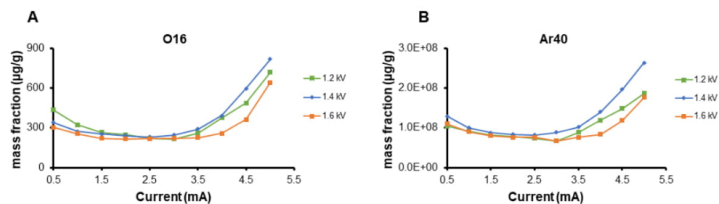


**Figure S4:** Variation in quantification of oxygen (A) and argon (B) upon analysing a flat silicon sample at discharge condition in range of 0.5 – 5 mA and 1.2 – 1.6 kV, plotted using standard RSF.

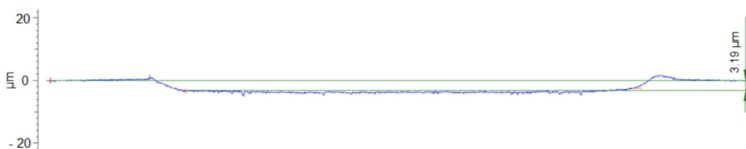


**Figure S5:** Crater profile of a flat silicon sample after sputtering for 2.5 h at discharge condition of 2.3 mA, 0.7 kV using argon flow of 0.4 ml/min.

**Table S1:** Summary of average and uncertainty associated with various elements based on NIST certificates and after ICP-MS analysis.

	Values from Certificates (µg/g)		ICP-MS reference values (µg/g)	
	NIST 57b silicon powder	NIST 195 ferrosilicon powder	NIST 57b silicon powder	NIST 195 ferrosilicon powder
Boron	12.5 ± 17%*	10.5 ± 15%	13.1 ± 11%	9.4 ± 4%
Aluminium	1690 ± 13%	460.0 ± 20%*	1548.9 ± 6%	434.3 ± 3%
Phosphorous	16.3 ± 9%	190.0 ± 46%*	14.3 ± 5%	139.0 ± 2%
Calcium	22.2 ± 20%*	540.0 ± 35%*	7.7 ± 19%	387.7 ± 8%
Titanium	346 ± 14%	367.0 ± 10%*	302.8 ± 4%	322.2 ± 4%
Vanadium	25**	-	23.7 ± 4%	19.6 ± 3%
Chromium	17.3 ± 19%*	474.0 ± 8%	15.9 ± 4%	378.9 ± 2%
Manganese	78.2 ± 9%	1710.0 ± 3%	70 ± 4%	1398.8 ± 4%
Iron	3400 ± 2%	236200.0 ± 1%	3160.3 ± 6%	204555.2 ± 2%
Cobalt	14**	-	11.9 ± 5%	24.7 ± 1%
Nickel	15.3 ± 11%	318.0 ± 6%	16.3 ± 3%	266.3 ± 2%
Copper	17.2 ± 34%*	468.0 ± 5%	21.5 ± 4%	387.9 ± 2%
Zirconium	17.8 ± 3%	110.0 ± 60%*	19.2 ± 8%	110.6 ± 7%
Niobium	-	-	1.3 ± 6%	2.8 ± 4%
Molybdenum	-	-	2.8 ± 13%	72.3 ± 1%
Tungsten	-	-	39.3 ± 8%	13.9 ± 4%

\*, \*\* and no asterisk sign represent reference, information, and certified values respectively as reported on NIST certificates of silicon 57b and ferrosilicon 195. Percentage values represent RSD calculated from average and uncertainty as shown in Table 1 and Table 2.

### **Paper III: Tantalum flat sputtering and roughness**

**Paudel, G.**, Khromov, S., Kasik, M., Roven, H. J., and Di Sabatino, M. (2020) Influence of polycrystalline material on crater shape optimization and roughness using low-power/low-pressure direct-current glow discharge mass spectrometry, *Journal of Analytical Atomic Spectrometry* 35, 1450-1457.

Reproduced by permission of The Royal Society of Chemistry



Cite this: *J. Anal. At. Spectrom.*, 2020, **35**, 1450

## Influence of polycrystalline material on crater shape optimization and roughness using low-power/low-pressure direct-current glow discharge mass spectrometry†

Gagan Paudel,<sup>a</sup> Sergey Khromov,<sup>a</sup> Martin Kasik,<sup>b</sup> Hans Jørgen Roven<sup>b</sup> and Marisa Di Sabatino<sup>a</sup>

Depth profiling is an attractive approach for analysis of non-homogeneous samples and layered materials. This application requires an optimum sputtered crater profile, which means a flat crater bottom with steep walls and a low roughness. It is known that discharge parameters are one of the most important factors influencing the crater shape. Hence, in the present work, different combinations of GDMS discharge current, voltage and argon flow, giving a flat crater bottom in tantalum are presented. A combination of mechanical profilometry, scanning electron microscopy and electron back scattered diffraction is used to show the contribution of grain orientation on various sputtering characteristics and crater bottom roughness. The results of the study indicate that differential sputtering is consistent at both higher and lower discharge conditions. The crater bottom roughness can be attributed to the differential sputtering of grains in polycrystalline materials.

Received 13th February 2020  
Accepted 9th June 2020

DOI: 10.1039/d0ja00055h

rsc.li/jaas

### Introduction

The glow discharge mass spectrometry (GDMS) utilizes glow discharge plasma to sputter atoms from the sample surface. Hence, atoms translate to ions that constitute the plasma. The ions thus formed are separated based on differences in their mass to charge ratio, allowing multi-elemental characterization. In general, GDMS offers two major applications namely bulk analysis and depth profiling.<sup>1–3</sup> For bulk analysis, as impurities are considered to be sufficiently homogenous throughout the sample, specific concentration of each element/isotope is usually obtained after a pre-sputtering when a steady glow discharge is reached. The bulk analysis is applied in quality assessment of metals, alloys, polymers, semiconductors, insulators *etc.*<sup>3,4</sup> The flat shaped samples allow characterization of concentration changes of analytes as a function of depth, *i.e.* depth profiling. Depth profiling has been used to determine coating performance, quality control related to elemental diffusion *etc.* The method can be used to profile coatings,<sup>5</sup> films,<sup>6</sup> bi- and multilayered materials.<sup>7,8</sup> It should be mentioned that secondary ion mass spectrometry (SIMS) can be used for depth profile analysis with better depth and lateral resolution.<sup>9</sup>

Nevertheless, SIMS is often compromised by limited availability of matrix-matched standards. Besides SIMS, other techniques such as X-ray photoelectron spectroscopy (XPS) and Auger electron spectroscopy (AES) can discriminate the crater edge effects by analyzing inner part of sputtered crater. In these analytical techniques, sputtering is more time consuming. Also mixing effects are stronger leading to matrix related effect. GDMS is less matrix dependent due to separation of sputtering and ionization events in space and time. Hence, GDMS is less affected by limited availability of matrix-matched standards. Another well-established analytical technique used for depth profiling is glow discharge optical emission spectroscopy (GDOES).<sup>2,10</sup> In 2017, Lobo *et al.* reviewed depth profiling applications of both GDMS and GDOES.<sup>11</sup> Comparatively, GDOES is more popular than GDMS for depth profiling and quality control applications in various industries. However, GDOES is limited to detection of impurities in percentage to parts per million (ppm) level. GDMS, however, offers dynamic range detection comprising up to 12 orders of magnitude, *i.e.* from percentage to parts per billion (ppb).<sup>12,13</sup> Thus, due to analytical merits of GDMS there is a need to improve its depth profiling capabilities.

Depth profiling relies on the assumption that atoms in the sample surface are eroded layer by layer, thus allowing conversion of time related- to depth related information. Therefore, for depth profiling a flat crater is a pre-requisite to ensure that atoms are sputtered from the same depth (layer) at a given time and hence ionized and recorded simultaneously.

<sup>a</sup>Department of Materials Science and Engineering, Norwegian University of Science and Technology, 7491 Trondheim, Norway. E-mail: gagan.paudel@ntnu.no

<sup>b</sup>MK2 Technologies Inc., Jamesville NY 13078, USA

† Electronic supplementary information (ESI) available. See DOI: 10.1039/d0ja00055h



However, non-uniform sputtering is commonly encountered. It has been demonstrated by Bogaerts and Gijbels that the electric potential distribution in front of the sample is slightly curved at the proximity of the anode front plate aperture as compared to the center of the sample.<sup>14</sup> This leads to enhanced influx of energetic argon ions towards the edge of the front plate anode aperture, leading to more sputtering at edges as compared to the sample center. This phenomenon is referred to as an edge effect (also named trenching). Bogaerts *et al.* developed the work further and suggested that the electric potential distribution in front of the cathode can be modified by changing current and voltage to mitigate the edge effect.<sup>15</sup> In general, keeping the current constant while voltage is increased, the crater profile changes from concave (U-shaped crater) to convex (W-shaped crater).<sup>15</sup> Thus, combinations of current and voltage that lead to flat craters can be determined empirically. Optimal combinations of these two parameters depend on the instrument, specimen matrix, type of discharge gas and flow rates (pressure). Work along these lines has been performed for low-power/low-pressure GDMS with mega cell design (VG 9000, Thermo Scientific)<sup>14</sup> and with fast-flow/high-pressure GDMS with Grimm-type GD cell geometry (Element GD, Thermo).<sup>16</sup> Another instrument that relies in continuous direct current, Astrum (Nu Instruments, UK) is also a low-power/low-pressure GDMS like VG 9000. However, a systematic work demonstrating a crater shape optimization is missing for analysis with Astrum GDMS. Hence, this instrument is used in the presented study.

Moreover, Demény *et al.* demonstrated that the electrical field distribution of a glow discharge lamp can be modified by changing the anode tube geometry.<sup>17</sup> Such modifications in geometry resulted into change in crater shapes of steel sample due changes in sputtering rates. For Astrum, the entire GD cell body acts as anode which is not modified in the present study.

Furthermore, non-homogenous temperature distribution is often encountered in a crater.<sup>18</sup> High sample surface temperature may lead to matrix evaporation for some materials with a high vapor pressure such as zinc.<sup>19</sup> Therefore, GDMS users/operators during sputtering process look for approaches so that likelihood of sample heating can be reduced. One of such possibilities is to use pulsed glow discharge (PGD) source instead of continuous GD source so that the sample thermal stress is reduced. Likewise, another approach is to use instruments that offer cryocooling, such as Astrum and VG 9000. In that case, the sample heating during sputtering can be compensated.

Further, Ferreira and Büger demonstrated copper redeposition during a sputtering process using a glow discharge lamp through copper ion micrographs, which were generated from an ion microprobe mass analyser.<sup>20</sup> It should be noted that these authors also sputtered redeposited material. After a short period of time, an equilibrium between simultaneously occurring events of sputtering and redeposition was occurring. The rate and amount of deposition and re-sputtering also change with the discharge current and voltage used, which ultimately contributes to the final crater shape.

Another important aspect of crater shape is steepness of the crater wall. The ideal crater walls would be perpendicular to the sample surface. However, sloped walls are commonly observed as incoming and outgoing species are deflected at and around the edge of the anode front plate aperture. Raith *et al.* demonstrated that use of high purity tantalum metal masks with an aperture smaller than the anode aperture could improve the crater wall steepness.<sup>21</sup> Also, the work of Bogaerts and Gijbels had a similar recommendation.<sup>14</sup> However, an instrument operator should be aware that use of masks may lead to higher blank values. This could prohibit use of masks, for example when analyzing materials such as high purity silicon. Therefore, deployment of masks is not considered in the presented study.

The present authors are not aware of any journal publication demonstrating work on crater shape optimization using Astrum GDMS. However, during the European glow discharge symposium 2018, Disch presented some examples of optimum crater profiles for a copper matrix using Astrum GDMS.<sup>22</sup> Later, it was proposed that voltage (in kV) to current (in mA) ratio in range of 0.3–0.4 ( $\text{kV mA}^{-1}$ ) leads to flat craters. In the present work, discharge parameters that lead to flat craters in tantalum are investigated. Hence, the current to voltage ratio giving an optimum crater for tantalum is proposed. Moreover, it is commonly observed among GDMS users that sputtering often leads to more surface roughness at the bottom of the crater. In the current work, we investigate and discuss the factors that can cause this effect with focus on the material's grain orientation. Specifically, the effect of grain orientation on differential sputtering is clearly demonstrated.

## Experimental

### Sample preparation and method

Two sets of tantalums were used in the present study – one with large irregular grains larger than 1 mm in size and another with regular grains less than 1 mm. For simplicity, the former group is referred to as a “test sample” while the latter is denoted a “control sample”. All tantalum samples were grinded by grit 800 SiC paper, rinsed with water and ethanol. The samples were dried using hot gun air before being inserted into the instrument (Astrum, Nu Instruments, UK). This instrument has a low-pressure ion source, double focusing mass analysers and a dual detector system. For the present work, a flat cell GD design using a flat sample holder with 10 mm tantalum front plate orifice was used that resulted into the crater diameter of 10 mm. The specimens were cryogenically cooled for about 15 minutes before sputtering. A constant current mode was deployed to control and stabilize glow discharge conditions. High purity (6 N) argon was used as a discharge gas. After sputtering the crater profile was measured mechanically by a profilometer (MarSurf M 400, Mahr GmbH, Göttingen, Germany). The obtained crater was then studied by field emission scanning electron microscopy (SEM, Zeiss Ultra 55, Jena, Germany) and electron back scatter diffraction (EBSD, NORDIF UF-1100 detector, Trondheim, Norway). For SEM, the primary electron beam was accelerated with voltage of 20 kV and an objective aperture lens

of 30  $\mu\text{m}$  was selected. The obtained secondary electrons from the specimen were detected using a secondary electron detector. For EBSD, the sample was tilted at  $70^\circ$  before being probed by the primary electron beam accelerated with energy of 20 kV. The 300  $\mu\text{m}$  objective aperture lens was selected. The working distance (WD) was  $\sim 25$  mm. Appropriate adjustments were made to compensate for the tilt angle such that the sample was brought to focus before recording the Kikuchi patterns using an EBSD detector. All EBSD scans were taken with the same area size of  $225 \times 255$   $\mu\text{m}$  and 1.5  $\mu\text{m}$  step size. The raw EBSD patterns were recorded in NORDIF acquisition software and

indexed offline in TSL OIM Data collection (Ametek, USA) with body centred cubic (BCC) tantalum as a possible crystal structure. After that the EBSD maps were built in TSL OIM Analysis (Ametek, USA) software.

## Result and discussion

### Crater profile optimization

Since the most important aspects of crater profile evolution with various discharge parameters is already introduced, further details can be found in articles as referred.<sup>14,15,23</sup> It is worth

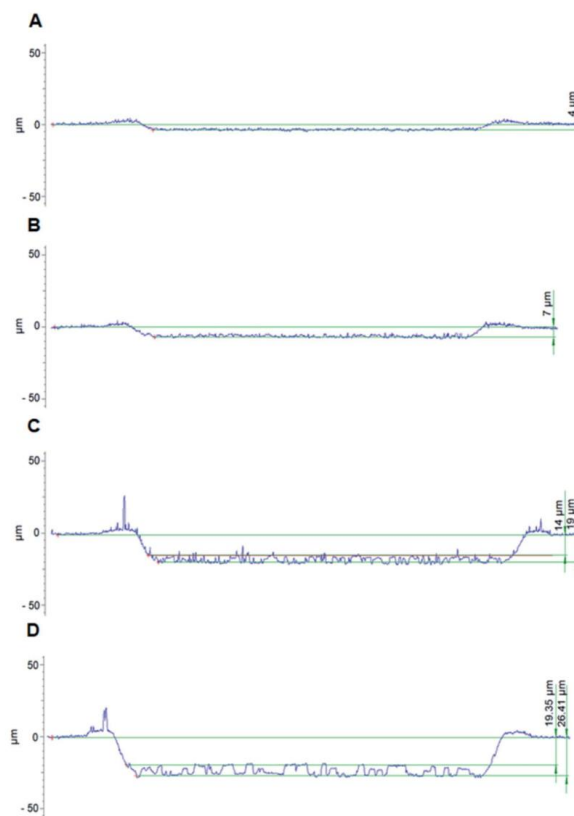


Fig. 1 Flat crater profile optimized for tantalum with small grains at various discharge conditions of 2 mA, 0.6 kV using  $0.27 \text{ ml min}^{-1}$  argon flow (A); 2.3 mA, 0.7 kV using  $0.25 \text{ ml min}^{-1}$  argon flow (B); 4 mA, 0.9 kV using  $0.30 \text{ ml min}^{-1}$  argon flow (C); and 5 mA, 1 kV using  $0.41 \text{ ml min}^{-1}$  argon flow (D), each after sputtering for 1.5 h.

mentioning that there are two typical operation modes for Astrum: (i) to fix current and adjust gas flow to obtain desired voltage, termed as constant current mode; (ii) to fix voltage and adjust gas flow to obtain desired current, termed as constant voltage mode. Nevertheless, according to the authors' experience, the former approach was found to be more appropriate.<sup>24</sup> Therefore, constant current mode was used to obtain flat crater profiles in this work. Some examples of flat crater profiles obtained for control samples are shown in Fig. 1. In order to get flat craters at higher currents also an increase of the gas flow is needed. The gas flow rates are expressed in standard cubic centimetre per minute (sccm) or equivalent unit, millilitre per minute ( $\text{ml min}^{-1}$ ). It is observed that for lower voltages (0.6–0.8 kV), a voltage to current ratio of  $\sim 0.3$  ( $\text{kV mA}^{-1}$ ) leads to flat craters, while for higher voltages (0.9–1 kV) the necessary ratio drops to  $\sim 0.2$  ( $\text{kV mA}^{-1}$ ). The voltage to current ratio in range of 0.2–0.35 ( $\text{kV mA}^{-1}$ ) is slightly below the flat crater conditions for copper where the ratio is 0.3–0.4 ( $\text{kV mA}^{-1}$ ).<sup>22</sup> The slight deviation might be related to a different matrix type introducing changes in the material properties for example, the secondary emission coefficient and thermal conductivity of the cathode material. Similar work on silicon resulted into flat crater at discharge condition of 2.3 mA, 0.7 kV. Crater profiles together with other results on silicon will be covered in another paper. It is possible that same conditions may not exactly fit for other matrices but can certainly serve as a starting point for crater shape optimization. In case flat craters are not obtained, it is recommended to fix one among current or voltage and change the other parameter as demonstrated in ref. 15.

The classical Boumans' equation describes a linear relationship of sputtering rate with voltage.<sup>25</sup> Indeed, a linear correspondence between sputtering rate and voltage is observed when current is kept constant at 3 mA (Fig. S1†). Additionally, if the Boumans' equation is applied to the present data, the threshold voltage ( $V_0$ ) is about  $\sim 0.23$  kV, which is reasonably close to the value reported for tantalum in Boumans' article ( $V_0 = 0.32$  kV). To be mentioned, it is still possible to obtain a flat crater below 0.6 kV. However, when the GD voltage is too low approaching the threshold potential, then the plasma becomes less stable. In addition, keeping an optimal ratio (0.2–0.35  $\text{kV mA}^{-1}$ ) for obtaining flat craters would require a very low current. As a consequence, the matrix signal intensity would be reduced, *i.e.* the measurement sensitivity will have to be compromised. Likewise, for higher voltages above 1 kV, current supply above 5 mA is needed. In our experience, there is higher fluctuation in current

and/or voltage at such high values of the parameters and therefore such conditions are not recommended.

It should be brought into attention that while performing weight loss experiments, weight of the sample before and after sputtering at a particular discharge condition is needed. This requires use of sensitive analytical balance that can accurately measure the difference in weight. For this work, analytical balance (PA224C, OHAUS Pioneer, Switzerland) was used that allows readability up to 0.1 mg. Therefore, to facilitate the variation in weight loss, use of higher current is advised. In this work, current of 3 mA was used to sputter tantalum sample with small grains for 30 minutes at various voltages in range of 0.6–1.9 kV (Fig. S1†).

#### Differential sputtering

After sputtering the test sample for 1.5 h at a discharge condition of 5 mA, 1 kV using argon flow of  $0.55 \text{ ml min}^{-1}$ , the grains inside the crater were visible with naked eyes. The corresponding crater profile is presented in Fig. 2. As observed, there is a clear 'step' in the crater profile, which indicates differential sputtering. To check if the observed step persists, the sample was re-inserted to the instrument and sputtered at the same spot for another 1 h (total 2.5 h) using same discharge condition (5 mA, 1 kV). This time using argon flow of  $0.43 \text{ ml min}^{-1}$ . The setting up of the sample into the sample holder and insertion of sample probe into GD chamber is a manual process. Despite of being mindful of this fact, an adjustment of argon flow from initial value of  $0.55 \text{ ml min}^{-1}$  to  $0.43 \text{ ml min}^{-1}$  was needed to obtain the same discharge condition (5 mA, 1 kV). This is probably linked to the change in crater bottom roughness as compared to freshly polished surface when sputtered initially. However, interestingly, the variation in gas flow rates did not alter the crater shape from initially obtained flat crater bottom (Fig. 2 and 3).

The accompanying scanning electron micrograph image of the crater after 2.5 h (1.5 h + 1 h sputtering) is presented in Fig. 3A. The vertical- and horizontal lines approximately indicate locations where two crater profiles were measured. The profile along the horizontal line was measured twice, once after 1.5 h of sputtering (Fig. 2) and the second time after additional 1 h sputtering (Fig. 3B). The profile measured along the vertical line (after 1.5 h + 1 h sputtering) is crossing three grains. Two well developed steps (Fig. 3C) are clearly visible along the bottom of the crater. Therefore, EBSD was performed inside the actual crater to check whether the steps corresponded to different grain orientations, *i.e.* grain boundaries. The results

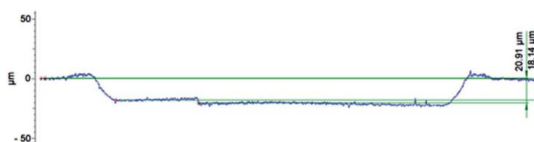


Fig. 2 Crater profile of tantalum with large grains after 1.5 h of sputtering at discharge condition of 5 mA, 1 kV using  $0.55 \text{ ml min}^{-1}$  argon flow.

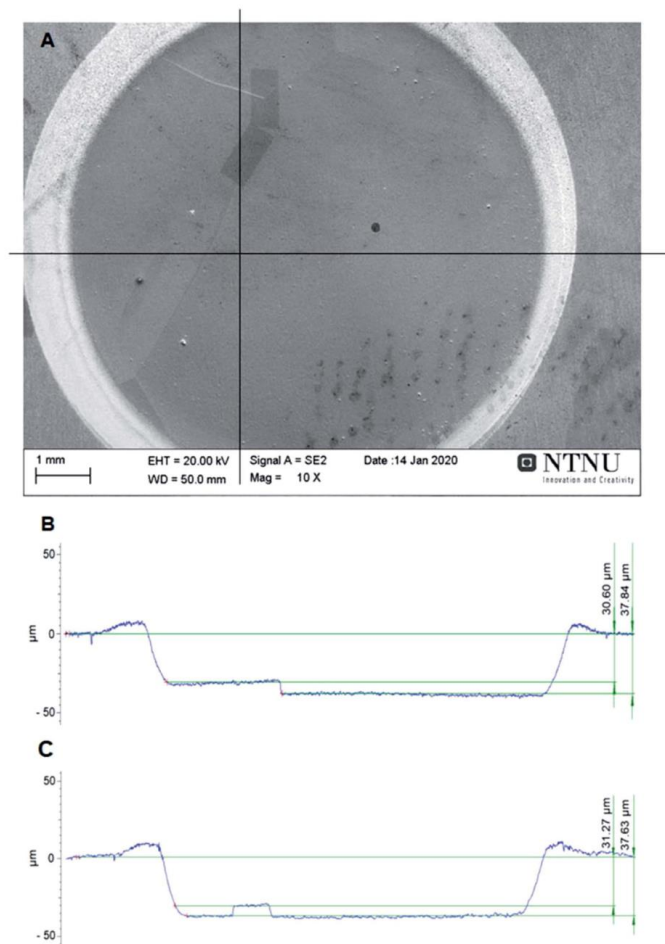


Fig. 3 Scanning electron micrograph of tantalum with large grains after additional 1 h of sputtering (total 2.5 h sputtering) at discharge condition of 5 mA, 1 kV using  $0.43 \text{ ml min}^{-1}$  argon flow (A), the corresponding crater profile map upon horizontal (B) and vertical (C) measurement along the line using a mechanical profilometer.

obtained are presented in Fig. 4 as secondary electron micrograph (Fig. 4A) and corresponding inverse pole figure (Fig. 4B). Indeed, the inverse pole figure indicates that three different grain orientation exists. The correlation between the EBSD map

and profilometer map showed that the grain close to plane orientation (111) sputters less as compared to a grain that is in between planes (001) and (101) (Fig. 3B and 4). Also, the grain close to plane (101) sputters almost equally to the grain being in



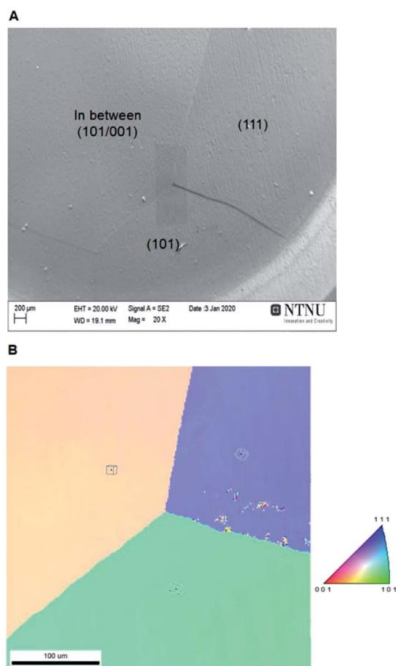


Fig. 4 Scanning electron micrograph of tantalum with large grains showing shaded region where electron backscattered diffraction was performed (A), and corresponding inverse pole figure (B) after 2.5 h sputtering at discharge condition of 5 mA, 1 kV. Corresponding inverse pole figure legend to the right.

between planes (001) and (101) (Fig. 3C and 4). This observation is consistent and can be verified further through Fig. S2,† where the blue grain with (111) plane is at a different height compared to the other two planes. It should be mentioned, however, that other studies exist, stating presence of differential sputtering as a function of crystallographic orientation when the energy of probing ions are above 1 keV.<sup>26–28</sup> Interestingly, differential sputtering can also be observed in GDMS where ion energies are at or lower than 1 keV.<sup>29</sup>

Also, it was checked whether differential sputtering is occurring with large grains when lower voltage and current were used. Here, the observation of the step is consistent at 3 mA, 0.8 kV (at 0.28 ml min<sup>-1</sup> argon flow) and 2.3 mA, 0.7 kV (at 0.37 ml min<sup>-1</sup> argon flow) each after 2 h of sputtering (Fig. 5). The grain texture difference could potentially be the reason for variation in argon flow rates in order to obtain flat crater using

the same discharge condition (2.3 mA, 0.7 kV) for the control sample (Fig. 1B) and the test sample (Fig. 5B). In Fig. 5, the depth axis scale is changed (zoomed) from what is used in Fig. 2 and 3 to show the presence of steps. It has to be pointed out that accurate quantitative value to estimate the differential sputtering or roughness is not presented in this paper. The grain texture varies from one sample to another. Also, for polycrystalline material it is likely that the roughness at the crater bottom is always changing. Thus, it is challenging to provide accurate quantitative data about differential sputtering and roughness for polycrystalline material. Also, ideally the EBSD map of entire crater is required to precisely identify the grain orientations to comment on its contribution to differential sputtering and roughness. Such limitations or inadequacies of data representation does not deviate from the conclusion that differential sputtering is present for the samples used in this study. Lines at the top and bottom of crater profile are used to indicate differential sputtering and roughness, where appropriate, to guide the reader.

There are probably several possible explanations to the observed differences in sputtering rates with different grain orientation. One plausible explanation can be linked to the variation in planar densities of the grains. Since plane (111) has lower density than (101), there could be slightly less energy and momentum transfer from the argon ions as they probe this plane. Conversely, higher momentum and energy transfer can be expected for denser planes. Zhang *et al.* performed similar work on tantalum with magnetron sputtering where (110) grains had higher sputtering rate as compared to (111) planes.<sup>30</sup> In another study performed by Chen *et al.* using GDOES on iron, sputtered depth for crystallites with different orientation were reported to be unequal.<sup>23</sup> Iron has also a BCC crystal structure and the authors reported less sputtering of (111) than (001) planes.<sup>23</sup> In the present work the plane orientation showing the highest sputtering rate is in between (001) and (101), and would have a planar density relatively close to (101). Hence, this is probably the reason why these planes sputter equivalently (Fig. 3C and S2†).

#### Roughness at crater bottom for materials with small grains

The entire study is designed using tantalum samples with different microstructure *i.e.* larger and smaller than 1 mm grain size so that only a few or many grains could be obtained within the crater. This allowed observation of results where effect of grains could be clearly demonstrated. There could be other reasons for crater bottom roughness. To mention a few—uneven sample polishing, presence of inclusions and other sub-grain structures. In fact, the sputtering process itself can lead to indentations as a result of argon ions hitting on sample surface which contributes to some roughness. This is dependent on energy of the ion projectile hitting the sample surface which is also true for single crystals (monocrystalline) materials.<sup>31</sup> However, for samples used in present study, the effect of grains are likely to dominate. For tantalum with finer grains, where grain orientations differ substantially (Fig. 6), a differential sputtering led to enhanced crater bottom roughness (Fig. 1D

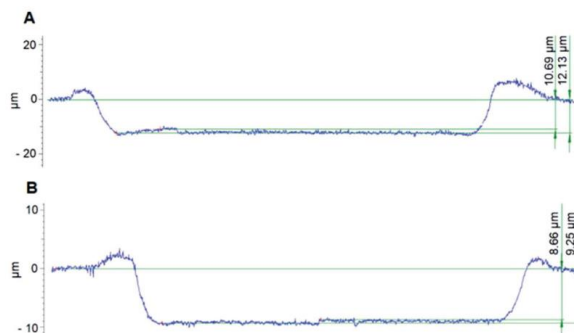


Fig. 5 Crater profiles for tantalum with large grains at various discharge conditions of 3 mA, 0.8 kV using  $0.28 \text{ ml min}^{-1}$  argon flow (A), and 2.3 mA, 0.7 kV using  $0.37 \text{ ml min}^{-1}$  (B), each after 2 h of sputtering.

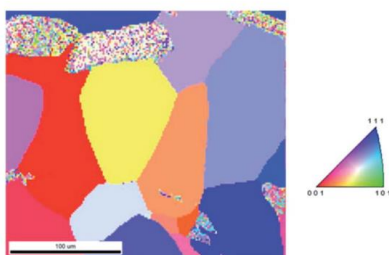


Fig. 6 EBSD map for tantalum with small grains at discharge conditions of 5 mA, 1 kV using  $0.41 \text{ ml min}^{-1}$  argon flow after sputtering for 1.5 h. Corresponding inverse pole figure legend to the right.

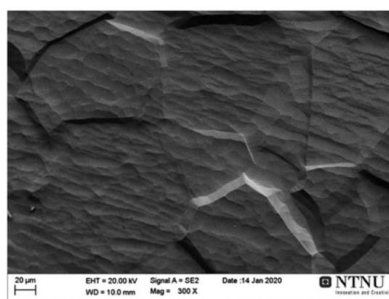


Fig. 7 Scanning electron micrographs of tantalum with small grains at discharge conditions of 5 mA, 1 kV using  $0.41 \text{ ml min}^{-1}$  argon flow after sputtering for 1.5 h.

and 7) as compared to tantalum with large grains (Fig. 2–4 and S2†), when both types of tantalum were sputtered at same discharge condition (5 mA, 1 kV). To compare if this observation is consistent with lower discharge condition, Fig. 1B is replotted in Fig. S3† with axis scale matching the axis scale in Fig. 5B. The enhanced roughness is evident for the control sample (finer grains) as compared to the test sample (larger grains) when operated at same discharge condition of 2.3 mA, 0.7 kV (Fig. 5B and S3†).

For polycrystalline material, therefore roughness can be fully or partially linked to differential sputtering of grains with different crystallographic orientations. It could likely be the reason why GDMS users almost always observe some roughness at the crater bottom. It is worth mentioning that according to some authors, atoms may have different sputter yields.<sup>32</sup> This phenomenon could eventually contribute to roughness if the concentration of impurities is high and the actual elemental sputter yields would be substantially different. However, for

pure tantalum samples, major impurities are molybdenum, tungsten and niobium. All those elements do have similar sputtering yields. Hence, it is unlikely these impurities would contribute significantly to roughness of sputtered tantalum. Thus, at least for tantalum, the contribution of such an effect can be regarded negligible.

## Conclusions

This study describes the impact of discharge parameters on crater profile optimization of tantalum. The voltage to current ratio in the range of  $0.2\text{--}0.35 \text{ (kV mA}^{-1}\text{)}$  resulted into flat craters. Thus, flat craters were obtained for five different discharge settings: (i) 2 mA, 0.6 kV; (ii) 2.3 mA, 0.7 kV; (iii) 3 mA, 0.8 kV; (iv) 4 mA, 0.9 kV and (v) 5 mA, 1 kV. The results of this work indicate that it is likely that the differential sputtering of

grains has a dominating contribution to the crater bottom roughness in the studied samples. However, more investigations of various materials with larger and smaller grains are needed to generalize this conclusion.

## Conflicts of interest

The authors have no conflicts to declare.

## Acknowledgements

The authors are thankful to Nu Instruments scientist, Dr Benoit Disch for providing tantalum sample and for fruitful discussions regarding crater shape optimization.

## Notes and references

- 1 A. Bogaerts, E. Neyts, R. Gijbels and J. van der Mullen, *Spectrochim. Acta, Part B*, 2002, **57**, 609–658.
- 2 R. K. Marcus and J. A. C. Broekaert, *Glow Discharge Plasmas in Analytical Spectroscopy*, John Wiley & Sons Ltd, 2003.
- 3 C. Venzago and J. Pisonero, in *Sector Field Mass Spectrometry for Elemental and Isotopic Analysis*, The Royal Society of Chemistry, 2015, pp. 319–380, DOI: 10.1039/9781849735407-00319.
- 4 A. A. Ganeev, A. R. Gubal, K. N. Uskov and S. V. Potapov, *Russ. Chem. Bull.*, 2012, **61**, 752–767.
- 5 J. Pisonero, J. Fandino, J. H. Nordlien, S. Richter, J. Pfeifer, C. D. Quarles, J. Gonzalez, N. Jakubowski and N. Bordel, *J. Anal. At. Spectrom.*, 2019, **34**, 2252–2260.
- 6 J. Pisonero, B. Fernández, R. Pereiro, N. Bordel and A. Sanz-Medel, *TRAC, Trends Anal. Chem.*, 2006, **25**, 11–18.
- 7 P. Konarski, K. Kaczorek, M. Cwil and J. Marks, *Vacuum*, 2008, **82**, 1133–1136.
- 8 J. Pisonero, R. Valledor, A. Licciardello, C. Quirós, J. I. Martín, A. Sanz-Medel and N. Bordel, *Anal. Bioanal. Chem.*, 2012, **403**, 2437–2448.
- 9 J. Pisonero, B. Fernández and D. Günther, *J. Anal. At. Spectrom.*, 2009, **24**, 1145–1160.
- 10 R. Payling, D. Jones and A. Bengtson, *Glow Discharge Optical Emission Spectrometry*, Wiley, 1997.
- 11 L. Lobo, B. Fernández and R. Pereiro, *J. Anal. At. Spectrom.*, 2017, **32**, 920–930.
- 12 M. Di Sabatino, C. Modanese and L. Arnberg, *J. Anal. At. Spectrom.*, 2014, **29**, 2072–2077.
- 13 C. Modanese, G. Gaspar, L. Arnberg and M. Di Sabatino, *Anal. Bioanal. Chem.*, 2014, **406**, 7455–7462.
- 14 A. Bogaerts and R. Gijbels, *Spectrochim. Acta, Part B*, 1997, **52**, 765–777.
- 15 A. Bogaerts, W. Verscharen and E. Steers, *Spectrochim. Acta, Part B*, 2004, **59**, 1403–1411.
- 16 J. Pisonero, I. Feldmann, N. Bordel, A. Sanz-Medel and N. Jakubowski, *Anal. Bioanal. Chem.*, 2005, **382**, 1965–1974.
- 17 D. Demény, L. Szűcs and M. Adamik, *J. Anal. At. Spectrom.*, 1992, **7**, 707–710.
- 18 L. Wilken, V. Hoffmann and K. Wetzig, *J. Anal. At. Spectrom.*, 2003, **18**, 1133–1140.
- 19 G. J. M. Hagelaar and L. C. Pitchford, *J. Anal. At. Spectrom.*, 2002, **17**, 1408–1410.
- 20 N. P. Ferreira and P. A. Büger, *Redeposition of Sputtered Material in a Glow-Discharge Lamp Measured by Means of an Ion Microprobe Mass Analyser*, report 18657109, National Physical Research Laboratory, Pretoria, South Africa, 1978.
- 21 A. Raith, R. C. Hutton and J. C. Huneke, *J. Anal. At. Spectrom.*, 1993, **8**, 867–873.
- 22 B. Disch, presented in part at the *International Glow Discharge Spectroscopy Symposium*, IGSS2018, Berlin, Germany, 2018.
- 23 L. Chen, M. C. Simmonds, S. Habesch and J. M. Rodenburg, *Surf. Interface Anal.*, 2001, **31**, 206–211.
- 24 G. Paudel, M. Kasik and M. Di Sabatino, *J. Anal. At. Spectrom.*, 2019, **34**, 1829–1837.
- 25 P. W. J. M. Boumans, *Anal. Chem.*, 1972, **44**, 1219–1228.
- 26 G. D. Magnuson and C. E. Carlston, *J. Appl. Phys.*, 1963, **34**, 3267–3273.
- 27 A. L. Southern, W. R. Willis and M. T. Robinson, *J. Appl. Phys.*, 1963, **34**, 153–163.
- 28 R. Behrisch and W. Eckstein, *Sputtering by Particle Bombardment*, Springer, 2007.
- 29 A. Bogaerts, PhD thesis, University of Antwerp, 1996.
- 30 Z. Zhang, L. Kho and C. E. W. Jr, *J. Vac. Sci. Technol., A*, 2006, **24**, 1107–1111.
- 31 D. Moreno and D. Eliezer, *J. Mater. Sci. Lett.*, 1994, **13**, 1591–1593.
- 32 R. K. Marcus, *Glow Discharge Spectroscopies*, Springer Science, 1991.

## Supplementary Information

**Figure S1:** Relationship between sputtering rate in terms of weight loss and voltage for tantalum with small grains.....1

**Figure S2:** EBSD map overlaid over secondary electron micrograph for tantalum sample with large grains showing grain boundaries and differential sputtering after 2.5 h sputtering at discharge condition of 5 mA, 1 kV. Corresponding inverse pole figure legend to the right.....1

**Figure S3:** Flat crater profile for tantalum with small grains at discharge condition of 2.3 mA, 0.7 kV using 0.25 ml/min argon flow after sputtering for 1.5 h, zoomed with a different axis scale using Figure 1B.....2

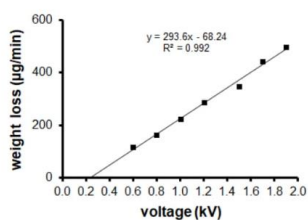


**Figure S1:** Relationship between sputtering rate in terms of weight loss and voltage for tantalum with small grains.

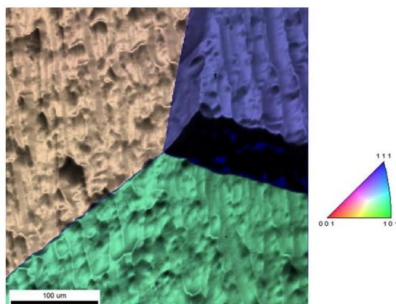


**Figure S2:** EBSD map overlaid over secondary electron micrograph for tantalum sample with large grains showing grain boundaries and differential sputtering after 2.5 h sputtering at discharge condition of 5 mA, 1 kV. Corresponding inverse pole figure legend to the right.





**Figure S3:** Flat crater profile for tantalum with small grains at discharge condition of 2.3 mA, 0.7 kV using 0.25 ml/min argon flow after sputtering for 1.5 h, zoomed with a different axis scale using Figure 1B.

#### **Paper IV: Steel-Aluminum joint depth profiling**

**Paudel, G.**, Langelandsvik, G., Khromov, S., Arbo S.M., Westermann, I., Roven, H.J., and Di Sabatino, M. Depth profiling at a steel-aluminum interface using slow-flow direct current glow discharge mass spectrometry, *in a peer review process of Journal of Analytical and Bioanalytical Chemistry*

This paper is awaiting publication and is not included in NTNU Open

**CHAPTER 9**  
**Appendix**

## Appendix 1: Ionization energy of various elements

The first ionization energy of various elements along with the isotope used for GDMS analysis in the PhD work. 'None' indicates there are no energy levels within about 2 eV of argon ion. 'Many' indicates there are several levels lying within about 0.02 eV above and about 1 eV below argon ion ground state and metastable levels (15.76 and 15.937 eV respectively), i.e., within range of about 14.7–16.0 eV for analyte elements. For number in parenthesis, the level gives charge transfer with argon ion metastable state (ref. 28).

Elements	Isotope used	Symbol	Ionization energy (eV)	Number of levels suitable for ACT
Boron	B11	B	8.30	None
Carbon	C12	C	11.26	None
Nitrogen	N14	N	14.53	-
Oxygen	O16	O	13.62	-
Sodium	Na23	Na	5.14	None
Aluminum	Al27	Al	5.99	None
Silicon	Si28	Si	8.15	1 (far)
Phosphorous	P31	P	10.49	None
Argon	Ar40	Ar	15.76	-
Calcium	Ca44	Ca	6.11	Many
Titanium	Ti48	Ti	6.83	Many
Vanadium	V51	V	6.75	Many
Chromium	Cr52	Cr	6.77	Many
Manganese	Mn55	Mn	7.43	Many
Iron	Fe56	Fe	7.90	Many
Cobalt	Co59	Co	7.88	Many
Nickel	Ni60	Ni	7.64	Many
Copper	Cu63	Cu	7.73	1
Zirconium	Zr90	Zr	6.63	Many
Niobium	Nb93	Nb	6.76	
Molybdenum	Mo98	Mo	7.09	Many
Tantalum	Ta181	Ta	7.89	
Tungsten	W184	W	7.98	Many

**Appendix 2:** Sputtering rate of tantalum, small grained<sup>a</sup> and large grained<sup>b</sup> at different glow discharge conditions. The depth represents the bottom layer as sputtering is associated with some roughness.

<b>Discharge condition</b>	<b>Time (min)</b>	<b>Depth, bottom layer (nm)</b>	<b>Sputtering rate (nm/min)</b>
2 mA, 0.6 kV	90 <sup>a</sup>	4000	44.4
2.3 mA, 0.7 kV	90 <sup>a</sup>	7000	77.8
3 mA, 0.8 kV	120 <sup>b</sup>	12130	101.1
4 mA, 0.9 kV	90 <sup>a</sup>	19000	211.1
5 mA, 1 kV	90 <sup>a</sup>	26410	293.4

ISBN 978-82-326-6760-4 (printed ver.)  
ISBN 978-82-326-6524-2 (electronic ver.)  
ISSN 1503-8181 (printed ver.)  
ISSN 2703-8084 (online ver.)



**NTNU**

Norwegian University of  
Science and Technology